



DIPLOMARBEIT

Electronic Structure of Thin-Film Bismuth for Spintronics: A Tight-Binding Study

ausgeführt am Institut für Festkörperelektronik der Technischen Universität Wien

unter der Anleitung von Univ.Prof. Dr.sc. Alexander Grüneis

durch

Marko Petric

Gußhausstraße 25-25a, 1040 Wien

February 2	4.	2025	

I declare that I have authored this thesis independently, that I have not used other
than the declared sources/resources, and that I have explicitly marked all materia
which has been quoted either literally or by content from the used sources.

Date

Signature

STATUTORY DECLARATION

TU Bibliothek, Die approbierte gedruckte Originalversion dieser Diplomarbeit ist an der TU Wien Bibliothek verfügbar wien vour knowledge hub The approved original version of this thesis is available in print at TU Wien Bibliothek.

DANKSAGUNG

Ich möchte mich von Herzen bei meiner Lebenspartnerin Iris bedanken, die mit mir gemeinsam die Achterbahn der Gefühle dieses Weges durchgestanden hat. Sie hat mir in schwierigen Momenten die Angst genommen, mich immer wieder gestärkt und manchmal auch das Denken im Leben außerhalb der Universität übernommen, besonders wenn ich zu sehr in meine Forschung vertieft war. Danke, dass du an meiner Seite bist!

Ein großer Dank geht an meine Schwester, die es auf ihre ganz eigene Art geschafft hat, mich in genau den richtigen Momenten voranzutreiben. Danke, dass du mir in den entscheidenden Momenten in den Hintern getreten hast, du Wappla.

Mein besonderer Dank gilt auch meinen Eltern, die mir diesen Lebensweg überhaupt erst ermöglicht haben. Mit ihrem Enthusiasmus und ihrer unerschütterlichen Unterstützung standen sie hinter jeder meiner Entscheidungen. Danke für alles, Mama und Papa!

Ein weiterer Dank geht an die gesamte Forschungsgruppe der Optoelektronischen Materialien des Institus für Festkörperelektronik. Dieses Jahr war eine der intensivsten Erfahrungen meiner wissenschaftlichen Entwicklung und das habe ich auch euch zu verdanken.

Zu guter Letzt möchte ich all den Menschen danken, die mich auf diesem Weg begleitet haben, die hier aber keinen Namen gefunden haben. Euch allen gebührt mein tiefster Dank - es bedeutet mir unglaublich viel, euch in meinem Leben zu wissen!

TW **Sibliothek**, Die approbierte gedruckte Originalversion dieser Diplomarbeit ist an der TU Wien Bibliothek verfügbar werknowiedgehub vourknowiedgehub

Contents

1	Intro	oductio	on	3
2	The	ory		5
	2.1	The C	rystal Structure of Bismuth	5
	2.2	The B	rillouin Zone of the rhombohedral Structure	8
		2.2.1	Thin Film Brillouin Zone of Bismuth(111)	10
	2.3	Tight-	Binding Formalism	11
		2.3.1	Slater-Koster Two-Center Approximation	15
	2.4	Symm	etries and Spin-Orbit Coupling	17
		2.4.1	Kramer's Theorem and Time-Reversal Symmetry	17
		2.4.2	Spin-Orbit Coupling and Inversion Symmetry	19
		2.4.3	Zeeman Effect	20
	2.5	Basis	Change	24
		2.5.1	Clebsch-Gordan Coefficents	25
		2.5.2	From Complex to Real Atomic Wave Functions	29
	2.6	Model	ing and Tight-Binding Calculations	32
		2.6.1	Infinite Bismuth Crystal (Bulk)	32
		2.6.2	Thin Bismuth Film	35
		2.6.3	The Bychkov-Rashba Effect and its Tight-Binding Formulation	37
	2.7	Topolo	ogical Matter	41
		2.7.1	Berry Phase, Connection and Curvature	44
		2.7.2	Chern Number	46
		2.7.3	Berry Curvature of a massive Dirac Fermion	47
		2.7.4	Topological Phase Transition in Terms of a half Chern Number	52
		2.7.5	Bulk-Boundary Correspondence	52
	2.8	Topolo	ogical Classification of Semimetals	59

Die The	
<u>\$</u>	
the	
owledge	
Wir kn	
Z	

	2.9	Quasi 3D Topological Insulators and Surface States	61
3	Res	ults	67
	3.1	Bulk Calculation	67
	3.2	Thin Film Calculation	69
		3.2.1 Bilayer Dependence	71
		3.2.2 Asymmetric Bychkov-Rashba Effect	75
4	Con	clusion	79
5	Арр	endix	83
	5.1	Matrix Elements of the Spin-Orbit Coupling Hamiltonian	83
	5.2	Matrix Elements of the Zeeman Hamiltonian	86
	5.3	Basis Change	87
		5.3.1 Clebsch-Gordan Coefficents	87
	5.4	Matrix Elements of the Bulk Hamiltonian	92
Ri	hliog	ranhy	i

Abstract

This thesis presents a tight-binding study of the formation of the spin-resolved electronic energy band structure of both bulk and thin-film bismuth. We derive the matrix representation of the bulk bismuth Hamiltonian, incorporating spinorbit coupling, the Bychkov-Rashba effect, and the Zeeman effect. We investigate the spin-polarized surface states that emerge at the bismuth-vacuum interface. Our calculations reveal that these surface states exhibit a significant decay length of 40 nm into the bulk, leading to a strong dependence of the system's dispersion on film thickness due to tunneling and hybridization effects between adjacent interfaces.

Our study also highlights several phenomena associated with topological materials. In the symmetric case of the Bychkov-Rashba effect, we identify the emergence of a gapped Dirac fermion in the electron pockets near the Fermi level, perpendicular to the high-symmetry line $\Gamma - M$. Furthermore, we demonstrate that an asymmetric Bychkov-Rashba effect allows for the closing and shifting of this gap in momentum space by tuning the ratio of the electric fields at the top and bottom surfaces, suggesting the potential for a tunable spin current in a spin-field-effect transistor (Spin-FET) device.

We identify the magnitude and ratio of the electric fields at the top and bottom surfaces, respectively, where the Dirac fermion aligns with the Fermi level at the time-reversal-invariant momentum (TRIM) point Γ . Finally, we propose how these theoretical predictions could be tested through in operando electrostatic spin manipulation using spin- and angle-resolved photoemission spectroscopy (SARPES).

Introduction 1

Bismuth, the heaviest stable elethe periodic table, ment in has been a subject of large interest in condensed matter physics and materials science due to its exceptional electronic properties. Initially recognized for its strong diamagnetism. bismuth became ular for its thermoelectric properties, particularly due to its high Seebeck coefficient, as highlighted by Dresselhaus [35]. Its significance grew further following the discovery of topological matter in 2007 [18].



Figure 1.1: Left: A bismuth hopper crystal exhibiting the stairstep crystal structure and iridescent colors, which are produced by interference of light within the oxide film on its surface. Right: A 1 cm³ cube of unoxidised bismuth metal. From [34].

One of bismuth's most remarkable properties is its exceptionally strong spin-orbit coupling (SOC) of $\lambda = 1.5$ eV, the highest among all stable elements [21]. This intrinsic feature makes it a promising candidate for spintronics, a field that seeks to exploit electron spin rather than charge for information processing and storage. Spintronic research aims to develop energy-efficient, high-speed electronic devices by leveraging the spin degree of freedom. Unlike conventional transistors that rely solely on charge transport, spintronic devices manipulate spin states, reducing power consumption and enabling novel computing architectures [23, 6]. Bismuth's unique electronic structure - characterized by low carrier density and high mobility - further enhances its suitability for such applications.

Beyond its role in spintronics, bismuth is integral to the study of topological materials. Bi-based compounds, such as topological insulators (Bi_{1-x}Se_x and Bi₂Te₃), exhibit robust surface states protected by time-reversal symmetry, facilitating dissipationless spin transport [10]. These materials are key candidates for nextgeneration quantum computing and low-energy electronics.

Due to its exceptional spin-orbit coupling, topological characteristics, and potential for energy-efficient spintronic applications, bismuth continues to be a key material in modern electronics and quantum research. Future studies will explore Bi-based heterostructures and novel quantum phases, further establishing its development in spintronic and quantum technologies.

This thesis presents a tight-binding calculation of both the bulk properties of an infinite bismuth crystal and the semi-infinite limit of an N-layer thin film. The aim is to gain deeper insight into the electronic structure of bismuth, particularly in low-dimensional and topological systems.

Chapter 2 provides an overview of the crystallographic properties and electronic structure of bismuth. Chapter 3 introduces the theoretical framework used in this study. The first part of the chapter discusses the tight-binding formalism and the key symmetries of the crystal structure, which give rise to interesting physical phenomena. Furthermore, it explains the implementation of various physical effects, such as spin-orbit coupling, the Zeeman effect, and the Bychkov-Rashba effect, within the tight-binding approach. The second part of Chapter 3 focuses on the concept of topological matter, providing the theoretical background necessary to interpret the results. Chapter 4 presents the findings of the calculations, analyzing the obtained data and discussing their implications. Finally, an outlook is given on how the theoretical results could be verified in future experiments.

By combining tight-binding calculations with a topological perspective, this work aims to contribute to the understanding of bismuth's electronic properties and its potential applications in modern spintronic and quantum technologies.



Theory

The Crystal Structure of Bismuth

The crystalline structure of bismuth exhibits rhombohedral symmetry, with a space group R3m, typical for group V semimetals, like Sb or GaSb. Each atom has three nearest neighbors and three second nearest neighbors slightly farther away, forming a distinct zigzagged bilayer structure of atoms perpendicular to the [1 1 1] direction (see Figure 2.1(c)). Additionally, there are six third nearest neighbors hexagonally arranged in a plane with the central atom.

The bonding within each bilayer is stronger than that between bilayers, and each bilayer connects to the next via the second-nearest neighbors, creating the layered arrangement. Within the unit cell there are two atoms, the second atom positioned in the neighboring bilayer.

Figure 2.1(a) illustrates the rhombohedral system and its three high-symmetry axes C_1, C_2, C_3 . The trigonal axis (C_3) aligns with the origin of the three latticespanning vectors, $\mathbf{a}_1, \mathbf{a}_2, \mathbf{a}_3$. Perpendicular to this axis lies the binary axis (C_2) and the bisectrix (C_1) . The bisectrix (C_1) and the trigonal axis (C_3) span a mirror plane. The Crystal possesses inversion symmetry, a characteristic relevant to spinorbit splitting effects, discussed in Section 2.4.2. Due to the threefold symmetry of the trigonal axis, the binary and bisectrix axes, as well as the mirror plane, appear three times |15|.

If we choose Cartesian coordinates such that the binary (C_2) axis is \hat{x} , the bisectrix (C_1) axis is \hat{y} and the trigonal (C_3) axis is \hat{z} , then the three primitive lattice vectors are given by

$$\mathbf{a}_{1} = \left(-\frac{1}{2}a, -\frac{\sqrt{3}}{6}a, \frac{1}{3}c\right)$$

$$\mathbf{a}_{2} = \left(\frac{1}{2}a, -\frac{\sqrt{3}}{6}a, \frac{1}{3}c\right)$$

$$\mathbf{a}_{3} = \left(0, \frac{\sqrt{3}}{3}a, \frac{1}{3}c\right)$$
(2.1)

These vectors are shown in Figure 2.1(a) as green arrows. Each pair of primitive lattice vectors encloses the rhombohedral angle α . The relative position of the two atoms in the unit cell is given by

$$\mathbf{d}_{1} = (0, 0, \mu)c$$

$$\mathbf{d}_{2} = (0, 0, 1 - \mu)c$$
(2.2)

where μ is the internal displacement parameter. The vectors from the central atom to its nearest neighbors are $\mathbf{a}_i - \mathbf{d}_1$ with $i \in \{1, 2, 3\}$, to the second neighbors $\mathbf{a}_i + \mathbf{a}_j - \mathbf{d}_1$, with $i \neq j \in \{1, 2, 3\}$ and to the third neighbors $\mathbf{a}_i - \mathbf{a}_j$, with $i \neq j \in \{1, 2, 3\}.$

The inter-bilayer and intra-bilayer spacings are given by

$$d_{\text{inter}} = c(\mu - 1/3) = 1.5910 \,\text{Å},$$

 $d_{\text{intra}} = c(2/3 - \mu) = 2.3413 \,\text{Å}$ (2.3)

The crystal structure parameters at 4.2K can be read in Table 2.1.

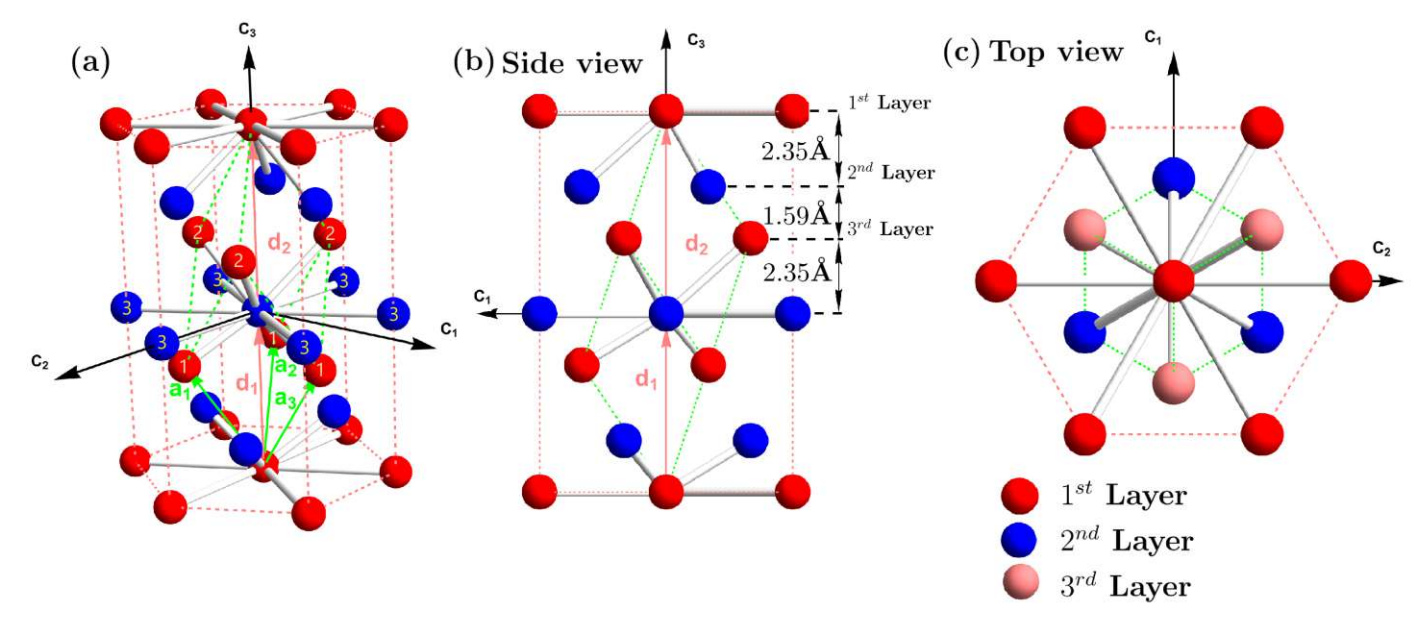


Figure 2.1: (a) Rhombohedral unit cell (green dashed lines). The crystal system can also be described with a hexagonal unit cell (pink dashed lines). The primitive lattice vectors $\mathbf{a}_1, \mathbf{a}_2, \mathbf{a}_3$ are shown with green arrows. The three Cartesian axes are $(C_1,\hat{y}),(C_2,\hat{x}),(C_3,\hat{z})$. The relative position of the second atom in the basis is given by the vector \mathbf{d}_1 and \mathbf{d}_2 respectively. The first, second and third neighbors to the central atom are indicated through numbers. The third neighbors (six in total) lie in plane with the central atom. (b) Side perspective of the crystal structure, highlighting its distinct bilayer nature. The interlayer distance is 2.35Å and the intralayer distance is 1.59Å. (c) Top view of the crystal. The different layers are colour-coded accordingly.

The three corresponding reciprocal lattice vectors to $\mathbf{a}_1, \mathbf{a}_2, \mathbf{a}_3$ are defined through

$$\mathbf{b}_i \cdot \mathbf{a}_j = 2\pi \delta_{ij},\tag{2.4}$$

and are given by

$$\mathbf{b}_{1} = \frac{2\pi}{a}(-1, -1/\sqrt{3}, a/c),$$

$$\mathbf{b}_{2} = \frac{2\pi}{a}(1, -1/\sqrt{3}, a/c),$$

$$\mathbf{b}_{3} = \frac{2\pi}{a}(0, 2/\sqrt{3}, a/c).$$
(2.5)



Table 2.1: Crystal structure parameters of Bi at 4.2K [21].

Lattice constants	a (Å)	4.5332
	c (Å)	11.7967
Rhombohedral angle	α	57.35°
Internal displacement parameter	μ	0.4682
Distance to the next basis atom	d_1 (Å)	5.5232
Nearest-neighbor distance	d' (Å)	3.0624
Next-nearest-neighbor distance	d'' (Å)	3.5120

The Brillouin Zone of the rhombohedral Structure

The Brillouin zone of the rhombohedral structure, constructed using the Voronoi method on the reciprocal lattice, closely resembles the Brillouin zone of an FCC lattice, similar to that of silicon. However, bismuth has a lower symmetry due to the specific rhombohedral angle $\alpha = 57.35^{\circ}$ and displacement parameter $\mu = 0.46$. In contrast, an ideal FCC lattice has parameters of $\alpha = 60^{\circ}$ and $\mu = 0.5$ which contribute to its higher symmetry.

The coordinates of the high-symmetry points within the Brillouin zone, usually straightforward to calculate, are modified by the rhombohedral angle α .

Table 2.2 lists the high-symmetry points in the first Brillouin zone that are most relevant for this thesis. The coordinates of these points depend directly on the rhombohedral angle α [27].

$$\eta = \frac{1 + 4\cos\alpha}{2 + 4\cos\alpha}, \qquad \nu = \frac{3}{4} - \frac{\eta}{2}$$
(2.6)

$\phantom{aaaaaaaaaaaaaaaaaaaaaaaaaaaaaaaaaaa$	$ imes \mathbf{b}_2$	$\times \mathbf{b}_3$		$ imes \mathbf{b}_1$	$ imes \mathbf{b}_2$	\times b ₃	
0	0	0	Γ	η	ν	ν	U
1/2	1/2	0	X	1/2	1/2	1/2	T
1/2	0	0	L	ν	0	$-\nu$	M

Table 2.2: The fractional coordinates of high symmetry points within the rhombohedral structure are presented. From Ref. [27], the author has adopted the nomenclature of these symmetry points.

Figure 2.2 shows a schematic sketch of the Brillouin zone. In summary, there are six rectangular faces with their high symmetry points X situated centrally, six larger hexagonal faces with central high symmetry points L, and two slightly smaller hexagonal faces with central high symmetry points T.

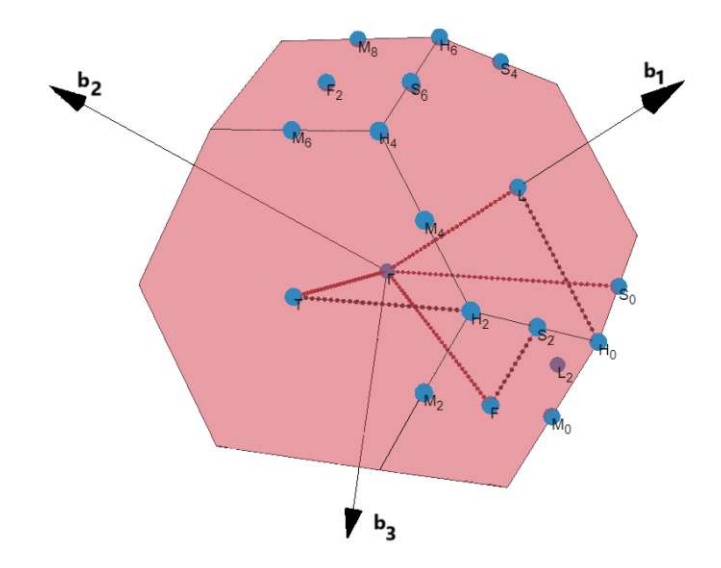


Figure 2.2: The Bulk Brillouin zone of Bismuth. The $\Gamma - T$ line corresponds to the \hat{z} = [1 1 1] direction in real space. The red dashed line indicates the path in k-space used for the bulk tight-binding calculations. The Plot was generated with the tools from Ref. [12, 33]

2.2.1 Thin Film Brillouin Zone of Bismuth(111)

The Brillouin zone of a thin film corresponds to the projection of the bulk Brillouin zone onto the (111)-surface, as shown in Figure 2.3. Photoemission spectra collected at normal emission sample the $\Gamma - T$ direction. The L and X point get projected onto the M point of the 2D Brillouin zone.

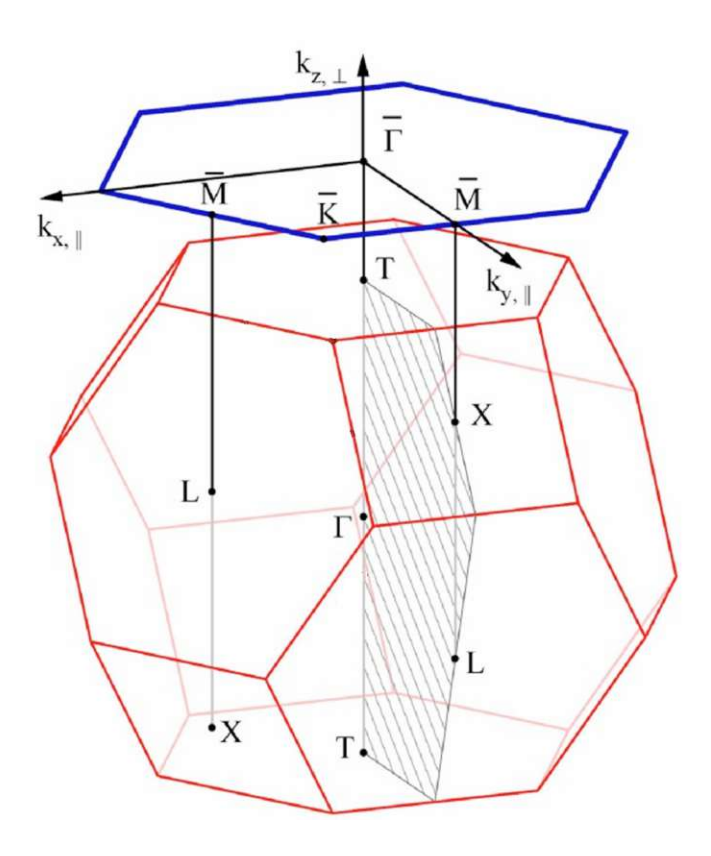


Figure 2.3: The bulk Brillouin zone of bismuth projected onto the (111) surface along with the coordinate system in k-space for the 2D system. The surface Brillouin zone exhibits threefold rotational symmetry and contains three mirror planes. Adapted from Ref. [3].

Tight-Binding Formalism

The tight-binding method is a one-electron model that is used to explain the formation of energy bands in crystals. As the name suggests, this model is suitable for materials where outer electrons remain relatively localized, or "tightly bound", around individual atoms. It is less suitable for cases where electrons are delocalized across the system. Consequently, the tight-binding approach is particularly useful for modeling the electronic bands of covalently bonded materials, where electron wave functions can be approximated by localized atomic wavefunctions at each atomic site.

The starting point is the summation of all atomic Hamiltonians H_{at} pertaining to isolated atoms at site \mathbf{R}_{i} . In addition, we consider the influence of neighboring atoms within a crystal lattice as a small perturbation in the atomic potential, represented by the term ΔU .

$$\hat{H} = \sum_{j} \hat{H}_{\text{at}}^{j} + \Delta U \tag{2.7}$$

Considering that the perturbation is small, the atomic wave functions $|\varphi_n(\mathbf{r} - \mathbf{R}_j)\rangle$ that solve

$$\hat{H}_{\text{at}}^{j} |\varphi_{n}(\mathbf{r} - \mathbf{R}_{j})\rangle = E_{n} |\varphi_{n}\rangle$$
(2.8)

where E_n is the Energy corresponding to the n-th orbital $|\varphi_n\rangle$, are used to construct the wave functions at the site \mathbf{R}_i

$$|\phi_{at}(\mathbf{r} - \mathbf{R}_j)\rangle = \sum_{n} c_n^j |\varphi_n(\mathbf{r} - \mathbf{R}_j)\rangle$$
 (2.9)

The solution to the total Hamiltonian for an arbitrary lattice, such as that of bismuth, is given by a Bloch wave function.

$$|\psi_{\mathbf{k}}^{m}\rangle = \frac{1}{\sqrt{N_{j}}} \sum_{j} \exp(i\mathbf{k} \cdot \mathbf{R}_{j}) |\phi_{at}(\mathbf{r} - \mathbf{R}_{j} - \delta_{m})\rangle$$
 (2.10)



Here, N_j represents the total number of primitive unit cells in the sublattices $(j=1,...,N_{\text{Basis}}\equiv 1,2 \text{ for bismuth})$ in the crystal; $\mathbf{k}=\mathbf{p}/\hbar$ denotes the crystal momentum of the electron; \mathbf{R}_j is the real-space vector pointing to the site j; and δ_m is the displacement vector separating the two basis atoms within the unit cell (cf. Equation 2.2). The complete solution for the crystal arises from the periodicity and symmetry of the system, as it must satisfy Bloch's theorem

$$|\Psi_{\mathbf{k}}(\mathbf{r})\rangle = \sum_{m=1}^{N_{\text{Basis}}} u^m(\mathbf{k})\psi_{\mathbf{k}}^m(\mathbf{r})$$
 (2.11)

We can now solve the Schrödinger equation

$$\langle \Psi_{\mathbf{k}} | \hat{H} | \Psi_{\mathbf{k}} \rangle = \varepsilon \langle \Psi_{\mathbf{k}} | \Psi_{\mathbf{k}} \rangle \tag{2.12}$$

The scalar product $\langle \Psi_{\mathbf{k}} | \Psi_{\mathbf{k}} \rangle$ accounts for the fact that Bloch wave functions are not necessarily normalized. Inserting Equation (2.11) in the Schrödinger equation yields

$$\sum_{m,m'} u^{(m)*}(\mathbf{k}) \left[\left\langle \psi_{\mathbf{k}}^{m} \left| \hat{H} \right| \psi_{\mathbf{k}}^{m'} \right\rangle - \varepsilon \left\langle \psi_{\mathbf{k}}^{m} | \psi_{\mathbf{k}}^{m'} \right\rangle \right] u^{(m')}(\mathbf{k}) = 0$$
 (2.13)

which implies the secular equation

$$det(H_{\mathbf{k}} - \varepsilon S_{\mathbf{k}}) = 0 (2.14)$$

In case the atomic orbitals form an orthonormal basis $S_{\mathbf{k}} = \langle \psi_{\mathbf{k}}^m | \psi_{\mathbf{k}}^{m'} \rangle = \delta_{m,m'}$ Equation (2.13) becomes the solution of the static Schrödinger equation

$$\hat{H}_{\mathbf{k}}|u_n(\mathbf{k})\rangle = \varepsilon_n(\mathbf{k})|u_n(\mathbf{k})\rangle$$
 (2.15)

Here, the periodic Hamiltonian H is replaced by the Bloch Hamiltonian H_k , and the Bloch wave functions are substituted with the Bloch states $|u_n^m(\mathbf{k})\rangle$ where

$$|u_n(\mathbf{k})\rangle = \begin{pmatrix} u_n^{(1)}(\mathbf{k}) \\ \vdots \\ u_n^{(m)}(\mathbf{k}) \\ \vdots \\ u_n^{(N_{\text{basis}})}(\mathbf{k}) \end{pmatrix} \equiv \begin{pmatrix} u_n^{(1)}(\mathbf{k}) \\ u_n^{(2)}(\mathbf{k}) \end{pmatrix}$$
(2.16)

Notice that the index n refers to the n-th eigenstate that is associated with the energy band ε_n , while the index m denotes the sublattice component, which is m=2 for bismuth.

Consider the following orthogonality property, which plays a crucial role in the geometric and topological characterization of Bloch bands in Section 2.7. While the orthogonality of Bloch wave functions at different wave vectors \mathbf{k} and \mathbf{k}' is ensured by the plane-wave factors,

$$\langle \psi_{\mathbf{k}} | \psi_{\mathbf{k}'} \rangle = \delta_{\mathbf{k}, \mathbf{k}'}$$

this is not generally true for the Bloch states,

$$\langle u(\mathbf{k})|u(\mathbf{k}')\rangle \neq \delta_{\mathbf{k},\mathbf{k}'}$$

This lack of orthogonality enables the definition of an evolution for Bloch states within a neighborhood in their associated Hilbert space when exploring the vicinity of a specific wave vector in reciprocal space - something that is not possible for the orthogonal Bloch wave functions. Calculating the matrix elements of $H_{\mathbf{k}}$ in Equation 2.13 is one of the most demanding steps. We can split each matrix element into the sum

$$\langle \psi_{\mathbf{k}}^{m} | \hat{H} | \psi_{\mathbf{k}}^{m'} \rangle = \langle \psi_{\mathbf{k}}^{m} | \hat{H}_{at} | \psi_{\mathbf{k}}^{m'} \rangle + \langle \psi_{\mathbf{k}}^{m} | \Delta U | \psi_{\mathbf{k}}^{m'} \rangle$$
 (2.17)

By substituting our solution from Equation (2.10) into the first term of Equation (2.17) - for brevity, we define $\varphi_n^{jm} \equiv \varphi_n(\mathbf{r} - \mathbf{R}_j - \delta_m)$, where the superscript denotes only spatial dependencies and the subscript only energy-related ones - we obtain the expression

$$\langle \psi_{\mathbf{k}}^{m} | \hat{H}_{at} | \psi_{\mathbf{k}}^{m'} \rangle = \frac{1}{N_{j}} \sum_{j,j',n,n'} c_{n}^{j*} c_{n'}^{j'} e^{i\mathbf{k}(\mathbf{R}_{j'} - \mathbf{R}_{j})} \langle \varphi_{n}^{j,m} | \hat{H}_{at} | \varphi_{n'}^{j',m'} \rangle$$

$$= c_{n}^{2} E_{n} + \frac{1}{N_{j}} \sum_{j \neq j',n,n'} c_{n}^{j*} c_{n'}^{j'} e^{i\mathbf{k}(\mathbf{R}_{j} - \mathbf{R}_{j'})} E_{n'} \langle \varphi_{n}^{j,m} | \varphi_{n'}^{j',m'} \rangle$$

$$= c_{n}^{2} E_{n} + \frac{1}{N_{j}} \sum_{j \neq j',n,n'} c_{n}^{j*} c_{n'}^{j'} e^{i\mathbf{k}(\mathbf{R}_{j} - \mathbf{R}_{j'})} E_{n'} \alpha_{n,n'}^{j,j',m,m'}$$

$$(2.18)$$

The overlap integral between different atomic wave functions is given by

$$\alpha_{n,n'} = \int d\mathbf{r} \, \varphi_n(\mathbf{r} - \mathbf{R}_j - \delta_m)^* \varphi_{n'}(\mathbf{r} - \mathbf{R}_{j'} - \delta_{m'})$$
 (2.19)

which corresponds to the matrix elements of $S_{\mathbf{k}}$. These elements are set to zero, as we neglect the (exponentially suppressed) overlap between atoms at different lattice sites. Performing the same calculation for the second summand in (2.17) we obtain

$$\langle \psi_{\mathbf{k}}^{m} | \Delta U | \psi_{\mathbf{k}}^{m'} \rangle = \frac{1}{N_{j}} \sum_{i,i',n,n'} c_{n}^{j*} c_{n'}^{j'} e^{i\mathbf{k}(\mathbf{R}_{j'} - \mathbf{R}_{j})} \langle \varphi_{n}^{j,m} | \Delta U | \varphi_{n'}^{j',m'} \rangle$$
(2.20)

$$= \sum_{n,n'} c_n^* c_{n'} \langle \varphi_n^{j,m} | \Delta U | \varphi_{n'}^{j,m} \rangle + \frac{1}{N_j} \sum_{j \neq j',n,n'} c_n^{j*} c_{n'}^{j'} e^{i\mathbf{k}(\mathbf{R}_{j'} - \mathbf{R}_j)} \langle \varphi_n^{j,m} | \Delta U | \varphi_{n'}^{j',m'} \rangle \quad (2.21)$$

$$= \sum_{n,n'} c_n^* c_{n'} \beta_{n,n'} + \frac{1}{N} \sum_{j \neq j',n,n'} c_n^{j*} c_{n'}^{j'} e^{i\mathbf{k}(\mathbf{R}_{j'} - \mathbf{R}_j)} t_{n,n'}$$
(2.22)

where $t_{n,n'}$ denotes the transfer (hopping) integral, and $\beta_{m,n}$ represents a lattice contribution

$$\beta_{n,n'} = \int d\mathbf{r} \, \varphi_n(\mathbf{r})^* \Delta U \varphi_{n'}(\mathbf{r})$$
 (2.23)

$$t_{n,n'}(\mathbf{R}) = \int d\mathbf{r} \, \varphi_n(\mathbf{r} - \mathbf{R}_j - \delta_m)^* \Delta U \varphi_{n'}(\mathbf{r} - \mathbf{R}_{j'} - \delta_{m'})$$
 (2.24)

The lattice contribution $\beta_{n,n'}$ can be used as an additional fitting parameter. However, because we assume that the perturbation ΔU is very small, $\beta_{n,n'}$ is typically set to zero. Larger values of $\beta_{n,n'}$ would imply a stronger perturbation, for which the tight-binding formalism breaks down. We further assumed that the electrons are tightly bound (localized), meaning their wave functions decay rapidly with increasing distance $|\mathbf{R}|$. This allows us to restrict the summation in Equation (2.22) to a smaller finite range. For simple systems, summing over only the nearest neighbors is often sufficient. In this work, however, we include contributions up to the third-nearest neighbors.

In theory, the calculations are completed, but fitting experimental data to such an extensive parameter space is challenging. The number of fitting parameters grows with the inclusion of more orbitals and atoms in the unit cell. For bismuth, we use one s orbital and three p orbitals per atom, with two atoms in the basis. When including spin, the Hamiltonian becomes a 16×16 matrix, resulting in $\frac{1}{2}(16 \cdot 16)$ fitting parameters. Fortunately, there already exists a solution to this problem.

2.3.1 Slater-Koster Two-Center Approximation

In their famous paper from 1954 [30] Slater and Koster introduced an elegant method to drastically reduce the number of fitting parameters. Instead of calculating every individual two center integral

$$t_{n,n'} = \langle \varphi_n^{j,m} | \Delta U | \varphi_{n'}^{j',m'} \rangle \tag{2.25}$$

from Equation 2.22, we can express it as a linear combination of σ and π bonds, corresponding to their respective bonding directions, as illustrated in Figure 2.4.

In order to express (2.25) as a linear combination of the bonds σ and π , we need to project $|\varphi_n\rangle$ onto $\{|\varphi_{n,\sigma}\rangle, |\varphi_{n,\pi}\rangle\}$ using the projector

$$\widehat{P}_{n} = |\varphi_{n,\sigma}\rangle \langle \varphi_{n,\sigma}| + |\varphi_{n,\pi}\rangle \langle \varphi_{n,\pi}|$$
(2.26)

and take the resulting $\langle \varphi_{m,\sigma} | \Delta U | \varphi_{n,\sigma} \rangle$, $\langle \varphi_{m,\pi} | \Delta U | \varphi_{n,\pi} \rangle$ as new fit parameters.

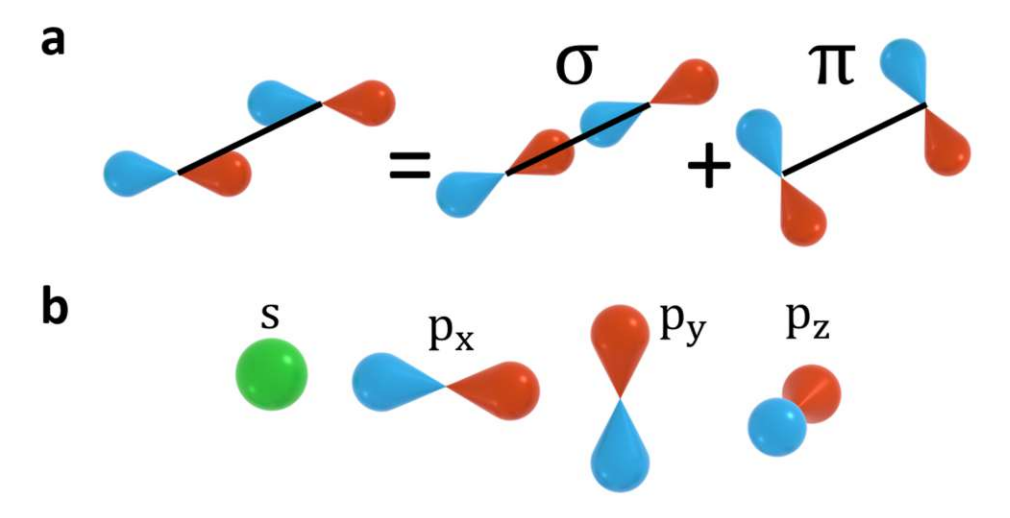


Figure 2.4: (a) Illustration showing how the overlap between two p orbitals can be represented as a linear combination of σ and π bonds. (b) Schematic depitction of the used set of orbitals. The color denotes the sign of the wavefunction (blue for positive and red for negative). The s orbital doesn't change in sign. Adapted from Ref. [7].

Mixed terms like $\langle \varphi_{m,\sigma} | \Delta U | \varphi_{n,\pi} \rangle$ are zero due to symmetry. The result reads as

$$\langle \varphi_{m} | \Delta U | \varphi_{n} \rangle = \langle \varphi_{m} | \hat{P}_{m} \Delta U \hat{P}_{n} | \varphi_{n} \rangle$$

$$= \langle \varphi_{m} | \varphi_{m,\sigma} \rangle \langle \varphi_{m,\sigma} | \Delta U | \varphi_{n,\sigma} \rangle \langle \varphi_{n,\sigma} | \varphi_{n} \rangle$$

$$+ \langle \varphi_{m} | \varphi_{m,\pi} \rangle \langle \varphi_{m,\pi} | \Delta U | \varphi_{n,\pi} \rangle \langle \varphi_{n,\pi} | \varphi_{n} \rangle$$

$$= aV_{mn\sigma} + bV_{mn\pi}$$
(2.27)

where a and b are known constants, calculated by the projection of atomic orbitals onto the bonding-orbitals. $V_{mn\sigma} \& V_{mn\pi}$ are the new fit parameters [7]. The advantage is that the parameters $V_{mn\sigma}$ & $V_{mn\pi}$ only depend on the distance between sites, but not on the direction, which removes the dependence of the direction of the fitting parameter. This allows us to set one V_{mni} for each neighbor-distance.

2.4 Symmetries and Spin-Orbit Coupling

The following section is based on the lecture notes "Introduction to Quantum" Mesoscopic Transport and Topological Matter" by Prof. Mark Oliver Goerbig [10], which were kindly provided to the author. His lecture notes offer an excellent introduction to the topic of topological matter.

2.4.1 Kramer's Theorem and Time-Reversal Symmetry

Kramer's theorem states that electrons, or more generally fermions with halfinteger spin, occur in pairs in time-reversal systems.

Let's briefly review the fundamental properties of time-reversal symmetry. Under time reversal, time t transforms as $t \to -t$, while position **r** remains unchanged, ${f r}
ightarrow {f r}$. In quantum systems, these quantities correspond to observables, which are represented by Hermitian operators that act on states within a Hilbert space. Consequently, transformations, including time reversal, are also represented by operators, which act on these observables.

Under a time-reversal transformation T, an observable \mathcal{O} and its corresponding eigenstate $|\psi\rangle$ transform as follows

$$\mathcal{O}' = T\mathcal{O}T^{-1}$$

$$|\psi'\rangle = T |\psi\rangle \tag{2.28}$$

If we let T act on the spin-1/2 Bloch bands described by the time-reverse symmetric Hamiltonian $H(\mathbf{k}, s)$, where **k** denotes the crystal momentum of the electrons and $s = \uparrow, \downarrow$ the spin orientations, we find

$$TH(\mathbf{k},\uparrow)T^{-1} = H(-\mathbf{k},\downarrow) = H(\mathbf{k},\uparrow)$$

$$T|\psi(\mathbf{k},\uparrow)\rangle = |\psi(-\mathbf{k},\downarrow)\rangle$$
(2.29)





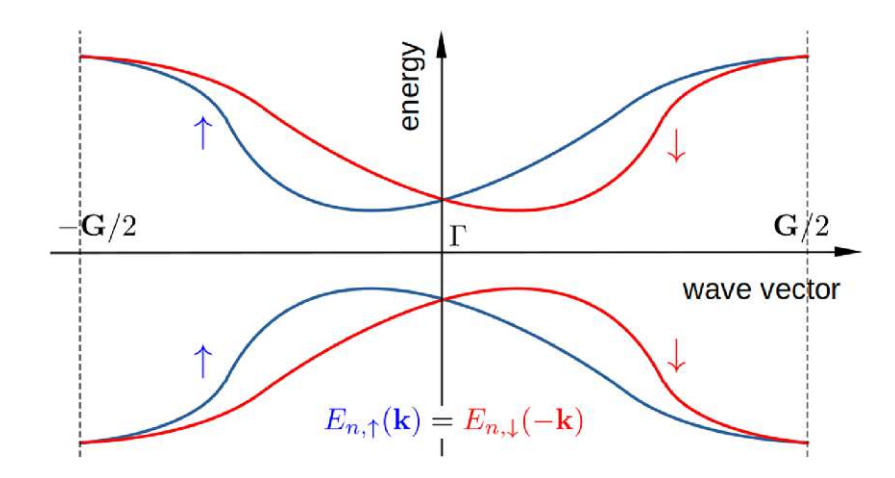


Figure 2.5: Illustration of Kramer's theorem for bands with a time-reverse-symmetric Hamiltonian. Generally, the two fold degeneracy is lifted, with exception of the timereversal-invariant-momenta (TRIM), where the two spin branches (blue for spin up \uparrow and red for spin down \downarrow). The TRIM are the Γ and points G/2 at the edge of the Brillouin zone. The branches respect the symmetry $E(\mathbf{k},\uparrow) = E(-\mathbf{k},\downarrow)$. From Ref. [10].

As a consequence, the eigenstates $|\psi(\mathbf{k},\uparrow)\rangle$ and $|\psi(-\mathbf{k},\downarrow)\rangle$ yield the same energy,

$$E(\mathbf{k},\uparrow) = E(-\mathbf{k},\downarrow)$$
 (2.30)

This symmetry is depicted in Figure 2.5, where the energy bands are generally split and the two-fold degeneracy is lifted. However, there are special points - called time-reversal-invariant-momenta (TRIM) - within the first Brillouin zone, where the bands are necessarily twofold degenerate. One obvious point is the Γ point at $\mathbf{k} = 0$, where $E(0,\uparrow) = E(0,\downarrow)$. We can generalize this fact by recalling that the spectrum is periodic in reciprocal space and that two points are equivalent if they are related by the reciprocal lattice vector G,

$$\mathbf{k} \to \mathbf{k} + \mathbf{G}, \quad E(\mathbf{k}, s) = E(\mathbf{k} + \mathbf{G}, s)$$
 (2.31)

The bands have crossing points at the wave vectors

$$\mathbf{k}_{\text{TRIM}} = -\mathbf{k}_{\text{TRIM}} + \mathbf{G} \quad \Leftrightarrow \quad \mathbf{k}_{\text{TRIM}} = \frac{\mathbf{G}}{2}$$
 (2.32)

which equals to the edge of the Brillouin zone.

2.4.2 Spin-Orbit Coupling and Inversion Symmetry

In order to lift the spin degeneracy as described and let the spin-up electrons move differently in the crystal than spin-down electrons, we need to introduce a spin-dependent hopping parameter to our total tight-binding Hamiltonian in Equation (2.7). This is achieved by considering spin-orbit coupling (SOC).

An electron with crystal momentum \vec{k} moving in an electric field \vec{E} caused by atomic nuclei, experiences a internal magnetic field \vec{B}_{int} in its rest frame

$$\vec{B}_{int} \propto \vec{E} \times \vec{k}$$
 (2.33)

The energy of a magnetic moment $\vec{\mu}$ in a magnetic field is given by

$$H = -\vec{\mu} \cdot \vec{B}_{int} \tag{2.34}$$

where $\vec{\mu} = \frac{1}{2}g\mu_B\vec{\sigma}$. This leads to

$$H_{\rm SOC} \propto \vec{\sigma} \cdot (\vec{E} \times \vec{B}_{int}) = \vec{\sigma} \cdot (\vec{\nabla} V \times \vec{B}_{int})$$
 (2.35)

where $\vec{\sigma} = (\hat{\sigma}_x, \hat{\sigma}_y, \hat{\sigma}_z)$ denotes the spin orientation of the moving electron. We assume that the atomic potential is spherically symmetric and we can use

$$\vec{\nabla}V = \frac{\partial V}{\partial r}\frac{\vec{r}}{r} \tag{2.36}$$

Substituting this expression into (2.35), we can rewrite the Hamiltonian

$$H_{\rm SOC} \propto \frac{1}{r} \frac{\partial V}{\partial r} \vec{\sigma} \cdot (\vec{r} \times \vec{k}) = \lambda_{SOC} \left(\vec{\sigma} \cdot \vec{L} \right)$$
 (2.37)

where we used the definition of the angular momentum $\vec{L} = \vec{r} \times \vec{k}$ and introduced the spin-orbit coupling strength λ_{SOC} as an additional fitting parameter. A detailed derivation of the matrix elements for the SOC Hamiltonian is provided in Appendix 5.1, where each step of the calculation is elaborated for clarity.



The SOC Hamiltonian respects the time-reversal symmetry, given by $TH_{\rm SOC}T^{-1}=$ $H_{\rm SOC}$, because it is proportional to the product of the electron spin and angular momentum, both of which are odd under the time-reversal transformation, while the atomic potential V remains even.

The coupling strength λ_{SOC} increases with heavier atoms due to the dependence of the atomic potential gradient V on the atomic number Z. Although bismuth exhibits a very large SOC coupling ($\lambda_{SOC} = 1.5 \,\text{eV}$), no band splitting is observed in bulk calculations [21]. This lack of splitting is a direct consequence of bulk inversion symmetry [15], as discussed in Section 2.1. In systems with inversion symmetry the energy at point \vec{k} is equal to the energy at point $-\vec{k}$ without influencing the electrons spin s

$$E(\vec{k}, s) = E(-\vec{k}, s)$$
 (2.38)

Combining time-reversal symmetry and inversion symmetry, we end up with

$$\underbrace{E(\mathbf{k},\uparrow) = E(-\mathbf{k},\downarrow)}_{\text{Inversion symmetry}} = \underbrace{E(-\mathbf{k},\downarrow) = E(\mathbf{k},\downarrow)}_{\text{Inversion symmetry}}$$
(2.39)

resulting in bands without spin splitting. A detailed analysis of spin-orbit splitting on surfaces, where the inversion symmetry is broken, will follow in Section 2.6.2.

2.4.3 Zeeman Effect

The fact that each energy band is doubly degenerate makes a numerical analysis of spin projections along a specific path in the Brillouin zone impossible. In the numerical analysis, each band appears with a non-continuous spin flipping.

We can circumvent this issue by applying an artificial external magnetic field to compensate for the not occurring spin-orbit (SOC) splitting, as depicted in Figure 2.6. In reality, this could be achieved by depositing Bi onto a magnetic substrate, such as Ni. The following derivation is adapted from Griffiths' book "Introduction to quantum mechanics" [11].

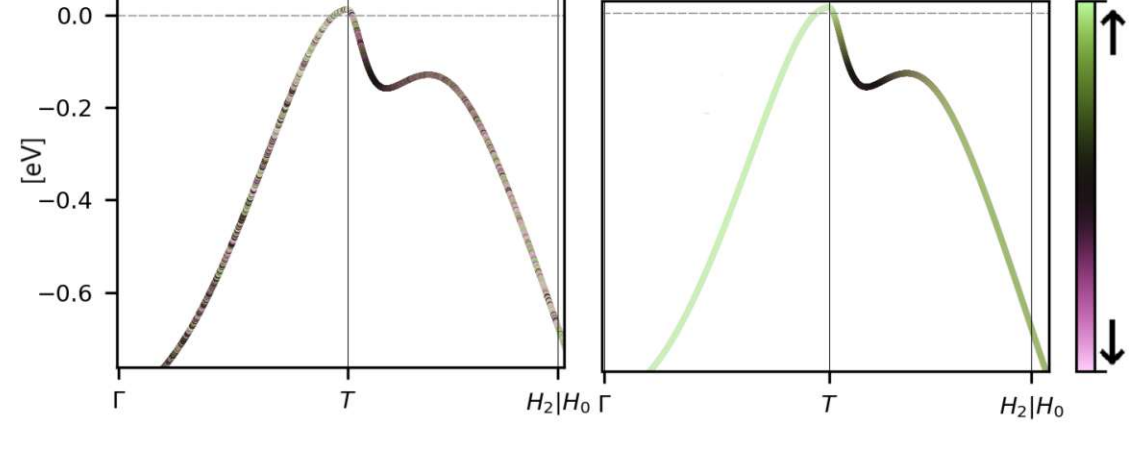


Figure 2.6: Spin projection onto the \hat{z} -axis of the valence band along an arbitrary path before (left) and after (right) applying a weak external magnetic field \vec{B}_{ext} . Although spin-orbit coupling (SOC) is taken into account, the band remains two-fold degenerate due to bulk inversion symmetry. This is reflected in the non-continuous spin flipping. The degeneracy is lifted when a magnetic field is applied, leading to a continuous spin change along the path.

When an atom is placed in a uniform external magnetic field \vec{B}_{ext} , the electron experiences an energy shift

$$H_z = -(\vec{\mu}_l + \vec{\mu}_s) \cdot \vec{B}_{\text{ext}} \tag{2.40}$$

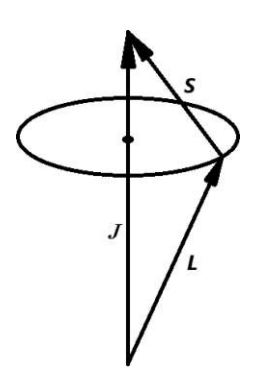
where $\vec{\mu}_s = -(e/m)\vec{S}$ is the magnetic moment of the electrons spin and $\vec{\mu}_l =$ $(e/2m)\vec{L}$ the magnetic moment corresponding to its orbital motion, which leads to

$$H_z = \frac{e}{2m}(\vec{L} + 2\vec{S}) \cdot \vec{B}_{\text{ext}}$$
 (2.41)

In case the external magnetic field is much smaller than the internal field, $\vec{B}_{\rm ext} \ll \vec{B}_{\rm int}$, the Zeeman effect can be viewed as a small perturbation to $H_{\rm SOC}$ in Equation (2.37).



Weak-Field Zeeman Effect



When the external magnetic field $\vec{B}_{\rm ext}$ is much smaller than the internal magnetic field $\vec{B}_{\rm int}$, the appropriate quantum numbers are n, l, j, and m_i . However, m_l and m_s are no longer good quantum numbers because, due to spin-orbit coupling (SOC), the orbital angular momentum \vec{L} and spin angular momentum \vec{S} are not conserved independently. Using first-order perturbation theory, the Zeeman correction to the energy is given by

 $\langle n, l, j, m_j | \hat{H}_Z | n, l, j, m_j \rangle = \frac{e}{2m_e} \vec{B}_{\text{ext}} \cdot \langle \vec{L} + 2\vec{S} \rangle$ (2.42)

Figure 2.7: In the presence of SOC, \vec{L} and \vec{S} are not individually They conserved. precess around the conserved total angular

momentum \vec{J} .

To find the expectation value we need to simplify this expression, using the identity

$$\vec{L} = \vec{J} - \vec{S}$$
 \Rightarrow $\vec{L} + 2\vec{S} = \vec{J} + \vec{S}$ (2.43)

which allows us to express the Zeeman correction in terms of the total angular momentum operator \vec{J} and \vec{S} , eliminating \vec{L} from the expression. Although we do not directly know the expectation value of \vec{S} , it can be determined as follows: Since \vec{L} and \vec{S} precess (see Figure 2.7) around the vector of total angular momentum \vec{J} , the time-averaged expectation value of \vec{S} is simply its projection along \vec{J}

$$\vec{S}_{\text{average}} = \frac{\vec{J} \cdot \vec{S}}{J^2} \vec{J} \tag{2.44}$$

To find $\vec{J} \cdot \vec{S}$, we square the identity for \vec{L} from (2.43):

$$L^{2} = J^{2} + S^{2} - 2\vec{J} \cdot \vec{S},$$

$$\Rightarrow \vec{J} \cdot \vec{S} = \frac{1}{2} (J^{2} + S^{2} - L^{2}).$$
(2.45)



From which follows

$$\langle \vec{J} + \vec{S} \rangle = \langle \left(1 + \frac{\vec{J} \cdot \vec{S}}{J^2} \right) \cdot \vec{J} \rangle = \langle \left(1 + \frac{\hat{J}^2 + \hat{S}^2 - \hat{L}^2}{2\hat{J}^2} \right) \cdot \vec{J} \rangle$$
 (2.46)

$$= \left[1 + \frac{j(j+1) + 3/4 - l(l+1)}{2j(j+1)}\right] \langle \vec{J} \rangle$$
 (2.47)

The term in the square brackets is called Landè g-factor, g_j . If we now choose the \hat{z} -axis along which we apply the magnetic field $\vec{B}_{ext} = (0, 0, \vec{B}_z^{ext})$, we can immediately calculate the zeemann correction

$$E_Z = \mu_B g_i B_z^{\text{ext}} m_i \tag{2.48}$$

where $\mu_B = e\hbar/2m = 5.788 \times 10^{-5} eV/T$ is the Bohr magneton and m_i is the expectation value of the total angular momentum projected onto the \hat{z} -axis. A detailed derivation of the matrix elements for the Zeeman Hamiltonian is provided in Appendix 5.2, where each step of the calculation is elaborated for clarity.

To apply this approach, we must estimate what constitutes a weak magnetic field. Consider an electron orbiting the nucleus, generating a magnetic field due to the resulting current. The magnetic field, \mathbf{B} , at a distance r from the nucleus is given by:

$$\mathbf{B} = \frac{1}{4\pi\epsilon_0} \frac{e}{mc^2 r^3} \mathbf{L} \tag{2.49}$$

where e is the electron charge, m is the electron mass, c is the speed of light, and L represents the angular momentum of the electron.

To estimate the magnitude of **B**, we substitute the Bohr radius, $r = a_0$, and set $\mathbf{L} = \hbar$, obtaining $\mathbf{B} \approx 12 \,\mathrm{T}$. In comparison, Earth's magnetic field, $\mathbf{B} = 10^{-4} \,\mathrm{T}$, is much smaller. Thus, Earth's magnetic field can be considered a weak external field, which will be used for the further analysis.



Basis Change 2.5

To carry out calculations on bulk and surface bismuth, we must first note that the Hamiltonian for the spin-orbit coupling (SOC), H_{SOC} , and the Hamiltonian for the Zeeman correction, H_Z , are defined in different Hilbert spaces from the tight-binding Hamiltonian, H_{TB} .

While the tight-binding Hamiltonian is defined based on real atomic wave functions, the SOC Hamiltonian uses complex atomic wave functions as its basis and the Zeeman Hamiltonian is defined using total angular momentum eigenstates as its basis.

These differences in basis make it necessary to perform a basis transformation on H_{SOC} and H_Z to align them with the basis of H_{TB} . This transformation is a standard problem in linear algebra, which we solve by expressing vectors of the old basis $\mathbf{b}_j \in B$ in terms of vectors in the new basis $\mathbf{b}_i' \in B'$

$$\mathbf{b}_j = \sum_{i=1}^n t_{ij} \mathbf{b}_i' \tag{2.50}$$

where each element \mathbf{b}_{j} is mapped through a linear combination of \mathbf{b}'_{i} . The coefficients t_{1j}, \ldots, t_{nj} form the j-th column of the change-of-basis matrix

$$T_{B'}^{B} = \begin{bmatrix} t_{11} & \cdots & t_{1j} & \cdots & t_{1n} \\ \vdots & \ddots & \vdots & \ddots & \vdots \\ t_{n1} & \cdots & t_{nj} & \cdots & t_{nn} \end{bmatrix}$$
 (2.51)

Its inverse $(T_{B'}^B)^{-1} = T_B^{B'}$ describes the change of basis from B' back to B. Our approach is as follows: we first transform the basis of H_Z to match that of the SOC Hamiltonian and add it to H_{SOC} . Then, we perform a basis transformation on this combined Hamiltonian to align it with the basis of H_{TB} , resulting in the final Hamiltonian:

$$H = H_{TB} + T_{xyz}^{nlm} \cdot \left(H_{SOC} + T_{nlm}^J \cdot H_Z \cdot \left(T_{nlm}^J \right)^{-1} \right) \cdot \left(T_{xyz}^{nlm} \right)^{-1} \tag{2.52}$$



2.5.1 Clebsch-Gordan Coefficents

In the first step, we focus on the expression

$$T_{nlm}^J \cdot H_Z \cdot \left(T_{nlm}^J\right)^{-1} \tag{2.53}$$

from Equation (2.52), where we aim to express the matrix elements of the Zeeman correction in terms of complex atomic wave functions.

For the basis of H_Z , we have chosen the eigenstates of the total angular momentum, $|n,l,j,m_j\rangle$, which we will abbreviate as $|j,m\rangle$ for simplicity.

In the basis of complex atomic wave functions, the electron has a defined orbital angular momentum l=1,2 (6s and 6p orbitals) and a fixed spin s=1/2. We denote the eigenstates of this basis as $|n, l, m_l, s, m_s\rangle$, or simply $|m_l, m_s\rangle$, where $-l < m_l < l \text{ and } -s < m_s < s.$

As stated in Equation (2.50), we want to express a vector $|j,m\rangle$ as a linear combination of $|m_l, m_s\rangle$ to find the coefficients for the transformation matrix. This is achieved using the projection \hat{P}

$$\hat{P} = \sum_{m_l=-l}^{l} \sum_{m_s=-s}^{s} |m_l, m_s\rangle \langle m_l, m_s| \qquad (2.54)$$

where we derive

$$|j,m\rangle = \sum_{m_l=-l}^{l} \sum_{m_s=-s}^{s} \langle m_l, m_s | j, m \rangle | m_l, m_s \rangle = \sum_{m_l=-l}^{l} \sum_{m_s=-s}^{s} C(j, m | m_l, m_s) | m_l, m_s \rangle$$

$$(2.55)$$

The coefficients $C(j, m|m_l, m_s)$, referred to as Clebsch-Gordan coefficients, are the same as those defined in Equation (2.51).

To construct this linear combination of eigenstates, we will use the properties of the operators \hat{J} , \hat{L} , and $\hat{\sigma}$, as well as the ladder operators \hat{L}_{\pm} and $\hat{\sigma}_{\pm}$, which were previously used to calculate the matrix elements of the SOC Hamiltonian in Section 5.1.



We will use the following relations:

$$\hat{L}^2|m_l, m_s\rangle = l(l+1)|m_l, m_s\rangle, \quad \hat{L}_z|m_l, m_s\rangle = m_l|m_l, m_s\rangle$$
 (2.56)

$$\hat{\sigma}^2|m_l, m_s\rangle = s(s+1)|m_l, m_s\rangle, \quad \hat{\sigma}_z|m_l, m_s\rangle = m_s|m_l, m_s\rangle$$
 (2.57)

as well as

$$\hat{L}_{\pm} | m_l, m_s \rangle = \sqrt{l(l+1) - m_l(m_l \pm 1)} | m_l \pm 1, m_s \rangle$$

$$\hat{\sigma}_{\pm} | m_l, m_s \rangle = \sqrt{s(s+1) - m_s(m_s \pm 1)} | m_l, m_s \pm 1 \rangle$$
(2.58)

$$\hat{L}_{z} |m_{l}, m_{s}\rangle = m_{l} |m_{l}, m_{s}\rangle$$

$$\hat{\sigma}_{z} |m_{l}, m_{s}\rangle = m_{s} |m_{l}, m_{s}\rangle$$
(2.59)

Calculating the Clebsch-Gordan Coefficients

Starting from the extremal state, defined by $\hat{J}_{+}|j_{\text{max}},m_{\text{max}}\rangle=0$ with $\hat{J}_{+} = \hat{L}_{+} + \hat{\sigma}_{+}$, we have a well defined relation of the eigenstates in the two Hilbert spaces

$$|j_{\text{max}}, m_{\text{max}}\rangle = |m_l = l, m_s = s\rangle \tag{2.60}$$

with eigenvalues:

$$\hat{J}_{z} |j_{\max}, m_{\max}\rangle = (\hat{L}_{z} + \hat{\sigma}_{z}) |m_{l} = l, m_{s} = s\rangle
= (l+s) |m_{l} = l, m_{s} = s\rangle
= (l+s) |j_{\max}, m_{\max}\rangle
= m_{\max} |j_{\max}, m_{\max}\rangle$$
(2.61)

and

26

$$\hat{J}^{2} | j_{\text{max}}, m_{\text{max}} \rangle = (\hat{L} + \hat{\sigma})^{2} | m_{l} = l, m_{s} = s \rangle
= (\hat{L}^{2} + \hat{\sigma}^{2} + 2\hat{L} \cdot \hat{\sigma}) | m_{l} = l, m_{s} = s \rangle
= (\hat{L}^{2} + \hat{\sigma}^{2} + \hat{L}_{+}\hat{\sigma}_{-} + \hat{L}_{-}\hat{\sigma}_{+} + 2\hat{L}_{z}\hat{\sigma}_{z}) | m_{l} = l, m_{s} = s \rangle
= (\hat{L}^{2} + \hat{\sigma}^{2} + 2\hat{L}_{z}\hat{\sigma}_{z}) | m_{l} = l, m_{s} = s \rangle
= (l(l+1) + s(s+1) + 2ls) | j_{\text{max}}, m_{\text{max}} \rangle
= (l+s) ((l+s+1)) | j_{\text{max}}, m_{\text{max}} \rangle
= j_{\text{max}}(j_{\text{max}} + 1) | j_{\text{max}}, m_{\text{max}} \rangle$$

where we derive the important relations $m_{\text{max}} = l + s$ and $j_{\text{max}} = l + s$.

The state $|j_{\text{max}}, m_{\text{max}} - 1\rangle = |l + s, l + s - 1\rangle$ can be obtained by applying \hat{J}_{-} :

$$\hat{J}_{-}|j,m\rangle = \sqrt{j(j+1) - m(m-1)}|j,m-1\rangle$$
 (2.63)

$$\Rightarrow \hat{J}_{-}|j_{\text{max}}, m_{\text{max}}\rangle = \sqrt{2(l+s)}|j_{\text{max}}, j_{\text{max}} - 1\rangle$$
 (2.64)

Using $\hat{J}_{-} = \hat{L}_{-} + \hat{\sigma}_{-}$, we find

$$\hat{J}_{-}|j_{\max},j_{\max}\rangle = (\hat{L}_{-} + \hat{\sigma}_{-})|m_{l} = l, m_{s} = s\rangle
= \sqrt{2l}|m_{l} = l - 1, m_{s} = s\rangle + \sqrt{2s}|m_{l} = l, m_{s} = s - 1\rangle$$
(2.65)

Comparing the coefficients of Equation (2.64) and Equation (2.65) we find

$$|j_{\text{max}}, j_{\text{max}} - 1\rangle = \sqrt{\frac{l}{l+s}} |m_l = l-1, m_s = s\rangle + \sqrt{\frac{s}{l+s}} |m_l = l, m_s = s-1\rangle$$

We continue this procedure repeatedly until we achieve $m = -j_{\text{max}}$. This approach enables us to determine all necessary coefficients for

$$|j_{\text{max}}, m\rangle, \quad -j_{\text{max}} \le m \le j_{\text{max}}$$
 (2.66)



Next, we want to find the states $|j_{\text{max}} - 1, m\rangle$ where $-|j_{\text{max}} - 1| \le m \le j_{\text{max}} - 1$. Through $m = m_l + m_s$, we see that the maximum value $m = j_{\text{max}} - 1 = l + s - 1$ must be a linear combination of $|m_l = l, m_s = s - 1\rangle$ and $|m_l = l - 1, m_s = s\rangle$. This state must be orthogonal to $|j_{\text{max}}, j_{\text{max}} - 1\rangle$. We write the state as

$$|j_{\text{max}} - 1, j_{\text{max}} - 1\rangle = \alpha |m_l = l - 1, m_s = s\rangle + \beta |m_l = l, m_s = s - 1\rangle,$$
 (2.67)

with the normalization condition $|\alpha|^2 + |\beta|^2 = 1$. Calculating the inner product with $|j_{\max}, j_{\max} - 1\rangle$, we find

$$0 = \langle j_{\text{max}}, j_{\text{max}} - 1 | j_{\text{max}} - 1, j_{\text{max}} - 1 \rangle = \alpha \sqrt{\frac{l}{l+s}} + \beta \sqrt{\frac{s}{l+s}}$$
 (2.68)

Solving for α and β using the orthogonality condition together with the normalization condition, we obtain:

$$\alpha = \sqrt{\frac{s}{l+s}}, \quad \beta = -\sqrt{\frac{l}{l+s}} \tag{2.69}$$

Thus, we can express the state $|j_{\text{max}} - 1, j_{\text{max}} - 1\rangle$ as

$$|j_{\text{max}} - 1, j_{\text{max}} - 1\rangle = \sqrt{\frac{s}{l+s}} |m_l = l-1, m_s = s\rangle - \sqrt{\frac{l}{l+s}} |m_l = l, m_s = s-1\rangle$$

From this state, we can obtain all other states $|j_{\text{max}}-1,m\rangle$ by applying the lowering operator J_{-} as before, where

$$-(j_{\max} - 1) \le m \le (j_{\max} - 1) \tag{2.70}$$

Following the same procedure, we calculate the states $|j_{\text{max}}-2,m\rangle$, and so on. After several iterations, we reach $j = j_{\min}$, at which point the constructed states span the entire Hilbert space.

An explicit calculation of the Clebsch-Gordan coefficients for the transformation matrix is provided in Appendix 5.3.1, where each step of the calculation is detailed for clarity.

2.5.2 From Complex to Real Atomic Wave Functions

After the transformation of the Zeeman correction into the basis of complex atomic wave functions, we can address the term

$$T_{xyz}^{nlm} \cdot H_{SOC} \cdot \left(T_{xyz}^{nlm}\right)^{-1} \tag{2.71}$$

from Equation (2.52). Now we must find the transformation T^{nlm}_{xyz} from the complex atomic wave functions $\psi_{n,l,m}\chi_{m_s} = |n,l,m_l,m_s\rangle$ to real atomic wave functions. In this context, we represent the spin-dependent component of the wave function by χ . The basis for our complex wave functions was defined as follows

$$B_{\text{SOC}} = \left\{ \left| s, 0, \frac{1}{2} \right\rangle, \left| s, 0, -\frac{1}{2} \right\rangle, \left| p, -1, \frac{1}{2} \right\rangle, \left| p, 0, \frac{1}{2} \right\rangle, \left| p, 1, \frac{1}{2} \right\rangle, \left| p, -1, -\frac{1}{2} \right\rangle, \left| p, 0, -\frac{1}{2} \right\rangle, \left| p, -1, -\frac{1}{2} \right\rangle \right\}$$

where we have omitted the principal quantum number n=6 for brevity. Following the Condon-Shortley phase convention [9] the relation between complex and real atomic orbital functions is given by

$$\psi_{nlm}^{real} = \begin{cases}
\frac{i}{\sqrt{2}} \left(\psi_{n,\ell,-|m|} - (-1)^m \psi_{n,\ell,|m|} \right) & \text{for } m < 0 \\
\psi_{n,\ell,|m|} & \text{for } m = 0 \\
\frac{1}{\sqrt{2}} \left(\psi_{n,\ell,-|m|} + (-1)^m \psi_{n,\ell,|m|} \right) & \text{for } m > 0
\end{cases}$$
(2.72)

For the 6s-orbitals the relation is trivial, since $l=m_l=0$

$$\psi_{6,0,0}\chi_{m_s} = \psi_{6,0,0}^{real}\chi_{m_s} := |s, m_s\rangle$$
(2.73)

For the 6p-orbitals, the real wave functions are defined as follows

$$\psi_{6,1,0}^{real} \chi_{m_s} = \psi_{6,1,0} \chi_{m_s} := |p_z, m_s\rangle
\psi_{6,1,1}^{real} \chi_{m_s} = \frac{1}{\sqrt{2}} (\psi_{6,1,-1} - \psi_{6,1,1}) \chi_{m_s} := |p_x, m_s\rangle
\psi_{6,1,-1}^{real} \chi_{m_s} = \frac{i}{\sqrt{2}} (\psi_{6,1,-1} + \psi_{6,1,1}) \chi_{m_s} := |p_y, m_s\rangle$$
(2.74)



Here we define our new basis in real atomic wave functions

$$B_{TB} = \left\{ |s, \frac{1}{2}\rangle, |s, -\frac{1}{2}\rangle, |p_x, \frac{1}{2}\rangle, |p_y, \frac{1}{2}\rangle, |p_z, \frac{1}{2}\rangle, |p_x, -\frac{1}{2}\rangle, |p_y, -\frac{1}{2}\rangle, |p_z, -\frac{1}{2}\rangle \right\}$$

From equations (2.73) and (2.74), the coefficients of the corresponding eigenstates can be arranged as column vectors in a matrix. As described in Equation (2.51), this yields the inverse of the (sub-)transformation matrix

$$(t_{xyz}^{nlm})^{-1} = \begin{pmatrix} 1 & 0 & 0 & 0 & 0 & 0 & 0 & 0 \\ 0 & 1 & 0 & 0 & 0 & 0 & 0 & 0 \\ 0 & 0 & \sqrt{\frac{1}{2}} & \frac{i}{\sqrt{2}} & 0 & 0 & 0 & 0 \\ 0 & 0 & 0 & 0 & 1 & 0 & 0 & 0 \\ 0 & 0 & -\sqrt{\frac{1}{2}} & \frac{i}{\sqrt{2}} & 0 & 0 & 0 & 0 \\ 0 & 0 & 0 & 0 & \sqrt{\frac{1}{2}} & \frac{i}{\sqrt{2}} & 0 \\ 0 & 0 & 0 & 0 & 0 & 0 & 1 \\ 0 & 0 & 0 & 0 & 0 & -\sqrt{\frac{1}{2}} & \frac{i}{\sqrt{2}} & 0 \end{pmatrix} \begin{cases} |s, 0, \frac{1}{2}\rangle \\ |s, 0, -\frac{1}{2}\rangle \\ |p, -1, \frac{1}{2}\rangle \\ |p, 0, \frac{1}{2}\rangle \\ |p, 1, \frac{1}{2}\rangle \\ |p, 0, -\frac{1}{2}\rangle \\ |p, 0, -\frac{1}{2}\rangle \\ |p, 1, -\frac{1}{2}\rangle \\ |p, 1, -\frac{1}{2}\rangle \end{cases}$$

$$\text{Coefficients of } |l, m_l, m_s\rangle$$

Consequently, by inverting $(t_{xyz}^{nlm})^{-1}$ the (sub-)transformation is given as

Expanding the matrix to account for the second atom in the unit cell, we find

$$T_{xyz}^{nlm} = \begin{bmatrix} t_{xyz}^{nlm} & 0\\ 0 & t_{xyz}^{nlm} \end{bmatrix}$$
 (2.77)

Using the transformation matrix, we can convert the spin-orbit coupling matrix h_{SOC} from Equation (5.11). The explicit matrix representation of h_{SOC} in the basis of real atomic wave functions is given by

Including the second atom in the unit cell, we derive

$$H_{SOC} = \begin{bmatrix} h_{SOC} & 0\\ 0 & h_{SOC} \end{bmatrix}_{xyz} \tag{2.79}$$



2.6 Modeling and Tight-Binding Calculations

2.6.1 Infinite Bismuth Crystal (Bulk)

We are now fully equipped to perform the tight-binding calculations for the electron energy band structure of bulk bismuth. By applying the procedures outlined above to the crystal structure of bismuth, as described in Section 2.1, we construct the tight-binding matrix for the bulk crystal.

In doing so, we follow the formulations and notations provided by Liu and Allen [21]. Their model, which employs a third-neighbor tight-binding approach including spin-orbit coupling, has proven highly successful in describing the electronic properties of Bi and Sb. This model reproduces the key features near the Fermi surface that are critical for describing the small overlap between the valence and conduction bands.

The inclusion of interactions up to third neighbors is necessary for two important reasons. First, the combination of first- and second-neighbor interactions is required to properly capture the symmetries of the system, particularly the bonding between the [1, 1, 1] bilayers. Second, the distances d_1 and d_2 between neighboring atoms are very similar (see Table 2.1), making the second-neighbor interaction significant. Since only the s- and p-orbital states contribute to the valence and conduction bands, we limit the basis to these orbitals. The basis set we use to represent the matrix is given by:

$$B_{TB} = \left\{ |s^i,\uparrow\rangle, |s^i,\downarrow\rangle, |p_x^i,\uparrow\rangle, |p_y^i,\uparrow\rangle, |p_z^i,\uparrow\rangle, |p_x^i,\downarrow\rangle, |p_y^i,\downarrow\rangle, |p_z^i,\downarrow\rangle \right\}$$

Here, i = 1, 2 refers to the two atoms in the unit cell, and $m_s = \pm 1/2 \equiv \uparrow, \downarrow$ denotes the spin states. Using this set of basis vectors, we introduce four Slater-Koster parameters - $V_{ss\sigma}$, $V_{sp\sigma}$, $V_{pp\sigma}$, $V_{pp\pi}$ - for each neighbor interaction and the on-site energies E_s , E_p . Including the spin-orbit coupling parameter λ_{SOC} , this results in a total of 15 parameters. The values of the tight-binding parameters are provided in Table 2.3.



0	$\overline{}$
t an	\vdash
St	at
=	available in print a
ω.	:=
Diplomarbe	Ö
\equiv	_
20	.⊑
\sqsubseteq	a)
0	=
d	2
\Box	(0
\Box	<u>_</u>
<u></u>	>
39	Ø
<u>[6</u>	S
=	-
sion dies	hesis is
\subseteq	S
.0	Φ
S	믚
<u>a</u>	
>	. 🖳
<u></u>	믚
\sim	<u>_</u>
- 🚍	0
riginalve	
$\tilde{\Box}$	0
\circ	ersion of this th
cte (27
	Ð
0	_
\Box	R
-	
Œ	. [6
0	-≅′
te	proved original ve
ĭ	$\overline{}$
ā	(i)
· <u>=</u>	>
$\frac{1}{2}$	0
\subseteq	$\overline{}$
9	0
胺	g
Die approbierte gedruc	he a
<u>.</u>	=
	È
\mathbf{Y}	
4	
<u> </u>	
_	Ф
\mathbf{T}	2
T	e)
) 용
•	فِ
	. >

	E_s	E_p	$\lambda_{ ext{SOC}}$	
On-site energies	-10.906	-0.486	1.5	
Hopping parameters	$V_{ss\sigma}$	$V_{sp\sigma}$	$V_{pp\sigma}$	$V_{pp\pi}$
1^{st}	-0.608	1.320	1.854	-0.600
2^{nd}	-0.384	0.433	1.396	-0.344
3^{rd}	0	0	0.156	0

Table 2.3: Tight-binding parameters in [eV] for Bi. From Ref. [21]

Using the primitive vectors \mathbf{a}_1 , \mathbf{a}_2 , \mathbf{a}_3 and the displacement vector \mathbf{d}_1 from Section 2.1, we can now construct the total 16×16 Hamiltonian matrix

$$H = H_{\rm TB} + H_{\rm SOC} = \begin{bmatrix} H_{AA} & H_{AB} \\ H_{BA} & H_{BB} \end{bmatrix}$$
 (2.80)

with $H_{AA} = H_{BB}$ and $H_{AB} = H_{BA}^{\dagger}$. The matrix H_{AB} includes all contributions from the first and second neighbors of the central atom, while H_{AA} encompasses contributions from the third neighbors, along with the eigenenergies ε_i and spinorbit coupling. This can be formulated as follows

$$H_{AA} = \sum_{i}^{\text{3rd NN}} h_{AA}^{i} + \delta_{ij}\varepsilon_{j} + h_{SOC}$$

$$H_{AB} = \sum_{i}^{\text{1st NN}} h_{AB-1}^{i} + \sum_{i}^{\text{2nd NN}} h_{AB-2}^{i}$$

$$\vdots = H_{AB-1}$$

$$\vdots = H_{AB-2}$$

$$(2.81)$$

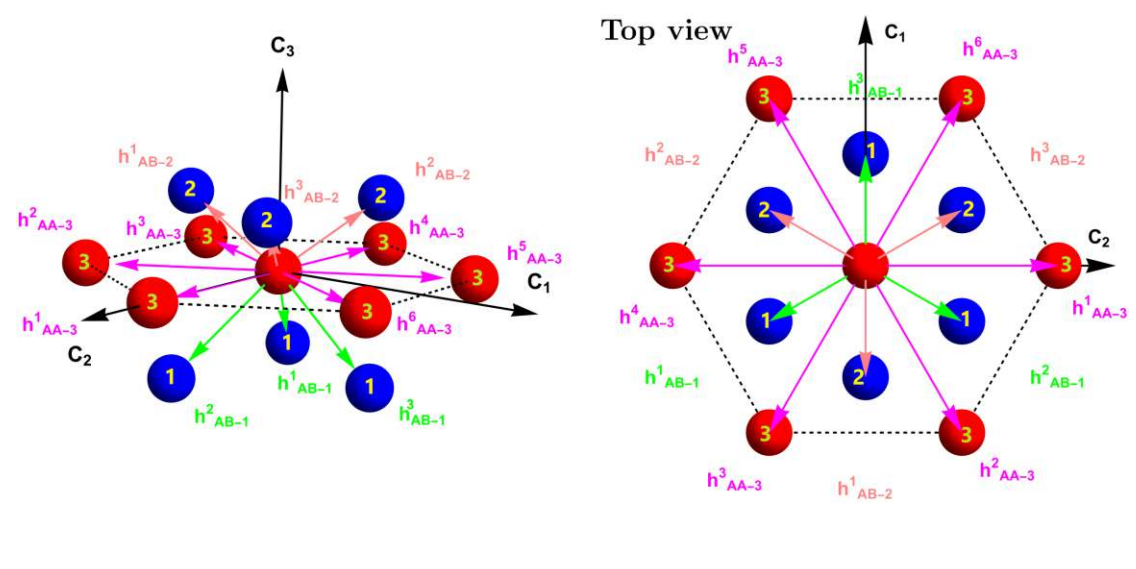


Figure 2.8: Left: Schematic representation of the interactions in bulk Bi. Right: Same as left but from the top view.

Figure 2.8 depicts a schematic representation of all the interactions in the bulk crystal. The explicit elements of the 8×8 matrices H_{AA} and H_{AB} can be found in the Appendix 5.4. By determining the factors introduced in the Appendix for each $\mathbf{k} = (k_x, k_y, k_z)$ and diagonalizing the matrix H, the electronic band structure of a Bi single crystal can be calculated.

As explained in Section 2.4, this Hamiltonian does not account for surface effects, as it is based on an infinite crystal model. Consequently, no spin-split bands are observed due to the absence of inversion-symmetry breaking. To address this, a symmetry-breaking term must be added to the total Hamiltonian to reveal spinsplit Bloch bands.



2.6.2 Thin Bismuth Film

To analyze the surface effects of a thin bismuth film, we exploit the bilayered structure of its crystal. This structure arises due to the arrangement of Bi atoms, where the first-neighbor distance along the \hat{z} -direction (1.59 Å) is smaller than the second-neighbor distance (2.39 Å).

The Hamiltonian introduced by Liu and Allen is decomposed into three parts based on neighbor contributions [26], as illustrated in Figure 2.9. Each layer consists of a central atom and its six third-nearest neighbors.

To describe the system, the Hamiltonian can be expressed as follows:

- In-plane interaction: Each layer includes an in-plane interaction term, which appears along the diagonal of the total Hamiltonian. This term corresponds to $H_{plane} = H_{AA}$ from Liu and Allen's formulation (Section 2.6.1) and includes the spin-orbit coupling.
- Interlayer and intralayer coupling: The off-diagonal elements couple the layers within the bilayer structure. The term H_{AB} from Liu and Allen is split into:
 - 1. Intralayer interaction, $H_{intra} = H_{AB-1}$, accounting for first-neighbor contributions.
 - 2. Interlayer interaction, $H_{inter} = H_{AB-2}$, including second-neighbor contributions.

To construct the total Hamiltonian, we begin with the topmost layer and couple it to the next layer using the intralayer interaction H_{AB-1} . The subsequent layer, which forms an adjacent bilayer, is then coupled via the interlayer interaction H_{AB-2} . It is important to note that the second-neighbor interaction is defined in the positive $C_3 = \hat{z} = (111)$ direction (see Figure 2.9). To extend this interaction into the negative direction, we use its hermitian conjugate (daggered expression). By repeating this process, we construct the total Hamiltonian layer by layer.

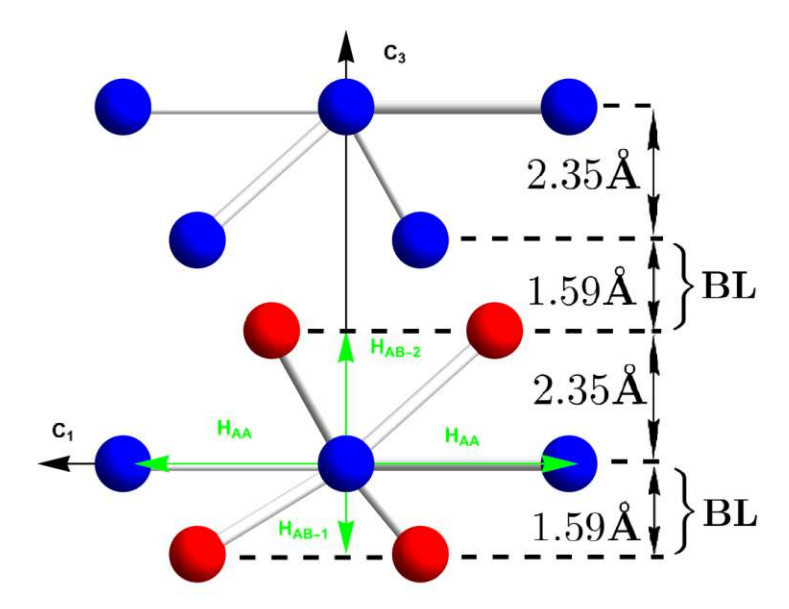


Figure 2.9: Schematic representation of the bilayer (BL) structure of bismuth along the (111) direction, highlighting the interactions within this arrangement. The central atom (at origin) forms parallel planes with its six third-nearest neighbors (blue). The bilayer structure arises from the differing distances to its neighbors. The first-neighbor atoms are closer and contribute to forming the bilayer. The second-neighbor atoms are located in the adjacent bilayer. The interactions within this structure are represented by green lines: H_{AA} corresponds to in-plane interactions, H_{AB-1} describes intra-layer interactions, and H_{AB-2} accounts for inter-layer interactions. Note that H_{AB-2} acts in the positive $\hat{z} = (111)$ - direction.

The total Hamiltonian for a thin film containing N bilayers is represented as a $16N \times 16N$ matrix:

$$H = \begin{bmatrix} H_{AA} & H_{AB-1} \\ H_{AB-1}^{\dagger} & H_{AA} & H_{AB-2}^{\dagger} \\ & H_{AB-2} & H_{AA} & H_{AB-1} \\ & & \ddots & \ddots & \ddots \\ & & & H_{AB-2} & H_{AA} & H_{AB-1} \\ & & & & & H_{AB-1} & H_{AA} \end{bmatrix}$$

$$(2.82)$$

where H_{AA} represents the in-plane interaction, and H_{AB-1} and H_{AB-2} describe the intralayer and interlayer couplings, respectively. The Hamiltonian is now a function of $\mathbf{k} = (k_x, k_y)$, as the loss of translational symmetry in the \hat{z} -direction modifies the k-space description accordingly.

2.6.3 The Bychkov-Rashba Effect and its Tight-Binding **Formulation**

The Bychkov-Rashba model [5] qualitatively explains the lifting of spin degeneracy in a two-dimensional (2D) electron gas caused by a perpendicular electric field. The effect arises when an electric field, typically caused by structural asymmetry, such as surfaces or interfaces, interacts with an electron's spin via spin-orbit coupling.

Building on the work of Petersen and Hedegård [25], Ast and Gierz [2] derived an sp-tight-binding formulation for the Bychkov-Rashba effect in two-dimensional systems. In this context, surface atoms experience a potential gradient ξ along the \hat{z} -direction. The absence of inversion symmetry ensures the electric field interacts asymmetrically with electronic states, producing the Rashba effect.

The effect can be described by the additional Hamiltonian:

$$H_{\xi} = \xi z = H_{\xi}^{\text{onsite}} + H_{\xi}^{\text{neigh}} \tag{2.83}$$

where the contributions are divided into an on-site term, H_{ξ}^{onsite} , and a nearestneighbor term, H_{ξ}^{neigh} .

On-site Contribution of H_{ξ}

The matrix elements for the on-site Hamiltonian are given by:

$$\left[H_{\xi}^{\text{onsite}}\right]_{ij} = \langle \psi_j | \xi z | \psi_i \rangle = \xi \langle \psi_j | r \cos \theta | \psi_i \rangle \propto \langle \psi_j | r Y_1^0(\theta, \phi) | \psi_i \rangle \tag{2.84}$$

In the last step, we used the relationship $\cos \theta = \sqrt{\frac{4\pi}{3}} Y_1^0(\theta, \phi)$, which expresses the cosine function in terms of spherical harmonics. This allows the angular part of the integrals to be expressed using Gaunt coefficients [8].



The properties of the Gaunt coefficients impose the following selection rules: the matrix elements are nonzero only when $\Delta l = \pm 1$ and $\Delta m = 0$. Furthermore, orbitals with $m \neq 0$ are linear combinations of spherical harmonics (as shown in Equation (2.72)). Consequently, even for some cases where $\Delta m = 0$, certain matrix elements cancel out. With these selection rules, the only nonzero matrix element is the sp_z -element.

We define the empirical parameter γ_{sp} for the sp_z interaction as

$$\gamma_{sp} = \xi \langle s|z|p_z \rangle \equiv \xi \int d\mathbf{r} \psi_s^*(\mathbf{r}) z \psi_{p_z}(\mathbf{r}) = -a_0 \xi \frac{n^* (1 + 2n^*)}{2\sqrt{3}(Z - s)}$$
(2.85)

where n^* is the effective principal quantum number, Z is the atomic number, s is the screening charge, and $a_0 = 0.529 \,\text{Å}$ is the Bohr radius (for details see Ref. [29]). The increase with n^* can be understood by the increasing spatial extension of the wave function, so that it becomes more sensitive to the effects of the potential gradient [2].

Nearest-Neighbor Contribution of H_{ξ}

The matrix elements for the nearest-neighbor contribution are expressed as:

$$\left[H_{\xi}^{\text{neigh}}\right]_{ij} = \sum_{m}^{n.n.} e^{i\mathbf{k}\mathbf{R}_{m}} \xi \left\langle \psi_{i} | r \cos \theta | \psi_{j}(\mathbf{R}_{m}) \right\rangle$$
 (2.86)

These integrals require numerical evaluation, even for simple hydrogen-like wavefunctions. However, we can identify nonzero matrix elements and their angular dependence using directional cosines. For a true 2D system, as in bismuth layers, the tight-binding matrix for the neighboring contribution in the basis:

$$B_{TB} = \left\{ |s^i,\uparrow\rangle, |s^i,\downarrow\rangle, |p_x^i,\uparrow\rangle, |p_y^i,\uparrow\rangle, |p_z^i,\uparrow\rangle, |p_x^i,\downarrow\rangle, |p_y^i,\downarrow\rangle, |p_z^i,\downarrow\rangle \right\}$$

is given by:

where n.n. denotes the summation over next neighbors $\mathbf{R}_m = \mathbf{a}_i - \mathbf{a}_j$, with $i \neq j \in \{1,2,3\}$ that lie in the same plane as the central atom (see Section 2.1). The parameters u and v are the directional cosines of the vector \mathbf{R}_m along the \hat{x} and \hat{y} -axes, respectively.

The parameters γ_{sp1} and γ_{pp1} are defined as

$$\gamma_{sp1} = \langle \psi_s, m_s | z | \psi_{p_z}(R_x), m_s' \rangle \equiv \delta_{m_s, m_s'} \int d\mathbf{r} \psi_s^*(\mathbf{r}) z \psi_{p_z}(\mathbf{r} - \mathbf{R}_m \cdot \hat{\mathbf{e}}_x)$$

$$\gamma_{pp1} = \langle \psi_{p_x}, m_s | z | \psi_{p_z}(R_x), m_s' \rangle \equiv \delta_{m_s, m_s'} \int d\mathbf{r} \psi_{p_x}^*(\mathbf{r}) z \psi_{p_z}(\mathbf{r} - \mathbf{R}_m \cdot \hat{\mathbf{e}}_x)$$
(2.88)

where $R_x = \mathbf{R}_m \cdot \hat{\mathbf{e}}_x$ is the nearest neighbor distance in the \hat{x} direction. It should be noted that matrix elements with different (same) parity between orbitals transform even (odd) under the exchange of indices [2]

$$E_{ji}(-\mathbf{R}_m) = (-1)^{|l-l'+1|} E_{ij}(\mathbf{R}_m)$$
(2.89)



Saito et al. used this formulation of the Bychkov-Rashba Hamiltonian from Equation (2.83) and added it to the uppermost and lowermost layer Hamiltonian H_{AA} from Equation (2.82) [26].

Note that for the lowermost layer, the Bychkov-Rashba Hamiltonian undergoes a sign change due to the electric field pointing in the negative \hat{z} -direction. We derive the final Hamiltonian

$$H = \begin{bmatrix} H_{AA} + H_{\xi} & H_{AB-1} \\ H_{AB-1}^{\dagger} & H_{AA} & H_{AB-2}^{\dagger} \\ & H_{AB-2} & H_{AA} & H_{AB-1} \\ & & H_{AB-1}^{\dagger} & H_{AA} & H_{AB-2}^{\dagger} \\ & & \ddots & \ddots & \ddots \\ & & & & H_{AB-2} & H_{AA} & H_{AB-1} \\ & & & & & & H_{AB-1}^{\dagger} & H_{AA} - H_{\xi} \end{bmatrix}$$

$$(2.90)$$

Saito et al. used solely the nearest-neighbor contributions while disregarding the on-site contributions, successfully reproducing the surface band dispersion [26]. Their study utilized the empirical parameters $\gamma_{sp1}=0.45\,\mathrm{eV}$ and $\gamma_{pp1}=-0.27\,\mathrm{eV}$.

2.7 Topological Matter

The following sections are closely based on the lecture notes "Introduction to Quantum Mesoscopic Transport and Topological Matter" by Prof. Mark Oliver Goerbig [10], which were kindly provided to the author. His lecture notes offer an excellent introduction to the topic of topological matter.

So far we have reviewed the fundamental aspects of the band structure formed by electrons in a periodic lattice, as determined by the underlying atomic crystal. Bloch's theorem in the context of the tight-binding formalism provides a framework for deriving its spectrum, which consists of energy bands. These energy bands can be interpreted as the energy levels of the tight-binding Hamiltonian, varying continuously with the wave vector **k**. The wave vector serves as a good quantum number due to the lattice's discrete translational symmetry.

In addition to the valuable information typically associated with band structure, Bloch bands also encode a distinct type of insight of geometric and topological nature. This insight becomes particularly relevant when we focus on a single band and vary the electron's eigenstate adiabatically, ensuring no transitions occur between bands. Despite this restriction, other bands remain present and interact with the chosen band through a coupling described by the Berry curvature.

The Berry curvature, derived from the geometric phase acquired by the electron's wave function during adiabatic evolution, reveals profound topological properties. A key quantity it provides is the Chern number, a topological invariant crucial for understanding the phenomenon of topological matter.

In the following sections, we will develop the foundational concepts needed to describe phase transitions from a topological perspective. These ideas will be applied to relativistic electrons, known as massive Dirac fermions, which offer a natural framework for qualitatively describing topological insulators.





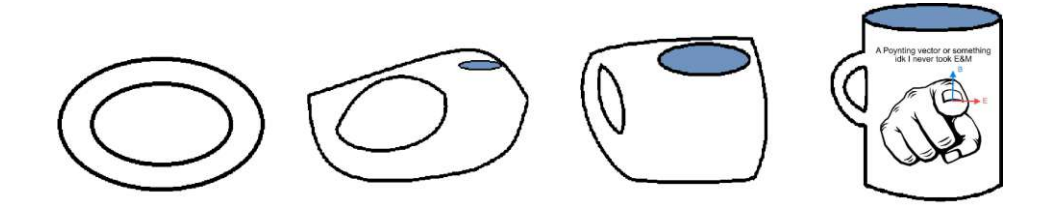


Figure 2.10: Illustration of the continuous deformation of a coffee mug into a doughnut

A natural question that arises in the context of topology in condensed matter is: where does topology play a role in phase transitions? In mathematics, a wellknown example often used to illustrate topology is the equivalence of a doughnut and a coffee mug. Mathematically, it is possible to continuously deform a doughnut into the shape of a coffee mug without making any cuts, as illustrated in Figure 2.10. Both objects share a key characteristic: the number of holes. This property is preserved during the deformation process, making it a topological invariant a quantity that remains unchanged (topologically protected) under continuous transformations. Importantly, this invariant is an integer, as partial holes are not possible.

In physics, phase transitions are often described using an order parameter. For example, the phase transition in ferromagnets can be characterized by the total magnetization $\mathbf{M}(\mathbf{r})$. Below a critical temperature T_c , microscopic magnetic moments align in such a way that the isotropy of the macroscopic magnetization is broken, resulting in a net magnetization $\mathbf{M}(\mathbf{r}) = \mathbf{M}_0$. However, this order parameter provides only a global description of the system. Locally, within small regions of the system, deviations from the order parameter can occur.

Now, consider a simple 2D ferromagnet with a magnetic monopole at position r. To describe this defect, we place a Gaussian surface around the monopole. In 2D, this surface is a closed curve (loop) that encloses the defect. We map each vector describing the evolution along the closed loop S^1 to a corresponding vector of the magnetization $\mathbf{M}(\mathbf{r})$. The magnetization vector, in turn, resides on another closed curve S_M^1 (a unit circle representing the direction of the magnetization).

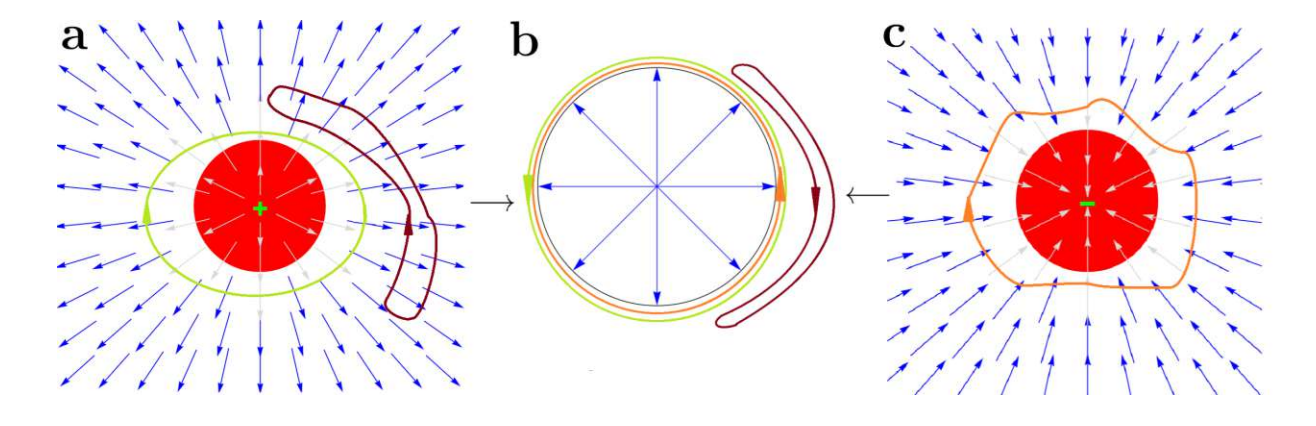


Figure 2.11: Illustration of the mapping from the space $S^1 \to S_M^1$: In (a), the green loop encloses the defect, represented by a vortex, which is characterized by a non-zero winding in (b). The brown loop in (a), on the other hand, can be continuously shrunk to a point in (b), indicating zero winding. Meanwhile, the orange loop in (c) represents an anti-vortex in (b), characterized by winding in the opposite direction.

Mathematically, we map one compact space (postion of r) to another compact space (magnetization M)

$$\mathbf{M}: S_r^1 \to S_M^1 \tag{2.91}$$

This mapping is also classified by an topological invariant integer $\pi_1(S_r^1) = \mathbb{Z}$. We can analyse this mapping by the illustration in Figure 2.11. The brown loop in 2.11(a) doesn't enclose the defect. In the picture of the magnetization in 2.11(b) the path doesn't explore the unit circle and thus can be contracted to a single point, which results in zero windings around the circle. The green path however fully encloses the defect, which in the image of the circle S_M^1 equals a closed path in a counter-clockwise direction. We can thus assign the integer +1, a so-called vortex, to the loop. Analogously the loop from 2.11(c) encloses a anti-vortex with the invariant -1. Notice that there are vortices larger/smaller than ± 1 . In this case the topological defect covers the circle S_M^1 several times. The number of windings corresponds exactly to the topological invariant $\pi_1(S_r^1) = \mathbb{Z}$, analogous to counting the number of holes in the doughnut-coffee mug analogy.

2.7.1 Berry Phase, Connection and Curvature

The starting point of the discussion is the solution of our Bloch-Hamiltonian $H(\mathbf{k})$, the Bloch-states $u_n(\mathbf{k})$ from Equation 2.15

$$\hat{H}(\mathbf{k})|u_n(\mathbf{k})\rangle = \varepsilon_n(\mathbf{k})|u_n(\mathbf{k})\rangle$$
 (2.92)

We will now show that the eigenstates $u_n(\mathbf{k})$ can be interpreted as maps from the first Brillouin zone \mathcal{K}^d - which is compact and isomorphic to a d-dimensional torus due to the periodicity of the reciprocal lattice - to the compact space of spinor states associated with the Hilbert subspace \mathcal{E}_n of the n-th band

$$|u_n(\mathbf{k})\rangle: \mathcal{K}^d \to \mathcal{E}_n$$
 (2.93)

The space of spinor states is compact as well, since Bloch states are inherently periodic. We are particularly interested in the evolution of the states $u_n(\mathbf{k})$ along closed paths. Displacing the state by a small increment $d\mathbf{k}$ yields

$$|u_n(\mathbf{k} + d\mathbf{k})\rangle = |u_n(\mathbf{k})\rangle + \nabla_{\mathbf{k}}|u_n(\mathbf{k})\rangle \cdot d\mathbf{k} \equiv |u_n(\mathbf{k})\rangle + |\nabla_{\mathbf{k}}u_n\rangle \cdot d\mathbf{k}$$
 (2.94)

We consider the adiabatic evolution of an electron along a closed path $\mathcal C$ in reciprocal space. This implies that the electron traverses the path over a sufficiently long time T, ensuring that no transitions occur between the energy band of interest and adjacent energy bands. The total evolution time T must satisfy:

$$T \gg \frac{\min[\varepsilon_i(\mathbf{k}) - \varepsilon_j(\mathbf{k})]}{\hbar}$$
 (2.95)

If the initial state at t=0 is located at $\mathbf{k_0}$, then the wave function is given by

$$|\psi(t=0)\rangle = |u_n(\mathbf{k_0})\rangle \tag{2.96}$$

At any later time, the state evolves as

$$|\psi(t)\rangle = e^{i\gamma(t)}|u_n(\mathbf{k}(t))\rangle$$
 (2.97)

The time evolution of the parametrized k-path is governed by the Schrödinger equation



$$\hat{H}(\mathbf{k}(t))|\psi(t)\rangle = i\hbar \frac{d}{dt}|\psi(t)\rangle$$
 (2.98)

Expanding the right-hand side, we find

$$i\hbar \frac{d}{dt} |\psi(t)\rangle = i\hbar \left[\dot{\gamma} |u_n(\mathbf{k}(t))\rangle + \dot{\mathbf{k}} \cdot |\nabla_{\mathbf{k}} u_n(\mathbf{k}(t))\rangle \right] e^{i\gamma(t)}$$
 (2.99)

The left-hand side becomes

$$\hat{H}(\mathbf{k}(t))|\psi(t)\rangle = e^{i\gamma(t)}\varepsilon_n(\mathbf{k}(t))|u_n(\mathbf{k}(t))\rangle$$
(2.100)

Multiplying both sides by $\langle u_n(\mathbf{k}(t))|$, we obtain

$$\dot{\gamma} = i\dot{\mathbf{k}} \cdot \langle u_n(\mathbf{k}(t)) | \nabla_{\mathbf{k}} u_n(\mathbf{k}(t)) \rangle - \frac{1}{\hbar} \varepsilon_n(\mathbf{k}(t))$$
 (2.101)

Integrating this expression over the interval t = 0 to t = T, we find

$$\gamma(T) - \gamma(0) = \int_0^T dt \, \dot{\mathbf{k}} \cdot i \langle u_n(\mathbf{k}(t)) | \nabla_{\mathbf{k}} u_n(\mathbf{k}(t)) \rangle - \frac{1}{\hbar} \int_0^T dt \, \varepsilon_n(\mathbf{k}(t))$$
 (2.102)

Using the parametrized path $\mathbf{k}(t)$, this can be rewritten as

$$\gamma(T) - \gamma(0) = \oint_C d\mathbf{k} \cdot \vec{A}_n(\mathbf{k}) - \frac{1}{\hbar} \int_0^T dt \,\varepsilon_n(\mathbf{k}(t))$$
 (2.103)

The second term represents the *dynamic phase*, which we no longer consider here. The first term represents a *qeometric phase* acquired during the evolution along the closed path C. This geometric phase is known as the Berry phase

$$\Gamma(C) = \oint_{\mathcal{C}} d\mathbf{k} \cdot \vec{A}_n(\mathbf{k}) \tag{2.104}$$



Here, the integrand $\vec{A}_n(\mathbf{k}) = i \langle u_n(\mathbf{k}) | \nabla_{\mathbf{k}} u_n(\mathbf{k}) \rangle$, known as the Berry connection, resembles a vector potential, but in reciprocal space.

A natural question is whether there exists an analog of a "topological magnetic field" in reciprocal space, derived from the curl of the Berry connection, and what its meaning is. The answer is yes and it is known as the Berry curvature, defined

$$\vec{B}_n(\mathbf{k}) = \nabla_{\mathbf{k}} \times \vec{A}_n(\mathbf{k}) = i \langle \nabla_{\mathbf{k}} u_n | \times | \nabla_{\mathbf{k}} u_n \rangle$$
 (2.105)

2.7.2 Chern Number

The Berry curvature enables the definition of a topological invariant. Drawing a parallel to electromagnetism, we can compute the magnetic flux through the first Brillouin zone, called the Berry flux

$$\Phi(\mathcal{C}) = \oint_{\mathcal{C}} d\mathbf{k} \cdot \vec{A}_n(\mathbf{k}) = \int_{\mathcal{K}} d^2k \, \vec{B}_n(\mathbf{k})$$
 (2.106)

where \mathcal{C} is a curve enclosing the first Brillouin zone \mathcal{K} . Using Stokes' theorem, we transform the line integral to a surface integral. This transformation is valid if a global gauge for the Berry connection can be defined. However, in non-trivial cases, such a global gauge cannot be found. Singularities in the Berry connection, analogous to magnetic monopoles, result in quantized flux through a closed surface around the monopole

$$\Phi(\mathcal{C}) = 2\pi C_n \tag{2.107}$$

where $C_n \in \mathbb{Z}$ is the topological invariant called the *Chern number*. The Chern number classifies topological phases and phase transitions. Since it is an integer, it cannot change continuously. In the next section, we apply this formalism to massive Dirac fermions to identify the mechanisms driving topological phase transitions and demonstrate its application to the bismuth crystal system.



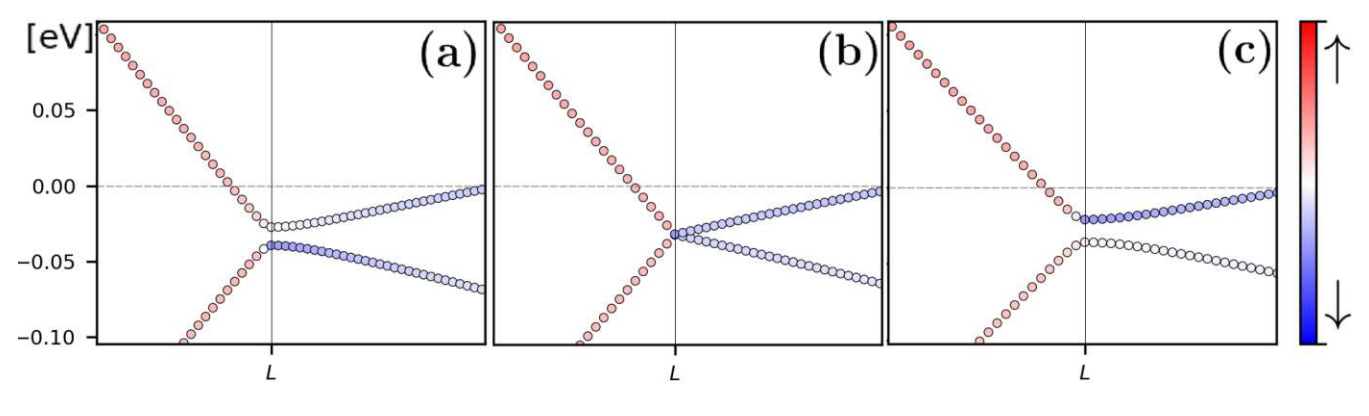


Figure 2.12: Band inversion at the L-point near the Fermi level: (a) shows the spin projection along the \hat{z} -direction for the band structure of bulk Bi, calculated using the tight-binding parameters provided by Liu and Allen [21]. By varying the parameter $V'_{ss\sigma}$ from $V'_{ss\sigma} = -0.384 \,\text{eV}$ to $V'_{ss\sigma} = -0.210 \,\text{eV}$, the gap parameter $\Delta = 0$ vanishes, as shown in (b). Further adjusting $V'_{ss\sigma}$ to $V'_{ss\sigma} = -0.150 \,\mathrm{eV}$ [24] reopens the gap, resulting in the same band gap as in (a) but with inverted bands.

2.7.3 Berry Curvature of a massive Dirac Fermion

We begin with a simple 2D two-band model, as most N-band systems can be decomposed into multiple two-band subsystems. Consider the low-energy Hamiltonian for gapped graphene with a direct band gap of 2Δ at $\mathbf{k} = 0$. In the vicinity of the band gap the two bands are described by the Hamiltonian

$$H_{\xi}(\mathbf{k}) = \hbar v(\xi k_x \sigma_x + k_y \sigma_y) + \Delta \sigma_z = \begin{pmatrix} \Delta & \xi \hbar v(k_x + i\xi k_y) \\ \xi \hbar v(k_x - i\xi k_y) & -\Delta \end{pmatrix}$$
(2.108)

where $\xi = \pm 1$ is the valley index and v is the Fermi velocity. At $\mathbf{k} = 0$, the off-diagonal terms vanish, reducing the Hamiltonian to

$$H(\mathbf{k} = 0) = \begin{pmatrix} \Delta & 0 \\ 0 & -\Delta \end{pmatrix} \tag{2.109}$$

Band Inversion

This formulation allows us to define band inversion, which occurs when the gap parameter Δ changes sign, passing through $\Delta = 0$. This value marks the topolog-



ical phase transition, as we will now demonstrate.

It is worth noting that the Hamiltonian described in Equation (2.108) is highly simplified. In practice, the gap parameter can have various sources.

Ohtsubo, Perfetti, and Görbig showed that by slightly modifying the tight-binding parameter $V'_{ss\sigma}$, the band structure for bulk Bi from Liu and Allen [21] can be reproduced. This modification results in a band inversion at the L-point [24], which is crucial to the emergence of the non-trivial topological phase in bismuth, as we will demonstrate later. The band inversion of Bi is shown in Figure 2.12 illustrating the change of the parameter $V'_{ss\sigma}$

When comparing the simplified toy-model Hamiltonian in Equation (2.108) with the Hamiltonian shown in Table 5.1, it becomes evident that $V'_{ss\sigma}$ also appears on the main diagonal. However, it is not the sole contribution to this matrix element, $V_{ss\sigma}$ also contributes to the matrix element driving the band inversion.

The Hamiltonian from Equation (2.108) can be rewritten as

$$H_{\xi}(\mathbf{k}) = \varepsilon(k) \begin{pmatrix} \cos \theta & \xi \sin \theta e^{-i\xi\phi} \\ \xi \sin \theta e^{i\xi\phi} & -\cos \theta \end{pmatrix}$$
 (2.110)

where $\varepsilon(k) = \sqrt{\Delta^2 + \hbar^2 v^2 k^2}$, $k = |\mathbf{k}|$, and

$$\cos \theta = \frac{\Delta}{\varepsilon(k)}, \quad \sin \theta = \frac{\hbar v k}{\varepsilon(k)}, \quad \tan \phi = \frac{k_y}{k_x}$$
 (2.111)

From the Hamiltonian's eigenstates

$$\left| u_{\lambda=+}^{\xi} \right\rangle = \begin{pmatrix} \cos\frac{\theta}{2} \\ \xi \sin\frac{\theta}{2} e^{i\xi\phi} \end{pmatrix}, \quad \left| u_{\lambda=-}^{\xi} \right\rangle = \begin{pmatrix} -\xi \sin\frac{\theta}{2} e^{-i\xi\phi} \\ \cos\frac{\theta}{2} \end{pmatrix}$$
 (2.112)

we compute the Berry connection, $\vec{A}_{\lambda,\xi}(\mathbf{k}) = i \langle u_{\lambda}^{\xi}(\mathbf{k}) | \nabla_{\mathbf{k}} u_{\lambda}^{\xi}(\mathbf{k}) \rangle$. Here $\lambda = \pm 1$ denotes the upper and lower branch of the energy band. The Berry connection reads as

$$\langle u_{+}^{\xi} | \nabla_{\mathbf{k}} u_{+}^{\xi} \rangle = i \xi \sin^{2} \left(\frac{\theta}{2} \right) \nabla_{\mathbf{k}} \phi, \qquad \langle u_{-}^{\xi} | \nabla_{\mathbf{k}} u_{-}^{\xi} \rangle = -i \xi \sin^{2} \left(\frac{\theta}{2} \right) \nabla_{\mathbf{k}} \phi$$
 (2.113)

Combining these expressions gives

$$\vec{A}_{\lambda,\xi}(\mathbf{k}) = -\xi\lambda\sin^2\left(\frac{\theta}{2}\right)\nabla_{\mathbf{k}}\phi = -\frac{\xi\lambda}{2}(1-\cos\theta)\nabla_{\mathbf{k}}\phi \tag{2.114}$$

Using the Berry connection, we calculate the Berry curvature

$$\vec{B}_{\lambda,\xi}(\mathbf{k}) = \nabla_{\mathbf{k}} \times \vec{A}_{\lambda,\xi}(\mathbf{k}) = \frac{\lambda \xi}{2} \nabla_{\mathbf{k}} \cos \theta \times \nabla_{\mathbf{k}} \phi \qquad (2.115)$$

From Equation (2.111), we compute $\nabla_{\mathbf{k}} \cos \theta$ and $\nabla_{\mathbf{k}} \phi$, leading to the Berry curvature, which has only a \hat{z} -component

$$\vec{B}_{\lambda,\xi}^{z}(\mathbf{k}) = -\frac{\lambda \xi}{2} \frac{\hbar^{2} v^{2} \Delta}{(\Delta^{2} + \hbar^{2} v^{2} k^{2})^{3/2}} = -\frac{\lambda \xi \operatorname{sgn}(\Delta)}{2} \frac{\lambda_{c}^{2}}{(1 + \lambda_{c}^{2} k^{2})^{3/2}}$$
(2.116)

where we have defined the characteristic length

$$\lambda_C = \frac{\hbar v}{|\Delta|} = \frac{\hbar}{m_D v} \tag{2.117}$$

The characteristic length has a very particular interpretation in the case of a Dirac fermion: It is the Compton length of relativistic quantum mechanics in condensed matter. The Compton wavelength is typically expressed as $\lambda = h/m_0c$, where m_0 is the electron's rest mass and c is the speed of light. A photon with this wavelength has energy $E = \frac{hc}{\lambda} = m_0 c^2$, which equals the rest energy of an electron. This implies that a photon with this wavelength possesses enough energy to create an electron-positron pair. In the context of condensed matter physics, the



speed of light c is replaced by the Fermi velocity v. Thus, the analogous Compton wavelength in condensed matter is given by $\lambda_C = \frac{h}{2m_D v}$, where m_D is the effective mass of the Dirac fermion. A photon with this wavelength has sufficient energy to promote an electron to the conduction band, leaving behind a hole in the valence band. Continuing to calculate the Berry flux to obtain the Chern number we find

$$\Gamma(k) = \int_{|k'| \le k} d^2 k' \vec{B}_{\lambda,\xi}(k) = -\frac{\lambda \xi \operatorname{sgn}(\Delta)}{2} 2\pi \lambda_C^2 \int_0^k dk' k' \frac{1}{(1 + \lambda_C^2 k'^2)^{3/2}}$$

$$= -\lambda \xi \operatorname{sgn}(\Delta) \pi \left(1 - \frac{1}{\sqrt{1 + \lambda_C^2 k^2}} \right)$$
(2.118)

We compute the Berry flux along a circular path of radius k, and the total flux is obtained by taking the limit as $k \to \infty$, followed by dividing the resulting Berry flux by 2π

$$\tilde{C}_{\lambda,\xi} = \frac{\Gamma(k \to \infty)}{2\pi} = -\frac{1}{2}\lambda \xi \operatorname{sgn}(\Delta)$$
 (2.119)

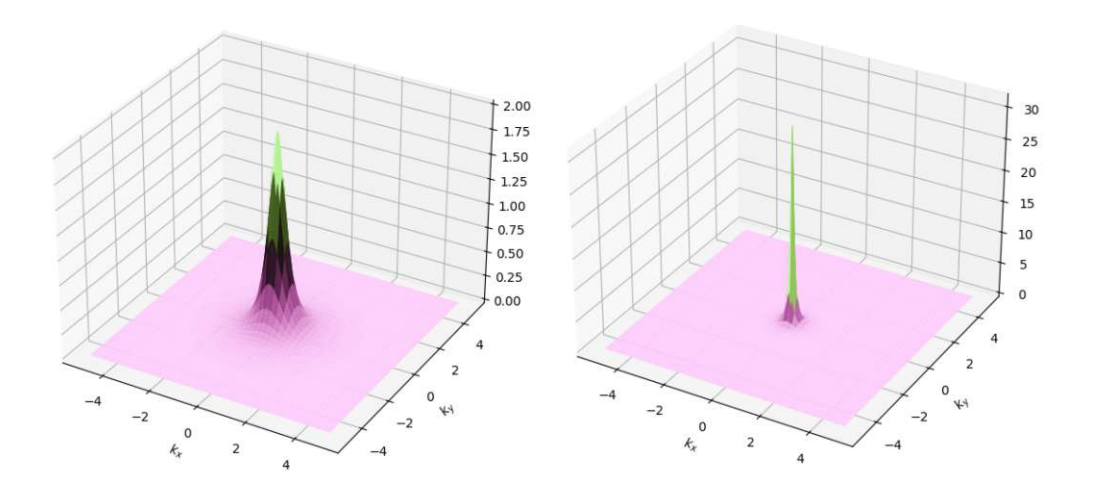


Figure 2.13: Berry flux for a massive Dirac fermion is shown for characteristic lengths $\lambda = 2a$ (left) and $\lambda = 8a$. The function is highly concentrated around $\mathbf{k} = 0$, with a characteristic spatial extent of approximately $1/\lambda$.

Here, we encounter an intriguing result that at first glance seems to contradict our earlier arguments. Specifically, we find that the total flux, \tilde{C} , which resembles a Chern number, is a half-integer. This appears paradoxical since we previously argued that half-integer invariants do not exist. However, the flux is not required to be an integer in this case because it is calculated for a Dirac fermion in the continuum limit, where the first Brillouin zone is replaced by the non-compact space \mathbb{R}^2 .

This calculation remains valid since the Berry curvature is localized within a region of size $1/\lambda \ll 1/a$, where a is the characteristic lattice constant in reciprocal space, as illustrated in Figure 2.13. Importantly, a Dirac fermion contributes $\pm 1/2$ to the Chern number. Since the Chern number must be an integer when calculated over the entire first Brillouin zone, this implies that Dirac fermions must always occur in pairs within periodic band structures.

The Chern number of a band is determined by summing the half-integer contributions from all valleys ξ , as given by

$$C_{\lambda} = \sum_{\xi} \tilde{C}_{\lambda,\xi} = -\frac{\lambda}{2} \sum_{\xi} \xi \operatorname{sgn}(\Delta_{\xi})$$
 (2.120)

This expression clearly shows that for a non-zero Chern number and consequently a non-trivial phase, the gap parameter Δ_{ξ} must change sign between different valleys ξ .



2.7.4 Topological Phase Transition in Terms of a half Chern Number

We can now articulate what is meant when referring to different topological phases. Two topological phases are considered distinct if their Chern numbers differ. Since the Chern number is an integer, it cannot change continuously during a transition between two different topological phases. We have observed that the Chern number can be modified by altering the half-Chern numbers associated with a Dirac fermion. Specifically, this occurs when the gap parameter for one valley, denoted ξ , changes sign, while the gap parameter for the opposite valley, $-\xi$, remains unchanged. This leads to a difference of $\Delta C_{\lambda,\xi} = 1$.

Regions with a Chern number $C_{\lambda,\xi} = 0$ are referred to as trivial insulators, whereas regions with $C_{\lambda,\xi} \neq 0$ are known as Chern insulators. The requirement for a gap closing implies the presence of massless Dirac fermions, as the lower and upper bands must touch at a single point, leading to vanishing diagonal elements.

2.7.5 Bulk-Boundary Correspondence

We have learned about the essential role of the gap parameter in describing a topological insulator. However, our toy Hamiltonian from Equation (2.108) describes an infinite system without boundaries. If we modify the system by including a term that accounts for its finite size, we observe interesting effects at the boundary. This phenomenon is known as bulk-boundary correspondence.

The presence of a boundary allows us to modify the gap parameter, which is crucial for describing a topological phase transition, as discussed in Section 2.7.4. This approach assumes a smooth interface between a topological material and a trivial one, such as the vacuum, as illustrated in Figure 2.14.



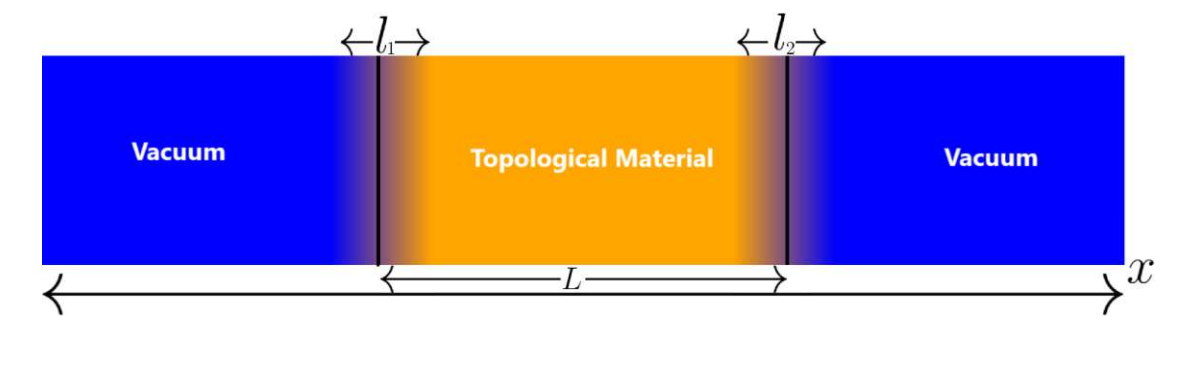


Figure 2.14: Schematic illustration of a Dirac quantum well. The interface is located at x = 0 with width l_2 . The gap parameter varies smoothly according to $\Delta(x) =$ $\Delta_0 \tanh(x/l_2)$. The second interface is located at x = -L, with width l_1 .

Initially, we consider only one interface at x=0, while also noting the second interface at x = -L for a sample of width L. For the variation of the gap parameter, simple interpolation formulas can be chosen, yielding

$$\Delta(x)_{\xi} = \begin{cases} -\Delta_0 & \text{for } x \to -\infty \\ \Delta_0 \tanh\left(\frac{x}{l_2}\right) & \text{for } x \in \left[-\frac{l_2}{2}, \frac{l_2}{2}\right] \\ \Delta_0 & \text{for } x \to \infty \end{cases}$$
 (2.121)

Now, our Hamiltonian from Equation (2.108) becomes

$$H_{\text{edge}}^{\xi} = \hbar v(\xi k_x \sigma_x + k_y \sigma_y) + \Delta(x)_{\xi} \sigma_z = \begin{pmatrix} \Delta_{\xi}(x) & \hbar v(\xi k_x - ik_y) \\ \hbar v(\xi k_x + ik_y) & -\Delta_{\xi}(x) \end{pmatrix} (2.122)$$

Due to the variation of the gap in the \hat{x} -direction and the non-commutativity $[x, k_x] = i$, the x-component of the wave vector is no longer a good quantum number. As a result, we expect a set of 1D bands in the \hat{y} -direction, each labeled by a discrete quantum number n, associated with quantization in the \hat{x} direction. To diagonalize the Hamiltonian, we need to exchange the Pauli matrices σ_z and σ_y . This can be achieved by the unitary transformation $U = \exp(i\pi\sigma_x/4)$, which rotates the spin axes by $\pi/2$ around the \hat{x} -axis.

The transformed Hamiltonian is

$$H_{\text{edge}}^{\xi'} = U H_{\text{edge}}^{\xi} U^{-1} = \begin{pmatrix} \hbar v k_y & \hbar v \xi k_x + i \Delta_{\xi}(x) \\ \hbar v \xi k_x - i \Delta_{\xi}(x) & -\hbar v k_y \end{pmatrix}$$
(2.123)

Near x = 0, we can linearize the gap parameter as $\Delta(x)_{\xi} \approx \Delta_0 x/l_2$. This gives

$$H_{\text{edge}}^{\xi'} = \begin{pmatrix} \hbar v k_y & \hbar v (\xi k_x + ix/l_S^2) \\ \hbar v (\xi k_x - ix/l_S^2) & -\hbar v k_y \end{pmatrix}$$
 (2.124)

Here, the length l_S is defined as

$$l_S = \sqrt{\frac{l_2 \hbar v}{\Delta}} = \sqrt{l_2 \lambda_C} \tag{2.125}$$

This length represents the geometric average of the interface width and the effective Compton length, as defined in Equation (2.117). The off-diagonal elements of the new Hamiltonian resemble ladder operators, like in the case for a quantum harmonic oscillator with

$$\hat{a} = \frac{l_s}{\sqrt{2}}(k_x - ix/l_S^2), \quad \hat{a}^{\dagger} = \frac{l_s}{\sqrt{2}}(k_x + ix/l_S^2)$$
 (2.126)

The Hamiltonian can be rewritten as

$$H_{\text{edge}}^{\xi=+} = \hbar v \begin{pmatrix} k_y & \sqrt{2} \frac{\hat{a}^{\dagger}}{l_S} \\ \sqrt{2} \frac{\hat{a}}{l_S} & -k_y \end{pmatrix}, \quad H_{\text{edge}}^{\xi=-} = \hbar v \begin{pmatrix} k_y & -\sqrt{2} \frac{\hat{a}}{l_S} \\ \sqrt{2} \frac{\hat{a}^{\dagger}}{l_S} & -k_y \end{pmatrix}$$
(2.127)

for $\xi = -1$. The energies of the Hamiltonian read as

$$E_{\lambda,n}^{\xi} = \begin{cases} \lambda \hbar v \sqrt{k_y^2 + 2n/l_s^2} & \text{for } n \neq 0\\ \xi \hbar v k_y & \text{for } n = 0 \end{cases}$$
 (2.128)

where n is the eigenvalue of the number operator $\hat{N} = \hat{a}^{\dagger} \hat{a}$, that is proportional to the eigenstate $|n\rangle$.

The n=0 state is the most important edge state. It is *chiral* because its group velocity in the \hat{y} -direction, which is perpendicular to the interface, is determined by the valley ξ , where the gap undergoes a sign change across the interface.

$$v_y = \frac{1}{\hbar} \frac{\partial E_{n=0}^{\xi}}{\partial k_y} = \xi v \tag{2.129}$$

This state depends solely on the intrinsic properties of the material and is independent of the specific modelling of the interface. In contrast, for states with $n \neq 0$, the width of the interface l_2 plays a significant role. The n=0 state, however, is resilient to the exact shape of the interface because it is determined only by the gap inversion in the valley ξ . Since this state necessarily crosses the energy gap at the edge, it is topologically protected. This is the concept of bulk-boundary correspondence.

The states with $n \neq 0$ are known as Volkov-Pankratov states (VP-states), named after the Soviet physicists Volkov and Pankratov. These surface states only exist if the minimum energy at $k_y = 0$ is smaller than the gap parameter Δ . Otherwise, the edge states would be "over-occupied" by bulk states, as illustrated in Figure 2.15. This requirement can be expressed through the following condition

$$\frac{\hbar v\sqrt{2n}}{l_s} < \Delta \tag{2.130}$$

With the expression from Equation (2.125) this yields

$$2n < \frac{l_2}{\lambda_C} = \frac{l_2 \Delta}{\hbar v} \tag{2.131}$$



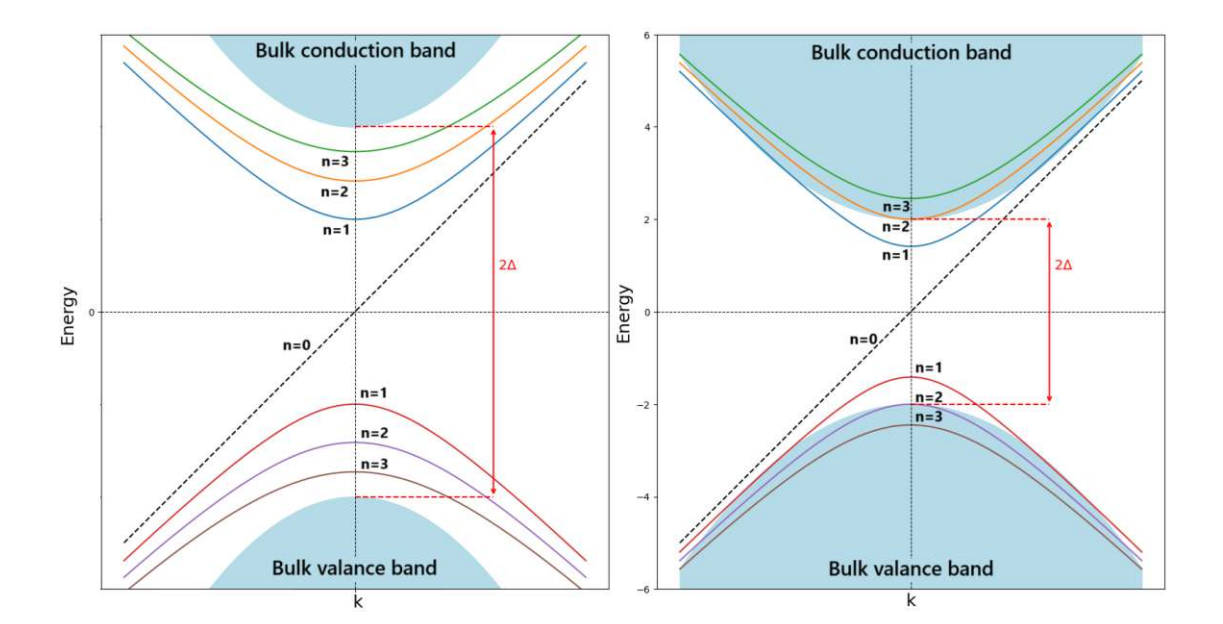


Figure 2.15: Illustration of the bulk-boundary correspondence. The chiral state n=0(black dashed line) and the massive Volkov-Pankratov states for n = 1, 2, 3 are depicted. Left: The minimum energy at $\mathbf{k} = 0$ of the Volkov-Pankratov state n = 3 is smaller than the gap parameter Δ , satisfying the condition from Equation (2.131). Therefore three VP-bands are visible. Right: The condition is not met, and states n > 1 are occupied by bulk states.

If we now consider a ribbon of width L, a second chiral state appears at the edge located at x = -L. In this case, the gap parameter varies as $\Delta(x) = -\Delta_0 \tanh(\frac{x+L}{l_1})$, and its linearization is given by $-\Delta_0 \frac{x+L}{l_1}$.

This yields the same result as in the previous case, but with a minus sign in the off-diagonal terms. Consequently, the ladder operators \hat{a} and \hat{a}^{\dagger} are exchanged. As a result, the sign of the dispersion also changes, leading to

$$E^{\xi} = -\xi \hbar v k_y \tag{2.132}$$

Helical Edge States of a Topological Insulator with Time-Reversal Symmetry

Our Hamiltonian from Equation (2.122) does not satisfy time-reversal symmetry. To enforce this symmetry, the Hamiltonian must fulfill the condition specified in Equation (2.29)

$$T^{-1}H(-\mathbf{k},\downarrow)T = H(\mathbf{k},\uparrow) \tag{2.133}$$

This is accomplished by extending the Hamiltonian to a 4×4 matrix

$$H = \begin{pmatrix} H_{\uparrow}(\mathbf{k}) & 0\\ 0 & H_{\downarrow}(\mathbf{k}) \end{pmatrix} \tag{2.134}$$

where $T^{-1}H_{\downarrow}(-\mathbf{k})T = H_{\uparrow}(\mathbf{k})$. It can be shown that the 2×2 matrices $H_s(\mathbf{k})$ must take the form

$$H_{\xi,s}(\mathbf{k}) = \hbar v(\xi s k_x \sigma_x + k_y \sigma_y) + \Delta(x)\sigma_z \tag{2.135}$$

where $s = \pm 1$ represents the spin of the Bloch state. This form ensures that the Hamiltonian respects time-reversal symmetry. If we consider spin-up electrons experiencing a gap inversion at the valley $\xi = +1$ and spin-down electrons at the valley $\xi = -1$, the interface at x = 0 is described by

$$H_{s=+}^{\text{edge}} = \hbar v \begin{pmatrix} k_y & \sqrt{2} \,\hat{a}_{l_S}^{\dagger} \\ \sqrt{2} \,\hat{a}_{l_S} & -k_y \end{pmatrix} \quad \text{and} \quad H_{s=-}^{\text{edge}} = \hbar v \begin{pmatrix} k_y & -\sqrt{2} \,\hat{a}_{l_S}^{\dagger} \\ \sqrt{2} \,\hat{a}_{l_S} & -k_y \end{pmatrix} \quad (2.136)$$

This yields the dispersion

$$E_{x=0}^{s}(\mathbf{k}) = s\hbar v k_{y}, \quad \text{for} \quad n = 0$$
(2.137)

which has a spin-dependent group velocity in the \hat{y} -direction. Note that the same arguments as in the previous case apply, where a second interface at x = -Lgenerates a second helical state with



$$E_{x=-L}^{s}(\mathbf{k}) = -s\hbar v k_{y}, \quad \text{for} \quad n = 0$$
(2.138)

In the context of time-reversal symmetric systems, an interface between a topological material and a trivial insulator (such as vacuum) creates a pair of edge states propagating in opposite directions along the edge, with their chirality locked to the electron's spin orientation. This pair of states with opposite chiralities is commonly referred to as *helical* edge states.

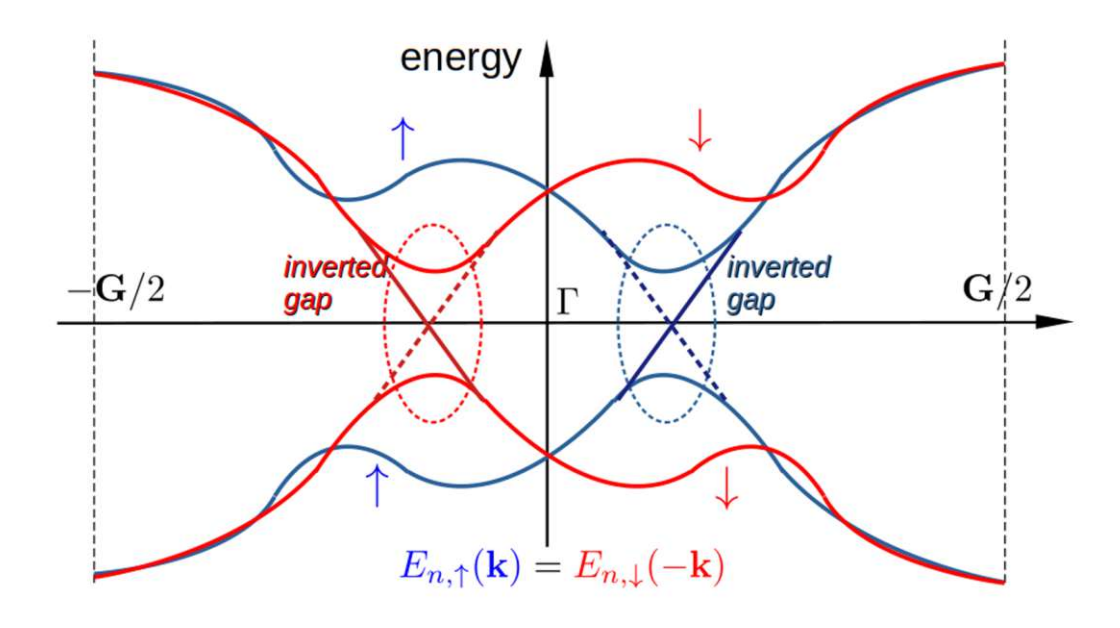


Figure 2.16: Schematic band structure of a topological insulator with time-reversal symmetry, satisfying $E_{\uparrow}(\mathbf{k}) = E_{\downarrow}(-\mathbf{k})$. There are two pairs of edge states (four in total). On the edge at x=0 (solid lines), the states exhibit opposite spin orientations and therefore possess opposite chiralities, referred to as helical edge states. At the opposite edge, x = -L (dashed lines), the chirality is inverted. From Ref. [10].

Topological Classification of Semimetals

The topological classification was originally developed for insulators, where the Fermi level always lies within a bulk gap separating the valence and conduction bands at every wave vector in the first Brillouin zone. Here, this framework is justified to a semimetal, which has overlapping energy bands yet maintains a gap at each wave vector in the first Brillouin zone. The bandstructure of a semimetal can be continuously transformed into an insulator via

$$H(\mathbf{k}) \to H'(\mathbf{k}) = H(\mathbf{k}) + \epsilon(\mathbf{k})\mathbb{I}$$
 (2.139)

where $H(\mathbf{k})$ is the matrix representation of the Bloch Hamiltonian. The energy function $\epsilon(\mathbf{k})$ shifts all energy bands in such manner that one obtains a bulk insulator. To preserve time-reversal symmetry, $\epsilon(\mathbf{k})$ must satisfy $\epsilon(\mathbf{k}) = \epsilon(-\mathbf{k})$. The function $\epsilon(\mathbf{k})$ can be interpreted as a pseudo Fermi surface, an imaginary energy surface lying between adjacent energy bands that cross the true Fermi level [24, 37]. Most importantly, adding $\epsilon(\mathbf{k})\mathbb{I}$ does not affect the eigenstates, leaving the topological invariants, such as the Chern number at time-reversal-invariant momenta (TRIMs), unchanged. Thus, semimetals can be classified topologically in the same way as insulators, provided the pseudo Fermi surface is used instead of the physical Fermi level. This construct simplifies the classification of semimetals, though in insulators, the pseudo Fermi surface coincides with the actual Fermi surface.

To illustrate this concept with respect to the surface state behavior, Figure 2.17 depicts four typical cases, corresponding to a topological insulator (a), a non-trivial semimetal (b), a trivial band insulator (c) and a topologically trivial semimetal (d). In the case of a topological insulator with time-reversal symmetry (TRS), there are necessarily surface states (solid black lines) that connect the projected bulk valence and conduction band and that cross the Fermi level (dashed black line) an odd number of times. The scenario in (a) shows three Fermi-level crossings, which can be reduced to a single crossing by continuously lowering the lower surface state (SS). The associated \mathbb{Z}_2 invariant corresponds to the parity of these crossings and remains conserved under all TRS-perturbations affecting the SS.





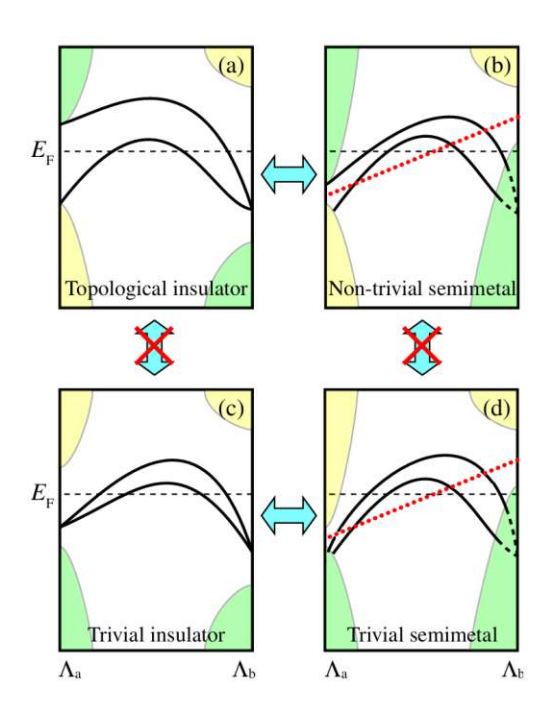


Figure 2.17: For a detailed discussion see the text. Adapted from Ref. [24].

This topological insulator (TI) is smoothly connected, via the transformation from Equation (2.139), to the semimetallic case shown in Figure 2.17(b). Here, part of the bulk conduction band (BCB) shifts below the Fermi level near the TRIM Λ_a , forming an electron pocket, while part of the bulk valence band (BVB) moves upward around Λ_b , forming a hole pocket. Since transformation does not affect the topological classification, the semimetal retains the same classification as the original TI. However, the topological invariants must now be defined relative to the pseudo Fermi surface (red dotted line in Figure 2.17(b)). The number of SS crossings with this

pseudo Fermi surface remains an odd integer, related to the \mathbb{Z}_2 invariant, ensuring a continuous SS connection between the BVB and BCB.

Similarly, a topologically trivial semimetal is one that is continuously connected to a trivial band insulator (Figure 2.17(c)). In this case, four SS crossings with the Fermi level exist, but TRS perturbations or continuous deformations can reduce them to two or zero. When defined with respect to a pseudo Fermi surface (red dotted line in Figure 2.17(d)), this even parity is preserved, though it provides no insight into crossings with the true Fermi level.

Finally, as with the insulating cases (a) and (c), there is no continuous TRS connection between the topological semimetal (b) and the trivial semimetal (d) unless band crossings between the BVB and BCB occur. This corresponds to a gap closing in the insulating case, accompanied by a band inversion at the crossing point.

Quasi 3D Topological Insulators and Surface States

Until now, we have explored the essential concepts and abstract mechanisms underlying a non-trivial two-dimensional material. With this foundation, we are equipped to study a remarkable Hamiltonian, as proposed by Zhang, Kane, and Mele [36], that describes topological matter in three dimensions. This Hamiltonian is a specialized form of the Dirac equation, which inherently describes a fermion and respects both time-reversal symmetry and the space group symmetry $R\bar{3}m$ of the bismuth's crystal structure.

Here we want to emphasize that in condensed matter physics, the components of the wave function of the Bloch Hamiltonian represent the respective weights on the underlying atomic orbitals as well as the physical spin. In contrast, the components of the three-dimensional Dirac equation - apart from the spin-1/2 description - are more abstract, lacking a direct physical interpretation and allowing a degree of arbitrariness in their definition [10].

The Hamiltonian under consideration describes a massive Dirac fermion with a mass given by $m = \Delta/v^2$ and satisfies the Clifford algebra. Its explicit form is

$$H(\mathbf{k}) = \Delta(z)\tau_z \otimes \mathbb{I} + hvk_z\tau_y \otimes \mathbb{I} + hv\tau_x \otimes (k_y\sigma_x - k_x\sigma_y)$$

$$= \begin{pmatrix} \Delta(z) & 0 & -ihvk_z & hv(k_y + ik_x) \\ 0 & \Delta(z) & hv(k_y - ik_x) & -ihvk_z \\ ihvk_z & hv(k_y + ik_x) & -\Delta(z) & 0 \\ hv(k_y - ik_x) & ihvk_z & 0 & -\Delta(z) \end{pmatrix}$$
(2.140)

Here, the Pauli matrices τ_i correspond to superpositions of atomic orbitals, while the matrices σ_i represent the electron spins, which arise due to strong spin-orbit coupling and v represents the Fermi velocity.



We will now discuss Lu and Görbig's solution [22] of this Hamiltonian for a thin film of topological matter sandwiched between two trivial insulators, such as vacuum. This setup is similar to the scenario discussed in the previous section (see Figure 2.14). For the sake of simplicity, we again begin with a single boundary located at z=0, which Lu and Görbig named the Dirac-quantum well.

Single Dirac Quantum Well

While the exact form of the gap parameter $\Delta(z)$ remains unknown, they assumed that it changes smoothly enough that it can be linearized within the interface region $z \in [-l, l]$. The description of a topological material implies that the gap parameter changes its sign across the interface.

$$\Delta(z) = \begin{cases} -\Delta_0 & \text{for } z \to -\infty \\ \Delta_0 & \text{for } z \to +\infty \end{cases}$$
 (2.141)

where $\Delta_0 > 0$ is half of the bulk gap. Again we must replace $k_z \to -i\partial_z$ because of the non-commutativity with $\Delta(z)$. To simplify the analysis, it is convenient to work in the Weyl-basis, obtained via the unitary transformation $T = \exp(i\pi\tau_y/4)$, which exchanges the roles of $\tau_x \to \tau_z$ and $\tau_z \to -\tau_x$. The transformed Hamiltonian $THT^{\dagger} |\psi\rangle = E |\psi\rangle$ is then solved for the eigenstates

$$|\psi\rangle = \begin{pmatrix} \chi_{+}(z) \\ \chi_{-}(z) \end{pmatrix} \tag{2.142}$$

which are four-component spinors that are itself an orthogonal direct sum of two two-component spinors χ_{λ} with chirality $\lambda = \pm 1$. The result is a set of two differential equations

$$(E^{2} - \hbar^{2}v^{2}k_{\parallel}^{2})\chi_{\lambda} = [\Delta(z) + \lambda\hbar v\partial_{z}][\Delta(z) - \lambda\hbar v\partial_{z}]\chi_{\lambda}$$
 (2.143)

where $k_{\parallel}^2 = k_x^2 + k_y^2$. Interestingly, this equation can be rewritten into a 1D Schrödinger-like equation

$$(E^2 - \hbar^2 v^2 k_{\parallel}^2) \chi_{\lambda} = \tilde{E}_{\lambda}^2 \chi_{\lambda} = \left(-\hbar^2 v^2 \partial_z^2 + V_{\lambda}(z)\right) \chi_{\lambda}$$
 (2.144)

with a confining potential

$$V_{\lambda}(z) = \Delta(z)^{2} + \lambda \hbar v \partial_{z} \Delta(z)$$
 (2.145)

which itself depends on the chirality λ . Note that solving for E is equivalent to solving

$$\tilde{E}_{\lambda}^2 \equiv E^2 - \hbar^2 v^2 k_{||}^2 \tag{2.146}$$

The spectrum of \tilde{E}_{λ} must be non-negative. Furthermore, the physical dimension of \tilde{E}_{λ} is that of a squared energy, making it a purely auxiliary quantity, referred to by Lu and Görbig as virtual energy.

The dispersion relation at the surface, which links virtual energies to real energies, is then given by

$$E = E_{\alpha,\lambda}(k_{\parallel}) = \alpha \sqrt{\tilde{E}_{\lambda}^2 + \hbar^2 v^2 k_{\parallel}^2}$$
 (2.147)

where $\alpha = \pm 1$ denotes the band index. So the squared Hamiltonian in the Weyl basis yields two decoupled Schrödinger equations for a quantum well with a chirality-dependent potential V_{λ} . The plane-wave motion in the $\hat{x}\hat{y}$ -direction is independent of the quantized motion in the \hat{z} -direction, reducing the 3D problem to a simpler 1D problem.

Locally, within the region $z \in [-l, l]$, where the gap parameter can be linearized as

$$\Delta(z) = \begin{cases} -\Delta_0 & \text{for } z < -l \\ \Delta_0 \frac{z}{l} & \text{for } z \in [-l, l] \\ \Delta_0 & \text{for } z > l \end{cases}$$
 (2.148)



the Hamiltonian from Equation (2.144) matches that of a 1D quantum harmonic oscillator. By substituting $\Delta_0/v^2 \to 2m$ and $v/l \to \omega/2$, we obtain

$$\frac{\tilde{E}_{\lambda}^{2}}{\Delta_{0}}\chi_{\lambda} = \left(-\frac{\hbar^{2}}{2m}\partial_{z}^{2} + \frac{1}{2}m\omega^{2}z^{2} + \lambda\frac{\hbar\omega}{2}\right)\chi_{\lambda}$$
 (2.149)

which describes the quantum harmonic oscillator with a chirality-dependent energy shift. The spectrum of this Hamiltonian is given by

$$\frac{\tilde{E}_{\lambda}^{2}}{\Delta_{0}} = \hbar \omega_{c} \left(n + \frac{1+\lambda}{2} \right) \quad \text{or} \quad \tilde{E}_{\lambda} = \sqrt{\frac{2\hbar v}{\Delta_{0} l} \left(n + \frac{1+\lambda}{2} \right)} \Delta_{0}$$
 (2.150)

where $n \geq 0$. Analyzing this result, we find that there exists exactly one zero (virtual) energy mode, $\tilde{E}_{\lambda=-1}=0$, for n=0 with chirality $\lambda=-1$. States with n>0 are the previously discussed Volkov-Pankratov states. Fermions with $\lambda=+1$ cannot be confined in the region $z \in [-l, l]$ and therefore tunnel out. This becomes clearer when considering the zero (virtual) energy solution at $k_{\parallel}=0$. In this case, known as the Jackiw-Rebbi argument [17, 28], one of the terms on the right-hand side of Equation (2.143) must vanish

$$[\Delta(z) - \lambda \hbar v \partial_z] \chi_{\lambda}^0(z) = 0$$
 (2.151)

which yields a massless Dirac fermion with real energy dispersion $E(k_{\parallel}) = \pm \hbar v k_{\parallel}$. As in the previous section, the dispersion for the massless Dirac fermion is robust against the exact shape of the interface. The ground state in the single Dirac quantum well is thus the topological massless surface state. The solution of Equation (2.151) can be obtained directly by integration, assuming the gap parameter $\Delta(z)$ is integrable

$$\chi_{\lambda}^{0}(z) \sim \exp\left[\frac{\lambda}{\hbar v} \int_{z_{0}}^{z} dz' \Delta(z')\right]$$
 (2.152)

Here, z_0 is chosen such that $\Delta(z_0) = 0$. As the solution for $\lambda = +1$ cannot be normalized, the physical surface state solution is given by $\lambda = -1$.

For the functional form of the gap parameter from Equation (2.148), the solution is given by

$$\chi_{\lambda}^{0}(z) \sim \begin{cases} e^{-z^{2}/2\xi l} & \text{for } |z| < l \\ e^{-|z|/\xi} & \text{for } |z| > l \end{cases}$$
(2.153)

This shows a crossover from a Gaussian behaviour within the region of the interface to an exponential decay outside. The intrinsic length scale

$$\xi = \frac{\hbar v}{\Delta_0} \tag{2.154}$$

characterizes the rate of exponential decay outside the Dirac quantum well. Finally, note that a more general gap function, given by a corrective term $\delta(z)$, does not alter the derived functional form of the solution as long as this term is bounded and rapidly converges to zero outside the interface, for |z| > l.

Double Dirac Quantum Well

We consider a topological insulator of width L sandwiched between two trivial insulators, where the gap function is given by

$$\Delta(z) = \begin{cases} \Delta_0 & \text{if } z < -\frac{L}{2} - l \\ -\frac{\Delta_0}{l} \left(z + \frac{L}{2} \right) & \text{if } z \in \left[-\frac{L}{2} - l, -\frac{L}{2} + l \right] \\ -\Delta_0 & \text{if } z \in \left[-\frac{L}{2} + l, \frac{L}{2} - l \right] \\ \frac{\Delta_0}{l} \left(z - \frac{L}{2} \right) & \text{if } z \in \left[\frac{L}{2} - l, \frac{L}{2} + l \right] \\ \Delta_0 & \text{if } z > \frac{L}{2} + l \end{cases}$$
(2.155)



Solving Equation (2.144) now modifies to the spectrum due to hybridization of the states caused by tunneling between the two Dirac quantum wells. In addition to the bound states of the wells, Equation (2.144) always permits plane-wave bulk solutions for energies above the bulk gap. Consequently, the hybridization of surface states involves not only direct tunneling between the bound states of the two Dirac quantum wells but also tunneling processes via bulk states at energies above the gap.

The energy spectrum of the surface states is expected to closely resemble that of a single Dirac quantum well. The deviation in energy, denoted as $\pm \Delta E_n$, can be determined using the virtual energies \tilde{E} , given by

$$\Delta E_n = \left\| |\tilde{E}| - |E_n(\mathbf{k}_{\parallel} = 0)| \right\| \tag{2.156}$$

for each chirality $\lambda = \pm 1$. The most notable consequence is the opening of a gap for the n=0 state. This state is no longer protected by the Jackiw-Rebbi argument, as the gap function now has the same sign at both limits, $z \to \pm \infty$. As a result, a zero-energy solution no longer exists and the energy shifts by $\pm \Delta E_0$, which manifests as a mass gap in the spectrum,

$$E_{\alpha,n=0}(k_{\parallel}) = \alpha \sqrt{\Delta E_0^2 + \hbar^2 v^2 k_{\parallel}^2}$$
 (2.157)

In contrast, the massive Volkov-Pankratov states experience an energy splitting of $\pm \Delta E_n$,

$$E_{\alpha,n}(\mathbf{k}_{\parallel}) = \alpha \sqrt{\left(E_n(\mathbf{k}_{\parallel} = 0) \pm \Delta E_n\right)^2 + \hbar^2 v^2 k_{\parallel}^2}$$
 (2.158)

as a result of quantum tunneling between the two Dirac quantum wells and the consequent hybridization of their states.

Results

Bulk Calculation

Using the parameters outlined in Section 2.6.1, the bulk calculation was carried out numerically. The resulting band structure for the bulk crystal is shown in Figure 3.1. Bismuth is a semi-metal, meaning it lacks a true band gap. The conduction band (CB) and valence band (VB) overlap, with the VB crossing the Fermi level near the T point and the CB at the L point. As a result, the Fermi surface comprises small electron and hole pockets, leading to a low carrier concentration of $3 \times 10^{17} \text{ cm}^{-3}$ for both charge carriers [21].

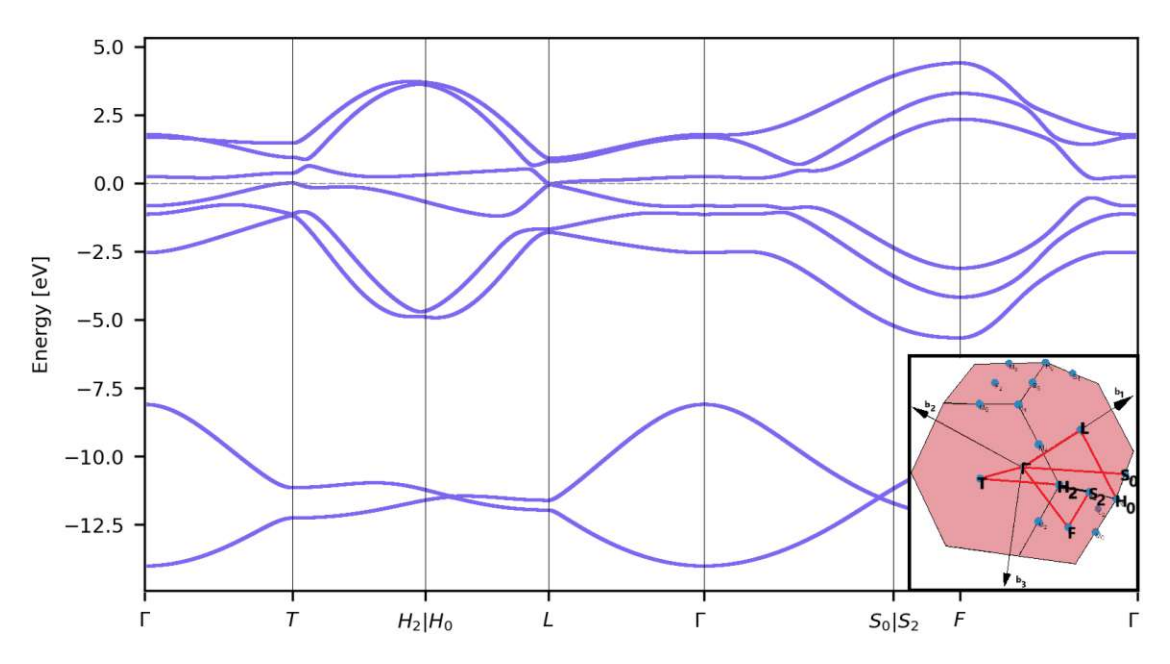


Figure 3.1: The computed band structure of bulk Bi is presented, along with the corresponding k-path in the first Brillouin zone.

The band gap at the T point is approximately 370 meV, whereas at the L point, it is around 14 meV. An inversion of the valence and conduction bands at this kpoint would alter the topological order of bismuth, as described in section 2.7.3. In other words, the symmetry (parity) of the wave functions in the highest valence band at the L point determines the \mathbb{Z}_2 topological character of Bi.

The small bulk band gap of only $2\Delta_0 = 14$ meV at the L point, which projects onto the M point of the 2D Brillouin zone, is expected to result in a very large intrinsic decay length, as described by Equations (2.117) and (2.154). The Fermi velocity was determined from the bulk band structure (see Figure 3.2) with

$$v_F = \nabla_{\mathbf{k}} E_n(\mathbf{k})|_{k_E} \tag{3.1}$$

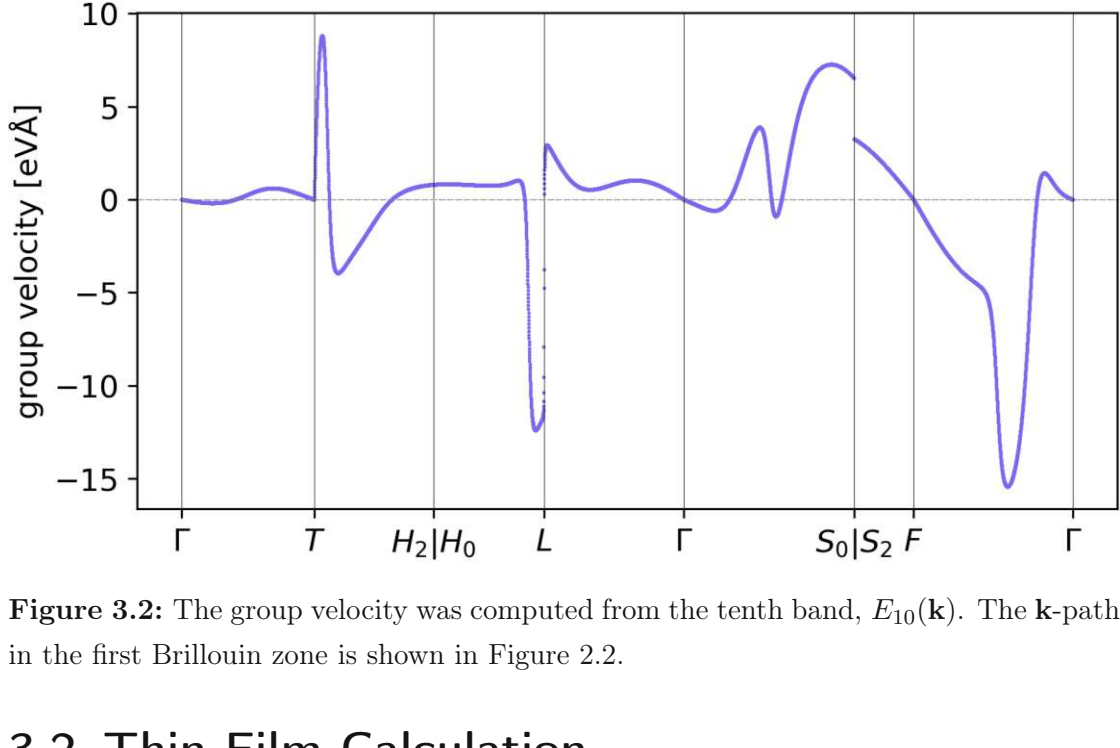
where n = 10, evaluated at the Fermi wave vector k_F near the L point. The calculated Fermi velocity is $v_F = 2.8 \,\mathrm{eV\AA}$, which leads to a decay length of

$$\xi = \frac{v_F}{\Delta_0} = \frac{2.8eV\text{Å}}{0.007eV} = 400\text{Å} \equiv 40nm$$
 (3.2)

Note that at this length, the function in Equation (2.153) decreases by a factor of $1/e \approx 0.37$, which still corresponds to a substantial tunneling probability. Only for thicknesses greater than 184 nm (468 BL) does the probability drop to 0.01. This length scale is comparable to the findings of density functional theory (DFT) calculations in Ref. [1], where the authors demonstrated that bismuth films exceeding 1000 BL can be considered bulk-like.

Due to the crystal's inversion symmetry, each band is doubly degenerate, as outlined in Section 2.4. However, at the surface, this symmetry is broken, leading to spin-polarized surface states, which is discussed in the next section. Projecting the $\Gamma - L$ path onto the (111) plane corresponds to the $\Gamma - M$ path in the two-dimensional Brillouin zone (see Figure 2.3).





Thin Film Calculation

With the Hamiltonian from Section 2.6.2, the band structure for a free standing slab of Bi(111) along the M- Γ -M direction was computed, where $k_x = 0$. Figure 3.3 presents the spin-resolved band structure for a 16-bilayer (BL) thick slab. The eigenstates of the $16N \times 16N$ Hamiltonian consist of 16N elements, where N is the number of bilayers. Each i-th block of 16 elements represents the contribution of the atomic orbitals from the i-th bilayer.

The relative contribution of the *i*-th bilayer to the band structure is determined by computing the relative opacity of each eigenvalue, proportional to the absolute square of the corresponding 16-element block (and the desired projection), normalized by the total sum over all 16N elements. Figure 3.3(a) shows the contribution from the topmost bilayer, while Figure 3.3(b) presents the contribution from the 8th bilayer. This analysis confirms that the bands crossing the Fermi energy correspond to surface states.





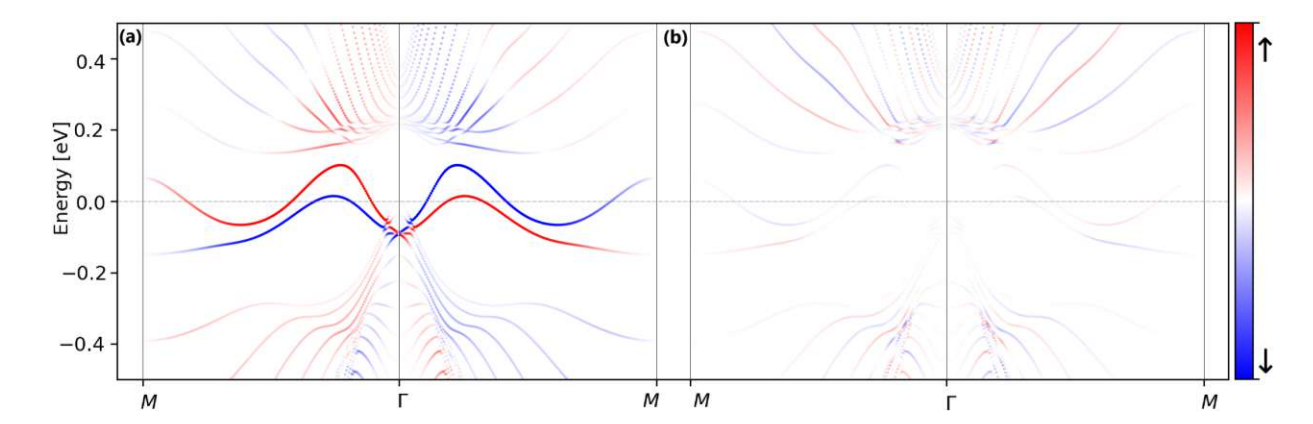


Figure 3.3: The Figure illustrates the s_x projection of the band structure for P_z orbitals in a 16-bilayer thick Bi(111) slab under a weak magnetic field applied along the \hat{z} direction. In (a), the projection is taken from the 0th (topmost) bilayer. In (b), the projection is taken from the 8th bilayer, highlighting the surface character of the two bands that cross the Fermi energy.

The surface states are double degenerated due to the system's mirror symmetry, which results from the presence of two equivalent interfaces. This results in a discontinuous spin flip in the spin projection of the band structure (see Figure 2.6). By applying a weak external magnetic field of $1 \times 10^{-4} T$ along the \hat{z} -direction, the degeneracy is lifted, causing the bands to slightly split. This enables a spinresolved analysis.

The upper branch of the surface states in Figure 3.3 forms a hexagonal electron pocket around Γ , labelled as S_1 . Additionally, six teardrop-shaped hole lobes, denoted as S_2 , and six ellipsoid-shaped electron pockets, labelled as S_3 , emerge from the lower and upper branches, respectively. This result is consistent with ARPES measurements reported in Refs. [24, 32, 4].

Setting the surface hopping parameters to $\gamma_{sp} = \gamma_{pp} = 0$ results in the disappearance of the S_2 structures, as shown in Figure 3.4.

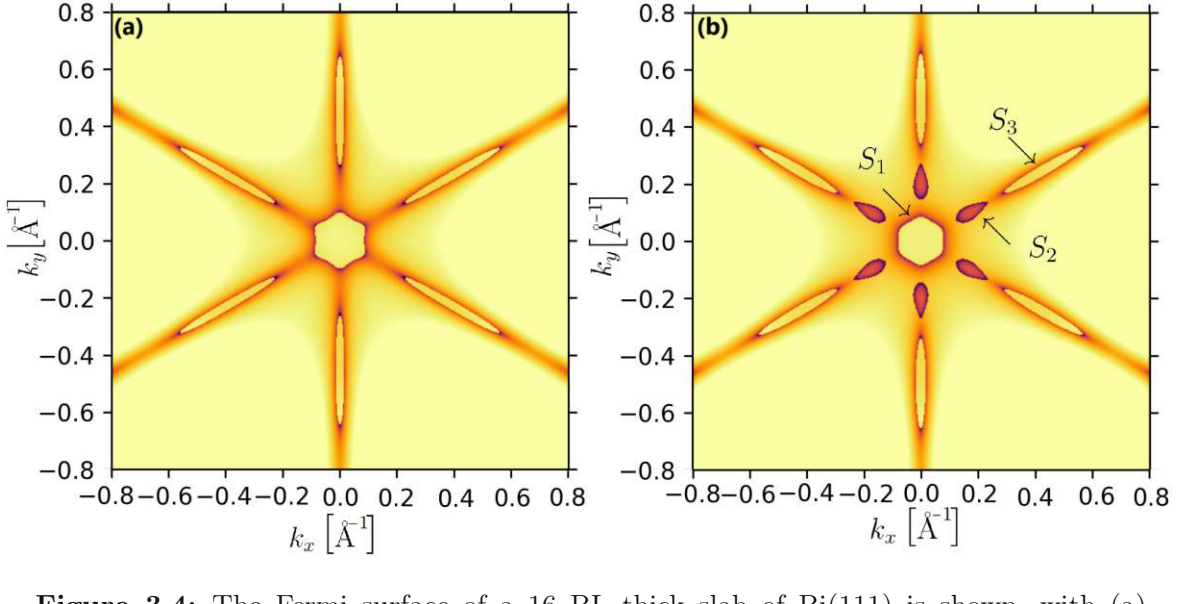


Figure 3.4: The Fermi surface of a 16 BL thick slab of Bi(111) is shown, with (a) corresponding to $\gamma_{sp} = \gamma_{pp} = 0$ and (b) to $\gamma_{sp} = -0.45$ eV and $\gamma_{pp} = 0.27$ eV. These results highlight the crucial role of surface states in shaping the Fermi surface. The coordinates of the Γ point are $\Gamma=(0,0)\,\text{Å}^{-1}$, while the M point is located at M= $(0,0.8) \text{ Å}^{-1}$.

3.2.1 Bilayer Dependence

Change in the Fermi Surface

Figure 3.5 shows a comparison of the band structures of Bi slabs with different thicknesses. The projected bulk bands were computed using the bulk Hamiltonian of Liu and Allen by iterating through all k_z values in the first Brillouin zone for each $d\mathbf{k}$ along the path from Γ to L. At each step, the maximum and minimum eigenvalues were taken to represent the valence and conduction bands, respectively.

For thicknesses below 5-6 BL, the surface state dispersion does not develop the electron pocket S_3 . Additionally, when the thickness is reduced below 4 BL, the hole pocket S_2 disappears. At 8 BL, the band structure exhibits all characteristic features S_1 , S_2 , and S_3 . For thicknesses beyond 8 BL, the sizes of S_1 and S_2 remain stable, whereas the electron pocket S_3 grows with increasing thickness and extends towards the M point. This behavior aligns with ARPES measurements reported in Refs. [14, 13, 32].



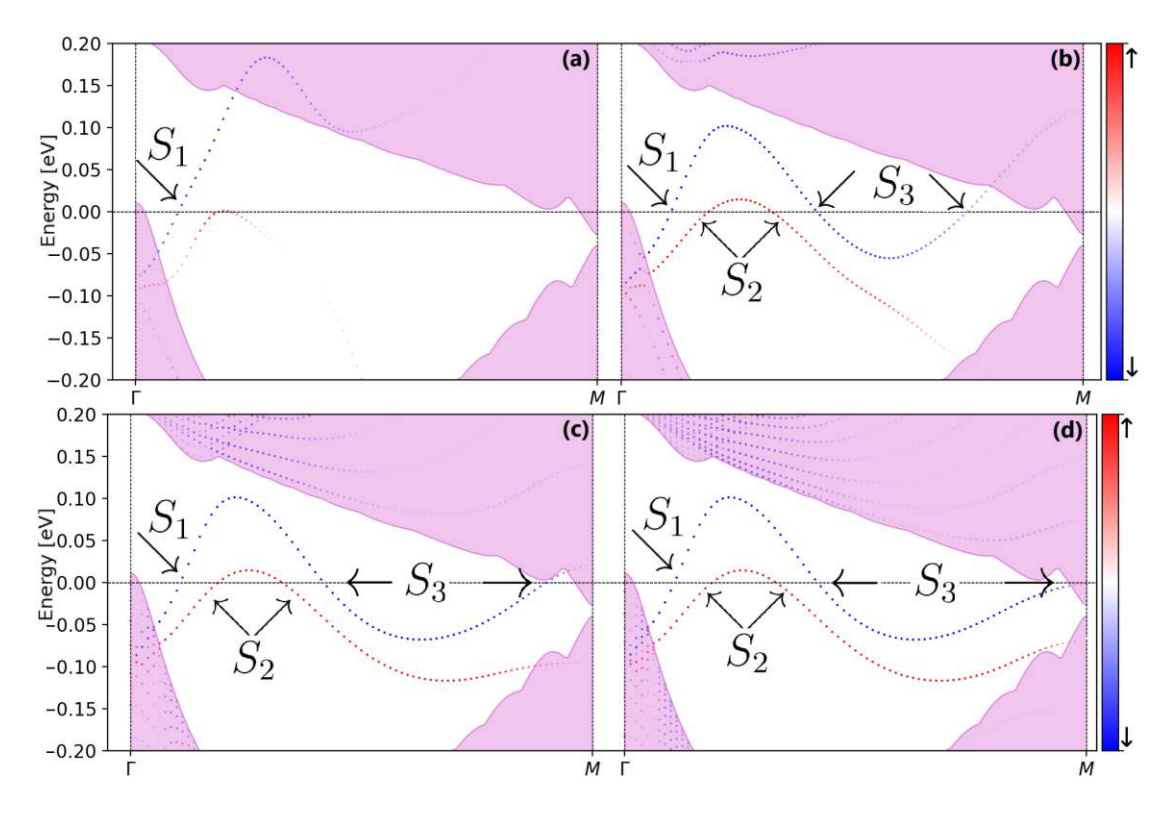


Figure 3.5: The figure shows the band structure of the s_x -projected P_z orbitals under a weak magnetic field of 1×10^{-4} T applied in the \hat{z} -direction (for spin-resolved analysis). The layer-dependent dispersion of spin-resolved surface states is presented for different thicknesses: 4 BL (a), 10 BL (b), 25 BL (c), and 50 BL (d). For thicknesses of 6 BL or less, no spin polarization is observed. Below 4 BL, the hole pocket S_2 vanishes. Beyond 8 BL, the dispersion of surface states for structures S_1 and S_2 remains unchanged, while S_3 extends further towards M with increasing thickness. At 10 BL, the surface states begin to develop a stable polarization, which diminishes towards the M point. As the thickness increases, the polarization stabilizes near M. Additionally, the other bands progressively merge with the projected bulk bands (pink area) as thickness increases.

Spin Polarization of Surface States

Figure 3.5 further shows that the surface states exhibit a spin polarization above 8 BL, which, however, decreases towards the M point. At the M point the bands are Kramer-degenerate. As the thickness increases, the polarization becomes more stable in the vicinity of the M point, which aligns with the findings of Takayama et al. [32].

In their study, scanning tunneling microscopy and electron diffraction experiments suggested that the coupling between the Bi film and the Si(111) substrate is relatively weak due to the presence of a disordered wetting layer at the interface. This implies that the Bi film behaves as a nearly free-standing layer. In this scenario, the Bi/Si interface can be considered an additional surface where surface states - referred to as Rashba states in their work - emerge, similar to those on the vacuum-side surface. These two surface states exhibit opposite spin orientations.

For sufficiently thick Bi films, the two surface states remain independent, and their wave functions do not hybridize. However, as the thickness decreases, the wave functions from the top and bottom surfaces begin to overlap and hybridize, leading to a mixing of spin states. In the thin-film limit, strong hybridization significantly reduces the observed spin polarization, explaining the general trend of polarization dependence on thickness.

However, Takayama et al. reported the absence of Kramers degeneracy at the Mpoint, along with an increased energy gap in thinner films - discussed in the next section - which indicates a strong hybridization effect.

Although the reduction in spin polarization in thin films could be attributed to the simultaneous observation of top- and bottom-surface states - given the finite photoelectron escape depth - this factor alone does not fully account for the observed behavior. In the experiment, the escape depth was approximately 20-40 Å, while the thinnest film measured around 30 Å (8 BL).

Their theoretical calculations assuming fully polarized spins predict a spin polarization of approximately 0.4–0.65, which contrasts sharply with the experimentally observed negligible spin polarization at 8 BL. This discrepancy underscores the crucial role of hybridization in the reduction of polarization. Moreover, the decrease in polarization is already noticeable at a thickness of 20 BL, suggesting that the decay length of the surface-state wave function extends to at least 20 BL.

Linear Dispersion

The electron pocket S_3 exhibits a linear dispersion perpendicular to the k_y direction along the $\Gamma-M$ path. Figure 3.6 shows a gapped Dirac-fermion-like dispersion, as discussed in Section 2.9. The gap decreases slightly as the number of bilayers increases, a trend that has been experimentally confirmed [32]. Interestingly, Takayama et al. reported that the massive Volkov-Pankratov (VP) states - being referred to as quantum well states by Takayama - remain visible even up to 40 BL.

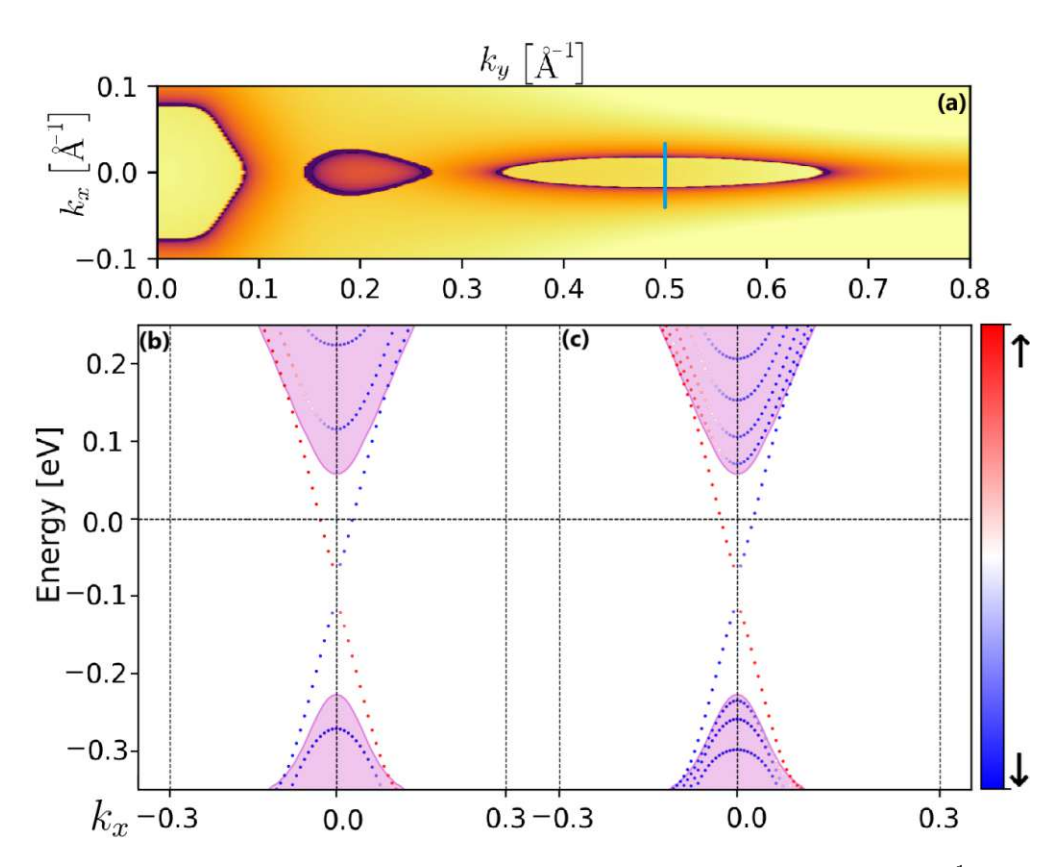


Figure 3.6: The blue line in (a) indicates the scan direction $(k_y = 0.5 \text{ Å}^{-1})$ used to obtain the dispersion shown in (b) and (c). The figure presents the s_y -projected P_z orbitals under a weak magnetic field of 1×10^{-4} T applied along the \hat{z} -direction for spinresolved analysis. Results are displayed for 20 BL in (a) and for 40 BL in (b), showing that the energy gap remains nearly unchanged. Additionally, the massive Volkov-Pankratov states are present but lie within the projected bulk bands (pink area).

Although these states lie within the projected bulk bands, they can still be observed. As the film thickness decreases, the top of the highest VP states shifts downward, while the energy separation between VP states increases.

3.2.2 Asymmetric Bychkov-Rashba Effect

So far, we have discussed the symmetric case of the Bychkov-Rashba effect, which corresponds to a free-standing bismuth slab in vacuum. However, a more realistic scenario involves a bismuth film deposited on a substrate. In this case, the potential gradient and the resulting electric field ξ are reduced compared to the free-standing case due to the presence of the substrate at one of the interfaces.

Introducing an asymmetric electric field at the two surfaces lifts the spin degeneracy of the surface bands. Previously, a weak magnetic field was required to break this degeneracy and enable a spin-resolved analysis. However, breaking the mirror symmetry between the two surfaces causes the surface bands to disperse differently.

Figure 3.7 presents the band dispersion along the $\Gamma - M$ path for different ratios of the bottom and top electric field magnitudes, $\xi_{\text{bottom}}/\xi_{\text{top}}$, while keeping the top electric field constant. While the dispersion of the surface states on the top layer remains unchanged, the surface states on the bottom layer exhibit noticeable modifications, though they reconverge towards the M point. The property of the of the spin polarization in the \hat{x} - direction remains, as before.

We first explore the effects of controlling the electric field, leaving the discussion of its implementation for later. Adjusting the electric field modifies the electronic structure of the thin film. Figure 3.8 shows the band structure for the ratio $\xi_{\text{bottom}}/\xi_{\text{top}} = \frac{2}{3}$.

As mentioned, the dispersion of the surface states in the topmost layer remains unchanged, while the surface states at the lower interface disperse in such a way that they cross at $k_y = 0.32 \text{ Å}^{-1}$. At the crossing point, a massless Dirac fermion emerges, polarized along s_y and oriented perpendicular to k_y .



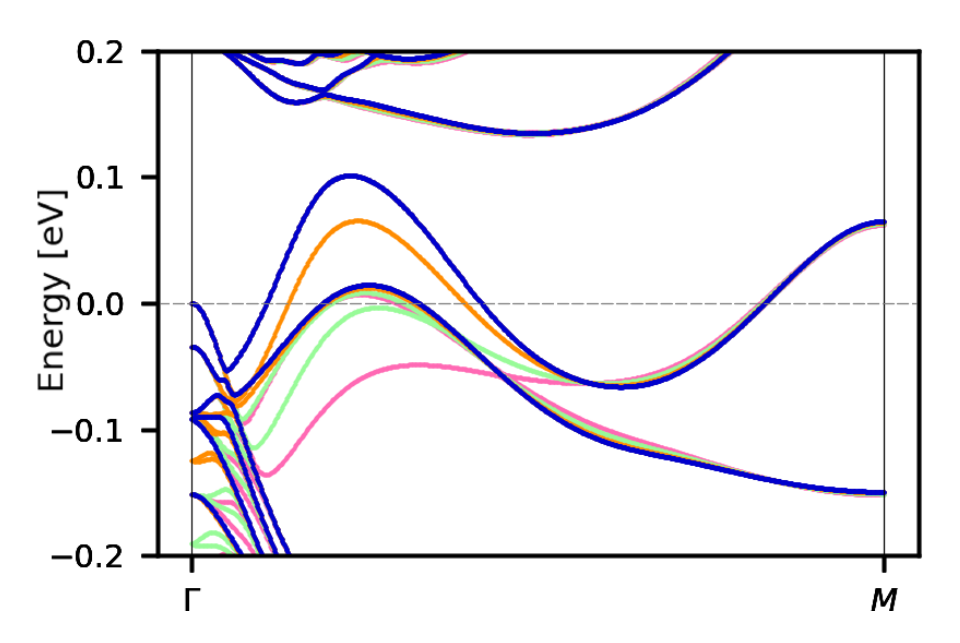
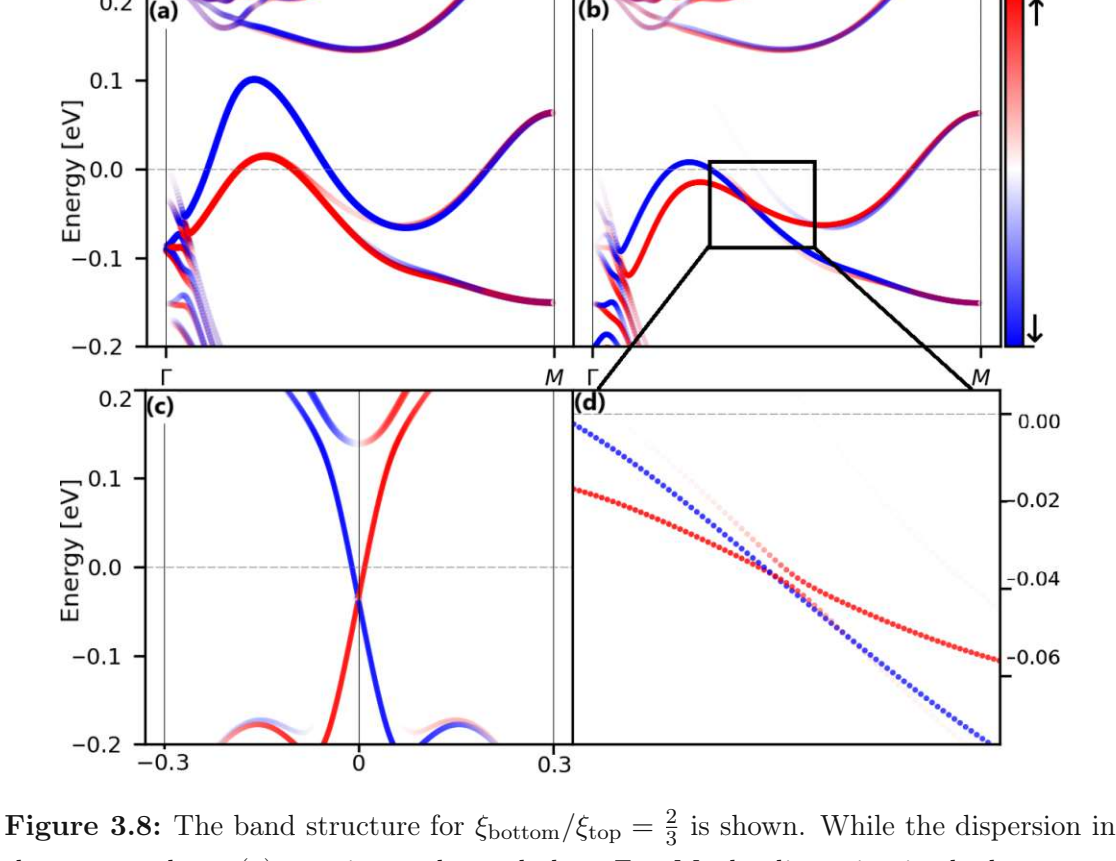


Figure 3.7: The band structure of a 16 BL thick Bi slab is shown for different ratios of the electric field $\xi_{\rm bottom}/\xi_{\rm top}$. The top electric field is kept constant, while the bottom electric field is varied with the following ratios: 1 (blue), 0.9 (orange), 0.7 (green), and 0.5 (pink; note that the top band is mostly covered by the green line). As a result, the two initially double-degenerate surface bands split into four distinct bands. Note that the dispersion of the top surface states remains unchanged and is therefore entirely covered by the blue bands.

This behavior is illustrated in (c), which shows the dispersion along $k_x = -0.3$ to 0.3 Å^{-1} .

In the vicinity of the crossing point, the spin-up polarized bands appear inverted. The contribution from the lowermost layer exhibits a discontinuous transition to another surface band near the crossing point.

Notably, the position in k-space of this Dirac point can be tuned by varying the electric field ratio. This suggests the possibility of selectively shifting the Dirac fermion toward or away from the Fermi level. For $\xi_{\text{bottom}}/\xi_{\text{top}} = 0.759$, the Dirac point shifts to the Fermi level at $k_y = 0.159 \text{ Å}^{-1}$, as shown in Figure 3.9.



the topmost layer (a) remains unchanged along $\Gamma - M$, the dispersion in the lowermost layer (b) is modified. The spin-polarized bands cross at $k_y = 0.32 \text{ Å}^{-1}$. At this crossing point, an s_y -polarized massless Dirac fermion emerges perpendicular to k_y , as shown in (c) along $k_x = -0.3$ to 0.3 Å⁻¹. (d) presents a magnified view of (b), highlighting the region around the crossing point. In this vicinity, the contribution from the lowermost layer appears to cause a band inversion.

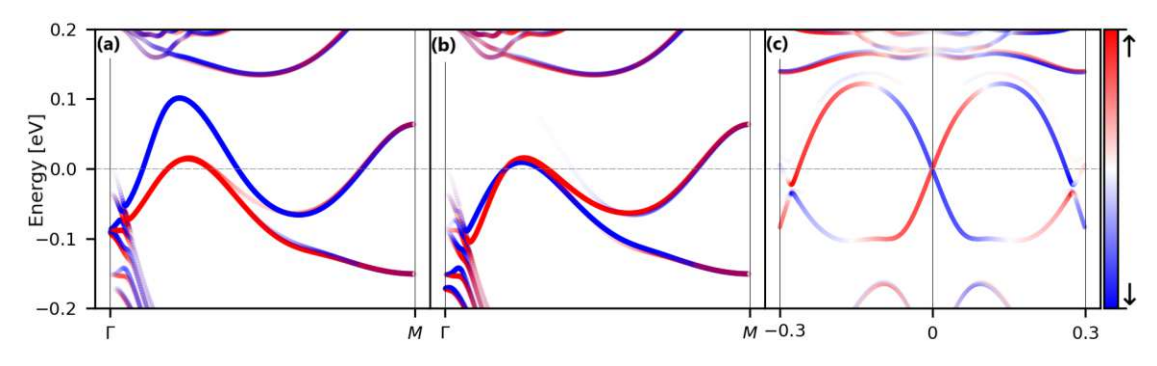


Figure 3.9: The band structure for $\xi_{\text{bottom}}/\xi_{\text{top}} = 0.759$ is shown. The dispersion at the top (a) remains unchanged. At the crossing point $k_y = 0.159 \text{ Å}^{-1}$ in (b), an s_y -polarized massless Dirac fermion emerges at the Fermi level perpendicular to k_y , as illustrated in (c) along $k_x = -0.3 \text{ to } 0.3 \text{ Å}^{-1}$.



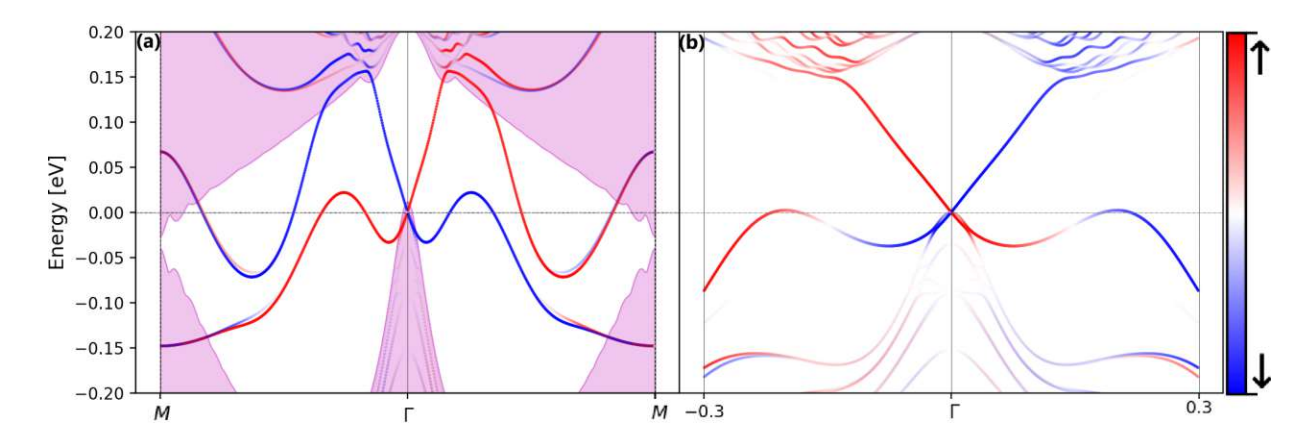


Figure 3.10: A massless Dirac fermion emerges at the Γ -point when the ratio $\xi_{\rm bottom}/\xi_{\rm top}$ is 1.31. The pink region represents the projected bulk band structure. The surface states are spin-polarized, with s_x polarization along the Γ -M path shown in (a) and s_y polarization as illustrated in (b) along $k_x = -0.3$ to 0.3 Å⁻¹.

For a larger bottom electric field, with $\xi_{\rm bottom}/\xi_{\rm top}=1.31$, the Dirac fermion residing on the bottom surface can be tuned to the Fermi level at the Γ -point, as shown in Figure 3.10. Additionally the surface state is also spin-polarized along the s_y direction along k_x .

The illustration suggests that adjusting the surface electric fields externally could induce a phase transition to a genuinely non-trivial topological semimetal. In the following section, we will discuss how these electric fields can be implemented and their effects experimentally verified.

Conclusion

In our model, the electric field is not explicitly included but implicitly affects the fitting parameters γ_{sp} and γ_{pp} (see Section 2.6.3). The electric field ξ appears in the Bychkov-Rashba Hamiltonian (Equation 2.83) and is expected to affect the matrix elements in a linear way. The electric field at a metal surface can be estimated using the material's work function and its Debye length [31]

$$E \approx \frac{\Phi}{\lambda_{\text{Deb}}} \tag{4.1}$$

For bismuth, the work function is $\Phi_{Bi} = 4.34$ eV [20] and the Debye length, as calculated by Hong et al., is $\lambda_{\text{Deb}} = 10 \text{ nm}$ [16], resulting in an intrinsic electric field of E = 0.434 eV/nm. The potential difference along the [111] direction within a single primitive unit cell (see Table 2.1) at the surface is given by $\phi =$ $(0.434\,\mathrm{eV/nm}) \times (1.17967\,\mathrm{nm}) = 0.512\,\mathrm{eV}$. This result is surprisingly close to the fitted parameters γ_{sp} and γ_{pp} reported in Ref. [26]. Hong et al. studied how an applied electric field affects a thin Bi(111) film in a metal-insulator-semiconductor (MIS) structure. With a bias voltage of V = 0.7 V, they found that 0.1 V drops across the Bi layer, corresponding to an applied electric field of E = 0.1 eV/nm. Furthermore, they showed that the Debye length showed little change with the gate voltage, remaining constant. A gate voltage of 10 V [31] would lead to an external electric field of E=0.14 eV/nm - strong enough to influence the spinpolarized bands near the Fermi level, as discussed. In theory, bismuth possesses the necessary properties for the realization of a spintronic-device. An alternative approach to constructing this device involves placing a bismuth layer between two materials with strongly different work functions. This configuration creates a non-tuneable asymmetry in the electric field.

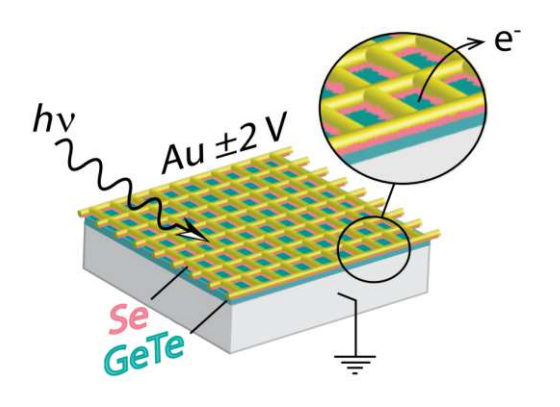


Figure 4.1: Schematic illustration of the gated sample layout used for operando SARPES measurements by Krempaský et al. Adapted from Ref. [19].

Α approach experimentally to verify this theoretical prediction operando has already been demonstrated by Krem-[19].their paský al. In achieved study, they electromanipulation ferstatic spin in roelectric α -GeTe and multifer- $Ge_{1-x}Mn_xTe$ under operando conditions. Their results confirmed that electrostatic spin Rashba semiconduccontrol in tors is possible through ferroelectric polarization reversal.

The gated sample structure used for these measurements consists of a protective Se cap covering the α -GeTe or $\text{Ge}_{1-x}\text{Mn}_x\text{Te}$ epilayers, with a Au mesh serving as the top electrode. The bottom electrode is formed by the conductive InP substrate, which is grounded via the sample holder. As shown in Figure 4.1, after in situ desorption, the Se cap adheres to the underside of the Au mesh, creating a quasi-insulating contact between the Au gate and the semiconducting α -GeTe.

An alternative approach involves predepositing an Al₂O₃ layer onto the Au mesh to enhance dielectric insulation. This modification allows for the application of higher bias voltages. The data showed that part of the applied voltage drops between the Au mesh and the GeTe film ($\approx 0.2 \text{ V}$), while the remaining voltage $(\approx 1.4 \text{ V})$ is distributed across the 200-nm-thick film.



Summary

In this work, we provided a detailed description of the calculation of bismuth's electronic structure. We examined its crystallographic structure, discussed the key symmetries involved in the calculations, and analyzed their effects.

Furthermore, we derived and solved the Hamiltonian for bulk bismuth. Building on this, we extended the model to the semi-infinite case, deriving the Hamiltonian for an N-layer bismuth slab. By analyzing the band structure, we identified spinpolarized surface states.

Through this process, we explored fundamental concepts in the theory of topological matter. Equipped with this knowledge, we were able to interpret the generated data. Assuming that bismuth is topologically non-trivial, the band structure allows for the emergence of a massless Dirac fermion, which can be shifted in k-space depending on the ratio of the electric fields at the top and bottom of the bismuth slab.

This insight suggests the possibility of a Spin-FET, a fascinating theoretical device that could serve as the foundation for spintronics.

In the Conclusion, we outlined a potential experimental approach using state-ofthe-art methods to investigate the predicted effects of an asymmetric electric field, which give rise to intriguing physical phenomena.



Appendix

Matrix Elements of the Spin-Orbit Coupling Hamiltonian

To integrate H_{SOC} into our tight-binding Hamiltonian, we will now explicitly calculate its matrix elements.

First, we address the term $\vec{\sigma} \cdot \vec{L} = \hat{L}_x \hat{\sigma}_x + \hat{L}_y \hat{\sigma}_y + \hat{L}_z \hat{\sigma}_z$ from equation (2.37). We can rewrite it using ladder operators as follows:

$$\hat{L}_{+} = \hat{L}_{x} + i\hat{L}_{y}, \qquad \hat{L}_{-} = \hat{L}_{x} - i\hat{L}_{y},
\hat{\sigma}_{+} = \hat{\sigma}_{x} + i\hat{\sigma}_{y}, \qquad \hat{\sigma}_{-} = \hat{\sigma}_{x} - i\hat{\sigma}_{y}.$$
(5.1)

These operators shift the quantum numbers m_l and m_s by ± 1 . We use a basis of complex atomic wavefunctions, which we will denote as $|n,l,m_l,s,m_s\rangle = |m_l,m_s\rangle$ for brevity, where l = 0, 1, 2, ..., n; $m_l = -l, -l + 1, ..., l$; $s = \frac{1}{2}$; and $m_s = \pm \frac{1}{2}$.

Considering the product

$$\hat{L}_{+}\hat{\sigma}_{-} + \hat{L}_{-}\hat{\sigma}_{+} = 2(\hat{L}_{x}\hat{\sigma}_{x} + \hat{L}_{y}\hat{\sigma}_{y}), \tag{5.2}$$

we nearly obtain the desired form. Adding $\hat{L}_z\hat{\sigma}_z$ gives

$$\vec{\sigma} \cdot \vec{L} = \frac{1}{2} (\hat{L}_{+} \hat{\sigma}_{-} + \hat{L}_{-} \hat{\sigma}_{+}) + \hat{L}_{z} \hat{\sigma}_{z}. \tag{5.3}$$



The eigenvalues of these operators are straightforward to calculate:

$$\hat{L}_{\pm} | n, l, m_l, s, m_s \rangle = \sqrt{l(l+1) - m_l(m_l \pm 1)} | n, l, m_l \pm 1, s, m_s \rangle,
\hat{\sigma}_{\pm} | n, l, m_l, s, m_s \rangle = \sqrt{s(s+1) - m_s(m_s \pm 1)} | n, l, m_l, s, m_s \pm 1 \rangle,$$
(5.4)

$$\hat{L}_{z} |n, l, m_{l}, s, m_{s}\rangle = m_{l} |n, l, m_{l}, s, m_{s}\rangle,$$

$$\hat{\sigma}_{z} |n, l, m_{l}, s, m_{s}\rangle = m_{s} |n, l, m_{l}, s, m_{s}\rangle.$$
(5.5)

As the Bi bands consist of 6s and 6p orbitals, we limit the basis B_{SOC} to include only these orbitals. For the 6s orbital (l = 0), all matrix elements are zero, so we $\text{limit the basis only to 6p orbitals } B^{6p}_{SOC} = \left\{ \left| -1, \tfrac{1}{2} \right\rangle, \left| 0, \tfrac{1}{2} \right\rangle, \left| 1, \tfrac{1}{2} \right\rangle, \left| -1, -\tfrac{1}{2} \right\rangle, \left| 0, -\tfrac{1}{2} \right\rangle, \left| -1, -\tfrac{1}{2} \right\rangle \right\},$ where subscripts indicate m_l values. This basis covers only one atom in the unit cell; a second atom will later extend the matrix.

Evaluating the matrix elements

$$H_{ij}^{SOC} = \langle i | \hat{H}_{SOC} | j \rangle, \tag{5.6}$$

for equation (5.3) with $i, j \in B_{SOC}$, we note that the terms in the bracket require eigenstates differing by $\Delta m_l = \pm 1$ and $\Delta m_s = \mp 1$, while $\hat{L}_z \hat{\sigma}_z$ only requires reading of the quantum numbers of the eigenstates and multiplying them. Applying these rules, we find



giving a total sub-Hamiltonian

$$h_{SOC} = \frac{\lambda_{SOC}}{2} \begin{bmatrix} -1 & 0 & 0 & 0 & \sqrt{2} & 0\\ 0 & 0 & 0 & 0 & \sqrt{2} & 0\\ 0 & 0 & 1 & 0 & 0 & 0\\ 0 & 0 & 0 & 1 & 0 & 0\\ \sqrt{2} & 0 & 0 & 0 & 0 & 0\\ 0 & \sqrt{2} & 0 & 0 & 0 & -1 \end{bmatrix}_{B_{SOC}}$$
(5.10)

Extending the basis to 6s orbitals

$$B_{SOC} = \left\{ \underbrace{|0, \frac{1}{2}\rangle, |0, -\frac{1}{2}\rangle}_{6s-orbitals}, |-1, \frac{1}{2}\rangle, |0, \frac{1}{2}\rangle, |1, \frac{1}{2}\rangle, |-1, -\frac{1}{2}\rangle, |0, -\frac{1}{2}\rangle, |-1, -\frac{1}{2}\rangle \right\}$$

we get

Considering the second atom in the unit cell, the total SOC Hamiltonian is

$$H_{SOC} = \begin{bmatrix} h_{SOC} & 0\\ 0 & h_{SOC} \end{bmatrix}_{B_{SOC}}$$

$$(5.12)$$

5.2 Matrix Elements of the Zeeman Hamiltonian

To evaluate the matrix elements of the Zeeman Hamiltonian, we begin with equation (2.48)

$$h_Z = \mu_B g_j B_z^{\text{ext}} \langle \hat{J}_z \rangle \tag{5.13}$$

as introduced in Section 2.4.3. We use the total angular momentum eigenstates $|n,l,j,m_i\rangle$ as our basis to evaluate the matrix elements, where the quantum numbers take the values $l = 0, 1, 2, ..., n; j = \frac{1}{2}, \frac{3}{2}, ...; m_j = -j, -j + 1, ..., j.$

The specific basis chosen for the calculation is:

$$B_Z = \{|s, \frac{1}{2}, \frac{1}{2}\rangle, |s, \frac{1}{2}, -\frac{1}{2}\rangle, |p, \frac{3}{2}, \frac{3}{2}\rangle, |p, \frac{3}{2}, \frac{1}{2}\rangle, |p, \frac{3}{2}, -\frac{1}{2}\rangle, |p, \frac{3}{2}, -\frac{3}{2}\rangle, |p, \frac{1}{2}, -\frac{1}{2}\rangle, |p, \frac{1}{2}, -\frac{1}{2}\rangle, |p, \frac{1}{2}, -\frac{1}{2}\rangle\}$$
 where we omit the quantum number n for brevity.

Since the matrix representation of h_Z in this basis is diagonal, we can directly assign the eigenvalues m_i to the corresponding eigenstates. However, note that the Landé factor g_j depends on the values of l and j. Specifically, for s-orbitals, $g_j = 2$, and for *p*-orbitals, $g_j = \frac{4}{3}$.

By placing the eigenvalues m_i on the diagonal and applying the appropriate Landé factors, we obtain the Zeeman Hamiltonian matrix:

Considering the second atom in the unit cell, the total Zeeman Hamiltonian is

$$H_Z = \begin{bmatrix} h_Z & 0\\ 0 & h_Z \end{bmatrix}_{B_Z} \tag{5.15}$$

5.3 Basis Change

5.3.1 Clebsch-Gordan Coefficents

For the basis of H_Z , we choose the eigenstates of the total angular momentum, represented as $|n, l, j, m_j\rangle$. For simplicity, we abbreviate these states as $|j, m\rangle$. The complete basis is given by

$$B_Z = \left\{ \left| s, \frac{1}{2}, \frac{1}{2} \right\rangle, \left| s, \frac{1}{2}, -\frac{1}{2} \right\rangle, \left| p, \frac{3}{2}, \frac{3}{2} \right\rangle, \left| p, \frac{3}{2}, \frac{1}{2} \right\rangle, \left| p, \frac{3}{2}, -\frac{1}{2} \right\rangle, \left| p, \frac{3}{2}, -\frac{3}{2} \right\rangle, \left| p, \frac{1}{2}, -\frac{1}{2} \right\rangle, \left| p, \frac{1}{2}, \frac{1}{2} \right\rangle \right\}$$

In complex atomic wave functions the electron is characterized by a well-defined orbital angular momentum l, which takes the values l=1 or l=2, and a fixed spin at $s = \frac{1}{2}$.

The eigenstates in this basis are written as $|n, l, m_l, s, m_s\rangle$, or more concisely as $|m_l, m_s\rangle$. Here, the quantum numbers m_l and m_s are in the the ranges:

$$-l \le m_l \le l, \quad -s \le m_s \le s.$$

The complete basis is given by

$$B_{SOC} = \left\{ \left| s, 0, \frac{1}{2} \right\rangle, \left| s, 0, -\frac{1}{2} \right\rangle, \left| p, -1, \frac{1}{2} \right\rangle, \left| p, 0, \frac{1}{2} \right\rangle, \left| p, 1, \frac{1}{2} \right\rangle, \left| p, -1, -\frac{1}{2} \right\rangle, \left| p, 0, -\frac{1}{2} \right\rangle, \left| p, -1, -\frac{1}{2} \right\rangle \right\}$$

Starting with the p-orbitals, we first consider the extremal state $|j = \frac{3}{2}, m = \frac{3}{2}\rangle$, which is defined by $J_{+}|j_{\rm max},m_{\rm max}\rangle=0$. In this case, $j_{\rm max}$ and $m_{\rm max}$ are given by $j_{\text{max}} = m_{\text{max}} = l + s = 1 + \frac{1}{2} = \frac{3}{2}.$

This state is uniquely given by

$$|j = \frac{3}{2}, m = \frac{3}{2}\rangle = |m_l = 1, m_s = \frac{1}{2}\rangle$$
 (5.16)

If we apply \tilde{J}_{-} to this state, we obtain on one hand:

$$\hat{J}_{-}|j = \frac{3}{2}, m = \frac{3}{2}\rangle = \sqrt{3}|j = \frac{3}{2}, m = \frac{1}{2}\rangle$$
 (5.17)

and on the other hand, using $J_{-} = L_{-} + \hat{\sigma}_{-}$

$$\hat{L}_{-} + \hat{\sigma}_{-} | m_l = 1, m_s = \frac{1}{2} \rangle = \sqrt{2} | m_l = 0, m_s = \frac{1}{2} \rangle + | m_l = 1, m_s = -\frac{1}{2} \rangle$$
 (5.18)

Thus, we have the relation:

$$|j = \frac{3}{2}, m = \frac{1}{2}\rangle = \sqrt{\frac{2}{3}}|m_l = 0, m_s = \frac{1}{2}\rangle + \sqrt{\frac{1}{3}}|m_l = 1, m_s = -\frac{1}{2}\rangle$$
 (5.19)

Upon applying the operator \hat{J}_{-} once again to this state, we acquire on one side:

$$\hat{J}_{-}|j=\frac{3}{2}, m=\frac{1}{2}\rangle = 2|j=\frac{3}{2}, m=-\frac{1}{2}\rangle$$
 (5.20)

and on the other side, using $\hat{J}_{-} = \hat{L}_{-} + \hat{\sigma}_{-}$

$$(\hat{L}_{-} + \hat{\sigma}_{-}) \left(\sqrt{\frac{2}{3}} | m_{l} = 0, m_{s} = \frac{1}{2} \rangle + \sqrt{\frac{1}{3}} | m_{l} = 1, m_{s} = -\frac{1}{2} \rangle \right)$$

$$= \sqrt{\frac{2}{3}} (\hat{L}_{-} + \hat{\sigma}_{-}) | m_{l} = 0, m_{s} = \frac{1}{2} \rangle + \sqrt{\frac{1}{3}} \hat{L}_{-} | m_{l} = 1, m_{s} = -\frac{1}{2} \rangle$$

$$= \sqrt{\frac{4}{3}} | m_{l} = -1, m_{s} = \frac{1}{2} \rangle + \sqrt{\frac{2}{3}} | m_{l} = 0, m_{s} = -\frac{1}{2} \rangle + \sqrt{\frac{2}{3}} | m_{l} = 0, m_{s} = -\frac{1}{2} \rangle$$

$$= \frac{2}{\sqrt{3}} | m_{l} = -1, m_{s} = \frac{1}{2} \rangle + 2\sqrt{\frac{2}{3}} | m_{l} = 0, m_{s} = -\frac{1}{2} \rangle$$

$$(5.21)$$

Therefore, we have relation:

$$|j = \frac{3}{2}, m = -\frac{1}{2}\rangle = \sqrt{\frac{1}{3}}|m_l = -1, m_s = \frac{1}{2}\rangle + \sqrt{\frac{2}{3}}|m_l = 0, m_s = -\frac{1}{2}\rangle$$
 (5.22)



By applying \hat{J}_{-} once more, we find on one side

$$\hat{J}_{-}|j = \frac{3}{2}, m = -\frac{1}{2}\rangle = \sqrt{3}|j = \frac{3}{2}, m = -\frac{3}{2}\rangle$$
 (5.23)

and on the other side, using $\hat{J}_{-} = \hat{L}_{-} + \hat{\sigma}_{-}$

$$(\hat{L}_{-} + \hat{\sigma}_{-}) \left(\sqrt{\frac{1}{3}} | m_{l} = -1, m_{s} = \frac{1}{2} \rangle + \sqrt{\frac{2}{3}} | m_{l} = 0, m_{s} = -\frac{1}{2} \rangle \right)$$

$$= \sqrt{\frac{1}{3}} \hat{\sigma}_{-} | m_{l} = -1, m_{s} = \frac{1}{2} \rangle + \sqrt{\frac{2}{3}} \hat{L} =_{-} | m_{l} = 0, m_{s} = -\frac{1}{2} \rangle$$

$$= \sqrt{\frac{1}{3}} | m_{l} = -1, m_{s} = -\frac{1}{2} \rangle + \sqrt{\frac{4}{3}} | m_{l} = -1, m_{s} = -\frac{1}{2} \rangle$$

$$= \sqrt{3} | m_{l} = -1, m_{s} = -\frac{1}{2} \rangle$$

$$= \sqrt{3} | m_{l} = -1, m_{s} = -\frac{1}{2} \rangle$$

$$(5.24)$$

Thus, we have

$$|j = \frac{3}{2}, m = -\frac{1}{2}\rangle = |m_l = -1, m_s = -\frac{1}{2}\rangle$$
 (5.25)

Next, we consider the states $|j = \frac{1}{2}, m\rangle$ for p-orbitals. The maximum value of m is $m = \frac{1}{2}$. Therefore, the state $|j = \frac{1}{2}, m = \frac{1}{2}\rangle$ must be a linear combination of $|m_l = 1, m_s = -\frac{1}{2}\rangle$ and $|m_l = 0, m_s = \frac{1}{2}\rangle$. We write this as

$$|j = \frac{1}{2}, m = \frac{1}{2}\rangle = \alpha |m_l = 1, m_s = -\frac{1}{2}\rangle + \beta |m_l = 0, m_s = \frac{1}{2}\rangle$$
 (5.26)

This state must be orthogonal to

$$|j = \frac{3}{2}, m = \frac{1}{2}\rangle = \sqrt{\frac{2}{3}}|m_l = 0, m_s = \frac{1}{2}\rangle + \sqrt{\frac{1}{3}}|m_l = 1, m_s = -\frac{1}{2}\rangle$$
 (5.27)

Thus:

$$0 = \langle j = \frac{3}{2}, m = \frac{1}{2} | j = \frac{1}{2}, m = \frac{1}{2} \rangle = \sqrt{\frac{1}{3}} \alpha + \sqrt{\frac{2}{3}} \beta$$
 (5.28)



This implies $\beta = -\frac{1}{\sqrt{2}}\alpha$ and with $\alpha^2 + \beta^2 = 1$, we obtain:

$$|j = \frac{1}{2}, m = \frac{1}{2}\rangle = \sqrt{\frac{2}{3}}|m_l = 1, m_s = -\frac{1}{2}\rangle - \sqrt{\frac{1}{3}}|m_l = 0, m_s = \frac{1}{2}\rangle$$
 (5.29)

Repeating the procedure by applying \hat{J}_{-} , we have on one hand:

$$\hat{J}_{-}|j=\frac{1}{2}, m=\frac{1}{2}\rangle = |j=\frac{1}{2}, m=-\frac{1}{2}\rangle$$
 (5.30)

and on the other hand:

$$(\hat{L}_{-} + \hat{\sigma}_{-}) \left(\sqrt{\frac{2}{3}} | m_{l} = 1, m_{s} = -\frac{1}{2} \rangle - \sqrt{\frac{1}{3}} | m_{l} = 0, m_{s} = \frac{1}{2} \rangle \right)$$

$$= \sqrt{\frac{2}{3}} \hat{L}_{-} | m_{l} = 1, m_{s} = -\frac{1}{2} \rangle - \sqrt{\frac{1}{3}} (\hat{L}_{-} + \hat{\sigma}_{-}) | m_{l} = 0, m_{s} = \frac{1}{2} \rangle$$

$$= \sqrt{\frac{4}{3}} | m_{l} = 0, m_{s} = -\frac{1}{2} \rangle - \sqrt{\frac{2}{3}} | m_{l} = -1, m_{s} = \frac{1}{2} \rangle - \sqrt{\frac{1}{3}} | m_{l} = 0, m_{s} = -\frac{1}{2} \rangle$$

$$= \sqrt{\frac{1}{3}} | m_{l} = 0, m_{s} = -\frac{1}{2} \rangle - \sqrt{\frac{2}{3}} | m_{l} = -1, m_{s} = \frac{1}{2} \rangle$$

$$(5.31)$$

Thus, we have:

$$|j = \frac{1}{2}, m = -\frac{1}{2}\rangle = \sqrt{\frac{1}{3}}|m_l = 0, m_s = -\frac{1}{2}\rangle - \sqrt{\frac{2}{3}}|m_l = -1, m_s = \frac{1}{2}\rangle$$
 (5.32)

For the s-orbitals the extremal state, defined by $\hat{J}_{-}|j_{max}=\frac{1}{2},m_{max}=\frac{1}{2}\rangle=0$, we once more find the unique relation

$$|j = \frac{1}{2}, m = \frac{1}{2}\rangle = |m_l = \frac{1}{2}, m_s = \frac{1}{2}\rangle$$
 (5.33)

Applying \hat{J}_{-} , we have

$$\hat{J}_{-}|j=\frac{1}{2}, m=\frac{1}{2}\rangle = (\hat{L}_{-}+\hat{\sigma}_{-})|j=\frac{1}{2}, m=-\frac{1}{2}\rangle$$
 (5.34)

$$|j = \frac{1}{2}, m = -\frac{1}{2}\rangle = |m_l = \frac{1}{2}, m_s = -\frac{1}{2}\rangle$$
 (5.35)

The coefficients of the corresponding eigenstates can be organized into column vectors and combined into a matrix. This matrix represents the (sub-)transformation matrix, t_{nlm}^{J} , as described in equation (2.51), which is used for the basis change specified in equation (2.53).

As in previous calculations we must expand the matrix to account for the second atom in the unit cell

$$T_{nlm}^{J} = \begin{bmatrix} t_{nlm}^{J} & 0\\ 0 & t_{nlm}^{J} \end{bmatrix}$$
 (5.37)



5.4 Matrix Elements of the Bulk Hamiltonian

The total Hamiltonian H is divided into two sub-matrices, H_{AA} and H_{AB} , whose explicit elements are shown in Table 5.1. These sub-matrices are functions of g_i , which contain all the terms of the form $\exp(i\mathbf{k}\cdot\mathbf{R}_n)$, depending on the set of neighbors considered.

The g_i terms are grouped based on the type of neighbor interactions as follows:

- $g_0 g_{12}$: first-neighbor interactions,
- $g_{13} g_{25}$: second-neighbor interactions,
- $g_{26} g_{31}$: third-neighbor interactions.

The explicit expressions for $g_0 - g_{12}$ are given by:

$$g_0 = e^{i\mathbf{k}\cdot(\mathbf{a}_1 - \mathbf{d})} + e^{i\mathbf{k}\cdot(\mathbf{a}_2 - \mathbf{d})} + e^{i\mathbf{k}\cdot(\mathbf{a}_3 - \mathbf{d})}$$

$$g_1 = \left[-e^{-i\mathbf{k}\cdot(\mathbf{a}_1 - \mathbf{d})} + e^{i\mathbf{k}\cdot(\mathbf{a}_2 - \mathbf{d})} \right] \cos \alpha$$

$$g_2 = \left[e^{i\mathbf{k}\cdot(\mathbf{a}_1 - \mathbf{d})} + e^{i\mathbf{k}\cdot(\mathbf{a}_2 - \mathbf{d})} - 2e^{i\mathbf{k}\cdot(\mathbf{a}_3 - \mathbf{d})} \right] \cos \beta$$

$$g_3 = \left[e^{i\mathbf{k}\cdot(\mathbf{a}_1 - \mathbf{d})} + e^{i\mathbf{k}\cdot(\mathbf{a}_2 - \mathbf{d})} + e^{i\mathbf{k}\cdot(\mathbf{a}_3 - \mathbf{d})} \right] \cos \gamma$$

$$g_4 = \left[e^{i\mathbf{k}\cdot(\mathbf{a}_1 - \mathbf{d})} + e^{i\mathbf{k}\cdot(\mathbf{a}_2 - \mathbf{d})} \right] \cos^2 \alpha$$

$$g_5 = g_0 - g_4$$

$$g_6 = \left[-e^{-i\mathbf{k}\cdot(\mathbf{a}_1 - \mathbf{d})} + e^{i\mathbf{k}\cdot(\mathbf{a}_2 - \mathbf{d})} \right] \cos \alpha \cos \gamma$$

$$g_7 = \left[e^{i\mathbf{k}\cdot(\mathbf{a}_1 - \mathbf{d})} + e^{i\mathbf{k}\cdot(\mathbf{a}_2 - \mathbf{d})} + 4e^{i\mathbf{k}\cdot(\mathbf{a}_3 - \mathbf{d})} \right] \cos^2 \beta$$

$$g_8 = g_0 - g_7$$

$$g_9 = \left[e^{i\mathbf{k}\cdot(\mathbf{a}_1 - \mathbf{d})} + e^{i\mathbf{k}\cdot(\mathbf{a}_2 - \mathbf{d})} + e^{i\mathbf{k}\cdot(\mathbf{a}_3 - \mathbf{d})} \right] \cos^2 \gamma$$

$$g_{10} = \left[e^{i\mathbf{k}\cdot(\mathbf{a}_1 - \mathbf{d})} + e^{i\mathbf{k}\cdot(\mathbf{a}_2 - \mathbf{d})} + e^{i\mathbf{k}\cdot(\mathbf{a}_3 - \mathbf{d})} \right] \left(1 - \cos^2 \gamma \right)$$

$$g_{11} = \left[e^{i\mathbf{k}\cdot(\mathbf{a}_1 - \mathbf{d})} + e^{i\mathbf{k}\cdot(\mathbf{a}_2 - \mathbf{d})} - 2e^{i\mathbf{k}\cdot(\mathbf{a}_3 - \mathbf{d})} \right] \cos \beta \cos \gamma$$

$$g_{12} = \left[-e^{-i\mathbf{k}\cdot(\mathbf{a}_1 - \mathbf{d})} + e^{i\mathbf{k}\cdot(\mathbf{a}_2 - \mathbf{d})} \right] \cos \alpha \cos \beta$$



With $\mathbf{a}_1, \mathbf{a}_2, \mathbf{a}_3$, and \mathbf{d} defined in Section 2.1, the parameters $\cos \alpha, \cos \beta, \cos \gamma$ represent the direction cosines of the vector $\mathbf{a}_2 - \mathbf{d}$, from the central atom to one of the nearest-neighbor atoms.

The functions $g_{13} - g_{25}$ can be obtained by substituting:

- the set of first-neighbor vectors $\mathbf{a}_i \mathbf{d}$ for $i \in \{1, 2, 3\}$
- with the set of second-neighbor vectors $\mathbf{a}_i + \mathbf{a}_j \mathbf{d}$, for $i \neq j$, $i, j \in \{1, 2, 3\}$, as well as using the direction cosines of $\mathbf{a}_1 + \mathbf{a}_3 \mathbf{d}$.

For the set of third neighbors, $\mathbf{a}_i - \mathbf{a}_j$, with $i \neq j$, $i, j \in \{1, 2, 3\}$, the functions $g_{26} - g_{31}$ are defined as follows:

$$\begin{split} g_{26} &= e^{i\mathbf{k}\cdot(\mathbf{a}_{1}-\mathbf{a}_{2})} + e^{i\mathbf{k}\cdot(\mathbf{a}_{2}-\mathbf{a}_{1})} + e^{i\mathbf{k}\cdot(\mathbf{a}_{2}-\mathbf{a}_{3})} + e^{i\mathbf{k}\cdot(\mathbf{a}_{3}-\mathbf{a}_{2})} + e^{i\mathbf{k}\cdot(\mathbf{a}_{1}-\mathbf{a}_{3})} \\ g_{28} &= \frac{\sqrt{3}}{2} \left[e^{i\mathbf{k}\cdot(\mathbf{a}_{1}-\mathbf{a}_{2})} - e^{i\mathbf{k}\cdot(\mathbf{a}_{2}-\mathbf{a}_{3})} + e^{i\mathbf{k}\cdot(\mathbf{a}_{2}-\mathbf{a}_{3})} - e^{i\mathbf{k}\cdot(\mathbf{a}_{1}-\mathbf{a}_{3})} \right] \\ g_{29} &= e^{i\mathbf{k}\cdot(\mathbf{a}_{1}-\mathbf{a}_{2})} + e^{i\mathbf{k}\cdot(\mathbf{a}_{2}-\mathbf{a}_{1})} + \frac{1}{4} \left[e^{i\mathbf{k}\cdot(\mathbf{a}_{2}-\mathbf{a}_{3})} + e^{i\mathbf{k}\cdot(\mathbf{a}_{3}-\mathbf{a}_{2})} + e^{i\mathbf{k}\cdot(\mathbf{a}_{1}-\mathbf{a}_{3})} + e^{i\mathbf{k}\cdot(\mathbf{a}_{1}-\mathbf{a}_{3})} + e^{i\mathbf{k}\cdot(\mathbf{a}_{3}-\mathbf{a}_{1})} \right] \\ g_{30} &= \frac{3}{4} \left[e^{i\mathbf{k}\cdot(\mathbf{a}_{2}-\mathbf{a}_{3})} + e^{i\mathbf{k}\cdot(\mathbf{a}_{3}-\mathbf{a}_{2})} + e^{i\mathbf{k}\cdot(\mathbf{a}_{1}-\mathbf{a}_{3})} + e^{i\mathbf{k}\cdot(\mathbf{a}_{3}-\mathbf{a}_{1})} \right] \\ g_{31} &= \frac{\sqrt{3}}{4} \left[-e^{i\mathbf{k}\cdot(\mathbf{a}_{2}-\mathbf{a}_{3})} - e^{i\mathbf{k}\cdot(\mathbf{a}_{3}-\mathbf{a}_{2})} + e^{i\mathbf{k}\cdot(\mathbf{a}_{1}-\mathbf{a}_{3})} + e^{i\mathbf{k}\cdot(\mathbf{a}_{3}-\mathbf{a}_{1})} \right] \end{split}$$

It should be noted that matrix elements with the same (different) parity between orbitals transform even (odd) under the exchange of indices [2]

$$E_{ii}(-\mathbf{R}_n) = (-1)^{|l-l'|} E_{ij}(\mathbf{R}_n).$$

Die app	The ap
3ibliothek	Your knowledge hub
2	E E

$ p_z^1 \downarrow \rangle$	0	0	$\lambda/3$	$-i\lambda/3$	0	0	0	$E_p + g_{26}V_{pp\pi}''$
$ p_y^1\downarrow\rangle$	0	$g_{28}V_{sp\sigma}''$	0	0	$i\lambda/3$	$i\lambda/3 + g_{31}(V''_{pp\sigma} - V''_{pp\pi})$	$E_p + g_{29}V_{pp\pi}'' + g_{30}V_{pp\sigma}''$	0
$ p_x^1 \downarrow \rangle$	0	$g_{27}V_{sp\sigma}''$	0	0	$-\lambda/3$	$E_p + g_{29}V_{pp\sigma}'' + g_{30}V_{pp\pi}''$	$-i\lambda/3 + g_{31}(V_{pp\sigma}'' - V_{pp\pi}'')$ $E_p + g_{29}V_{pp\pi}'' + g_{30}V_{pp\sigma}''$	0
$ p_z^1 \uparrow\rangle$	0	0	0	0	$E_p + g_{26}V_{pp\pi}''$	$-\lambda/3$	$-i\lambda/3$	0
$ p_y^1 \uparrow\rangle$	$g_{28}V_{sp\sigma}^{\prime\prime}$	0	$-i\lambda/3 + g_{31}(V_{pp\sigma}''' - V_{pp\pi}'')$	$E_p + g_{29}V''_{pp\pi} + g_{30}V''_{pp\sigma}$	0	0	0	$i\lambda/3$
$ p_x^1 \uparrow\rangle$	$g_{27}V_{sp\sigma}^{\prime\prime}$	0	$E_p + g_{29}V'''_{pp\sigma} + g_{30}V'''_{pp\pi}$	$i\lambda/3 + g_{31}(V''_{pp\sigma} - V''_{pp\pi})$	0	0	0	$\lambda/3$
$ s^1\downarrow\rangle$	0	$E_s + g_{26}V_{ss\sigma}''$	0	0	0	$-g_{27}V_{sp\sigma}'''$	$-g_{28}V_{sp\sigma}'''$	0
$ s^1\uparrow\rangle$	$E_s + g_{26}V_{ss\sigma}^{\prime\prime\prime}$	0	$-g_{27}V_{sp\sigma}'''$	$-g_{28}V_{sp\sigma}'''$	0	0	0	0
H_{AA}	$ s^1 \uparrow\rangle$	$ s^1\downarrow\rangle$	$ p_x^1\uparrow\rangle$	$ p_y^1 \uparrow\rangle$	$ p_z^1\uparrow\rangle$	$ p_x^1\downarrow\rangle$	$ p_y^1\downarrow\rangle$	$ p_z^1\downarrow\rangle$

Table 5.1: The matrix elements of H_{AA} (top) and H_{AB} (bottom) from Ref. [21]. The primes on the Slater-Koster parameters denote the contribution from the corresponding (' for 2^{nd} and " for 3^{rd}) neighbors.

Bibliography

- Irene Aguilera et al. "Z2 topology of bismuth". In: Physical Review Materials [1]5.9 (Sept. 2021). ISSN: 24759953. DOI: 10.1103/PhysRevMaterials.5. L091201.
- Christian R. Ast and Isabella Gierz. "Sp -band tight-binding model for the Bychkov-Rashba effect in a two-dimensional electron system including nearest-neighbor contributions from an electric field". In: Physical Review B 86.8 (Aug. 2012), p. 085105. ISSN: 1098-0121. DOI: 10.1103/PhysRevB.86. 085105.
- Christian R. Ast and Hartmut Höchst. "Electronic structure of a bismuth bilayer". In: *Physical Review B* 67.11 (Mar. 2003), p. 113102. ISSN: 0163-1829. DOI: 10.1103/PhysRevB.67.113102.
- [4]Christian R. Ast and Hartmut Höchst. "Fermi surface of bi(111) measured by photoemission spectroscopy". In: *Physical Review Letters* 87.17 (Oct. 2001). ISSN: 10797114. DOI: 10.1103/PhysRevLett.87.177602.
- Yu. A. Bychkov and E. I. Rashba. "Properties of a 2D electron gas with |5|lifted spectral degeneracy". In: Pis'ma v ZHETF 39.2 (1984), p. 66. URL: http://jetpletters.ru/ps/0/article_19121.shtml.
- Supriyo Datta and Biswajit Das. "Electronic analog of the electro-optic modulator". In: Applied Physics Letters 56.7 (1990), pp. 665–667. ISSN: 00036951. DOI: 10.1063/1.102730.
- Niels Ehlen. "Spectroscopic Characterization of 1H-MoS 2 and 1H-TaS 2". PhD thesis. Köln: Physikalisches Institut Universität zu Köln, Dec. 2019.

i

- J.A Gaunt. "IV. The triplets of helium". In: Philosophical Transactions of the Royal Society of London. Series A, Containing Papers of a Mathematical or Physical Character 228.659-669 (Jan. 1929), pp. 151–196. ISSN: 0264-3952. DOI: 10.1098/rsta.1929.0004. URL: https://doi.org/10.1098/rsta. 1929.0004.
- Arfken George B., Weber Hans J., and Harris Frank E. Mathematical methods for physicists. 7th ed. Academic Press, 2013, pp. 756–760.
- Mark Oliver Goerbig. Introduction to Quantum Mesoscopic Transport and Topological Matter. 2024. URL: https://cel.hal.science/hal-04248649v2.
- David J. Griffiths. *Introduction to quantum mechanics*. 3rd ed. Cambridge: |11|Cambridge University Press, 1995.
- Yoyo Hinuma et al. "Band structure diagram paths based on crystallogra-|12|phy". In: (Feb. 2016). DOI: 10.1016/j.commatsci.2016.10.015.
- T. Hirahara et al. "Quantum well states in ultrathin Bi films: Angle-resolved photoemission spectroscopy and first-principles calculations study". In: Physical Review B - Condensed Matter and Materials Physics 75.3 (2007). ISSN: 10980121. DOI: 10.1103/PhysRevB.75.035422.
- T. Hirahara et al. "Role of spin-orbit coupling and hybridization effects in [14]the electronic structure of ultrathin Bi films". In: Physical Review Letters 97.14 (2006). ISSN: 00319007. DOI: 10.1103/PhysRevLett.97.146803.
- Ph. Hofmann. "The surfaces of bismuth: Structural and electronic proper-[15]ties". In: Progress in Surface Science 81.5 (Jan. 2006), pp. 191–245. ISSN: 00796816. DOI: 10.1016/j.progsurf.2006.03.001.
- Lee-Chi Hong, Chieh Chou, and Hao-Hsiung Lin. "Simulation on the electric [16] field effect of Bi thin film". In: Solid State Electronics Letters 2 (Dec. 2020), pp. 28-34. ISSN: 25892088. DOI: 10.1016/j.ssel.2020.04.001.
- R. Jackie and C. Rebbi. Solitons with fermion number $1/2^*$. Tech. rep. [17]Cambridge: Massachusetts Institute of Technology, Dec. 1975. DOI: https: //doi.org/10.1103/PhysRevD.13.3398.

- Markus König et al. "Quantum Spin Hall Insulator State in HgTe Quantum 18 Wells". In: Science 318.5851 (Nov. 2007), pp. 766–770. ISSN: 0036-8075. DOI: 10.1126/science.1148047.
- [19]J. Krempaský et al. "Operando Imaging of All-Electric Spin Texture Manipulation in Ferroelectric and Multiferroic Rashba Semiconductors". In: Physical Review X 8.2 (June 2018). ISSN: 21603308. DOI: 10.1103/PhysRevX.8. 021067.
- David R Lide et al. CRC Handbook of Chemistry and Physics Editor-in-[20]Chief. Tech. rep. 2008.
- Yi Liu and Roland E. Allen. "Electronic structure of the semimetals Bi and |21|Sb". In: Physical Review B 52 (1995). DOI: https://doi.org/10.1103/ PhysRevB.52.1566.
- X. Lu and M. O. Goerbig. "Dirac quantum well engineering on the surface of [22]a topological insulator". In: *Physical Review B* 102.15 (Oct. 2020), p. 155311. ISSN: 2469-9950. DOI: 10.1103/PhysRevB.102.155311.
- [23]Sadamichi Maekawa, ed. Concepts in Spin Electronics. New York: Oxford University Press, 2006. ISBN: 9780198568216.
- [24]Yoshiyuki Ohtsubo et al. "Non-trivial Surface-band Dispersion on Bi(111)". In: (Mar. 2013). DOI: 10.1088/1367-2630/15/3/033041.
- L. Petersen and P. Hedegård. "A simple tight-binding model of spin-orbit [25]splitting of sp-derived surface states". In: Surface Science 459.1-2 (July 2000), pp. 49–56. ISSN: 00396028. DOI: 10.1016/S0039-6028(00)00441-6.
- Kazuo Saito et al. "Tight-binding theory of surface spin states on bismuth [26] thin films". In: *Physical Review B* 93.4 (Jan. 2016), p. 041301. ISSN: 2469-9950. DOI: 10.1103/PhysRevB.93.041301.
- Wahyu Setyawan and Stefano Curtarolo. "High-throughput electronic band |27|structure calculations: Challenges and tools". In: Computational Materials Science 49.2 (Aug. 2010), pp. 299-312. ISSN: 09270256. DOI: 10.1016/j. commatsci.2010.05.010.

- [28] Shun-Qing Shen. *Topological Insulators*. Berlin: Springer-Verlag, 2012, pp. 15–17. ISBN: 978-3-642-32857-2. DOI: 10.1007/978-3-642-32858-9.
- [29] J. C. Slater. "Atomic Shielding Constants". In: *Physical Review* 36.1 (July 1930), pp. 57–64. ISSN: 0031-899X. DOI: 10.1103/PhysRev.36.57.
- [30] J. C. Slater and G. F. Koster. "Simplified LCAO Method for the Periodic Potential Problem". In: *Physical Review* 94.6 (June 1954), pp. 1498–1524. ISSN: 0031-899X. DOI: 10.1103/PhysRev.94.1498.
- [31] S.M. Sze and Kwok K. Ng. Physics of Semiconductor Devices. Wiley, Oct. 2006. ISBN: 9780471143239. DOI: 10.1002/0470068329.
- [32] Akari Takayama et al. "Tunable Spin Polarization in Bismuth Ultrathin Film on Si(111)". In: *Nano Letters* 12.4 (Apr. 2012), pp. 1776–1779. ISSN: 1530-6984. DOI: 10.1021/nl2035018.
- [33] Atsushi Togo, Kohei Shinohara, and Isao Tanaka. "Spglib: a software library for crystal symmetry search". In: (Aug. 2018). URL: http://arxiv.org/abs/1808.01590.
- [34] User: Alchemist-hp. *Bismuth*. Dec. 2010. URL: https://en.wikipedia.org/wiki/Bismuth#/media/File:Wismut_Kristall_und_1cm3_Wuerfel.jpg.
- [35] M. P. Vecchil and M. S. Dresselhaus. Temperature dependence of the band parameters of bismuth. Tech. rep. 1974. DOI: https://doi.org/10.1103/ PhysRevB.10.771.
- [36] Fan Zhang, C. L. Kane, and E. J. Mele. "Surface states of topological insulators". In: Physical Review B Condensed Matter and Materials Physics 86.8 (Aug. 2012). ISSN: 10980121. DOI: 10.1103/PhysRevB.86.081303.
- [37] Haijun Zhang and Shou Cheng Zhang. "Topological insulators from the perspective of first-principles calculations". In: *Physica Status Solidi Rapid Research Letters* 7.1-2 (Feb. 2013), pp. 72–81. ISSN: 18626254. DOI: 10.1002/pssr.201206414.

List of Figures

1.1	Picture of elemental Bismuth	3
2.1	Crystal structure of Bi	7
2.2	Bulk Brillouin zone of Bi	9
2.3	Thin Film Brillouin Zone of Bi	10
2.4	Slater-Koster Approximation	16
2.5	Illustration of Kramers Theorem	18
2.6	Spin Projection before and after applying an external Magnetic Field	21
2.7	Precession of \vec{L} and \vec{S} around \vec{J}	22
2.8	Interactions in Bulk Bi	34
2.9	Interactions in bilayered Bi	36
2.10	Illustration of continuous Deformation	42
2.11	Characterisation of a Topological Defect	43
2.12	Band Inversion at the L -point	47
2.13	Berry Flux of a massive Dirac Fermion	50
2.14	Illustration of a Dirac Quantum Well	53
2.15	Volkov-Pankratov States	56
2.16	Helical States in Time-Reversal Systems	58
2.17	Topological Classification of Semimetals	60
3.1	Band Structure of Bulk Bimuth	67
3.2	Group Velocity of Bulk Bismuth	69
3.3	Band Structure of thin Bi(111)	70
3.4	Computed Fermi Surface of thin $Bi(111)$	71
3.5	Layer Dependence of Spin Polarized Surface States	72
3.6	Gaped Dirac Fermion	74

3.7	Bismuth Thin-Film Band Structure in the case of the asymmetric	
	Bychkov-Rashba Effect	76
3.8	Realization of a massless Dirac fermion through the asymmetric	
	Bychkov-Rashba Effect	77
3.9	Realization of a massless Dirac fermion at the Fermi level	77
3.10	Realization of a massless Dirac fermion at the Fermi level at Γ	78
1 1		00
4.1	Schematic Layout of gated Sample used for operando SARPES	80